

Stephen F. Austin State University

**SFA ScholarWorks**

---

Electronic Theses and Dissertations

---

5-8-2020

## **Delineating Subsurface Karst Potential Using Electrical Resistivity in the Shell Mountain Province, Fort Hood Military Installation, Texas**

Annie Robison

*Stephen F Austin State University*, [anniepaige1317@gmail.com](mailto:anniepaige1317@gmail.com)

Follow this and additional works at: <https://scholarworks.sfasu.edu/etds>



Part of the [Geology Commons](#), and the [Geophysics and Seismology Commons](#)

[Tell us](#) how this article helped you.

---

### **Repository Citation**

Robison, Annie, "Delineating Subsurface Karst Potential Using Electrical Resistivity in the Shell Mountain Province, Fort Hood Military Installation, Texas" (2020). *Electronic Theses and Dissertations*. 309.

<https://scholarworks.sfasu.edu/etds/309>

This Thesis is brought to you for free and open access by SFA ScholarWorks. It has been accepted for inclusion in Electronic Theses and Dissertations by an authorized administrator of SFA ScholarWorks. For more information, please contact [cdsscholarworks@sfasu.edu](mailto:cdsscholarworks@sfasu.edu).

---

# Delineating Subsurface Karst Potential Using Electrical Resistivity in the Shell Mountain Province, Fort Hood Military Installation, Texas

## Creative Commons License



This work is licensed under a [Creative Commons Attribution-Noncommercial-No Derivative Works 4.0 License](https://creativecommons.org/licenses/by-nc-nd/4.0/).



**Delineating Subsurface Karst Potential Using Electrical Resistivity in the Shell  
Mountain Province, Fort Hood Military Installation, Texas**

By

Annie Robison, Bachelor of Science

Presented to the Faculty of the Graduate School of

Stephen F. Austin State University

In Partial Fulfillment

Of the Requirements

For the Degree of

Master of Science

Stephen F. Austin State University

May 2020

**Delineating Subsurface Karst Potential Using Electrical Resistivity in the Shell  
Mountain Province, Fort Hood Military Installation, Texas**

By

Annie Robison, Bachelor of Science

APPROVED:

---

Dr. Melinda Faulkner, Thesis Director

---

Dr. Kevin Stafford, Committee Member

---

Dr. Wesley Brown, Committee Member

---

Dr. I-Kuai Hung, Committee Member

---

Pauline M. Sampson, PhD  
Dean of Research and Graduate Studies

## **ABSTRACT**

Fort Hood Military Installation is located within the Lampasas Cut Plain in Bell and Coryell counties, Texas, and is characterized by exposures of Lower Cretaceous Trinity and Fredericksburg Group carbonates. The Shell Mountain Province is an elevated plateau located in western Fort Hood utilized by the military for heavy mechanical (troop and wheeled) maneuver training and hosts significant surficial and subsurface karst. Ongoing karst inventories in western Fort Hood conducted by range managers have documented over 100 individual karst features. Recent studies utilizing LiDAR and remote sensing techniques delineated karst potential in this area and identified over 13,909 discrete depressions.

This study used electrical resistivity to characterize subsurface karst potential associated with two known caves in the Shell Mountain Province. Existing cave maps from the Texas Speleological Survey and the Division of Natural Resource Management at Fort Hood were used to select areas in which there may be inaccessible passages. The AGI SuperSting was implemented using the dipole-dipole array method to complete 2-D and 3-D surveys at each of the cave locations. Results showed significant inaccessible subsurface karst features; these data will be utilized by the Fort Hood Natural Resources

Management Branch range managers to create karst management plans in Fort Hood training areas to support military readiness and protect environmentally sensitive habitats.

## ACKNOWLEDGEMENTS

Charles Pekins of the Natural Resources Branch on Fort Hood is acknowledged for his support in providing LiDAR data, cave maps, housing and access to the training areas on Fort Hood. This project would have been impossible to complete without his role in the process and for that I am forever grateful. I would like to take this moment to also recognize my Advisor, Dr. Melinda Faulkner, for providing the endless support and encouragement needed to complete this project. I know that without your insight, care, and availability to travel to the field with me, I would have never finished. I would also like to thank my thesis committee, Dr. Kevin Stafford, Dr. Wesley Brown and Dr. I-Kuai Hung for their dedication and consultation on this project. Next I want to mention the entirety of the SFA Geology department and my friends Kaleb Henry, Andrew Brillion, Heather Dailey and my fiancé Adam Winkelmann for their willingness to travel and complete field work with me as well as my other friends who offered their help in any way possible. Lastly, I want to thank my wonderful parents, family, and Adam who never shied away from encouraging and allowing me to continue my education. There are not enough words to thank you all enough for everything you have done to aid in the completion of this project.



## TABLE OF CONTENTS

ABSTRACT.....	i
ACKNOWLEDGMENTS.....	iii
TABLE OF CONTENTS.....	iv
LIST OF FIGURES.....	vii
LIST OF TABLES.....	xi
LIST OF EQUATIONS.....	xii
PREFACE.....	xiii
DELINEATING SUBSURFACE KARST POTENTIAL USING ELECTRICAL RESISTIVITY IN THE SHELL MOUNTAIN PROVINCE, FORT HOOD MILITARY INSTALLATION, TEXAS.....	1
ABSTRACT.....	1
INTRODUCTION.....	2
LITERATURE REVIEW.....	6
Geologic Setting.....	6
Structural History.....	9
Stratigraphy.....	14

Hydrogeology.....	18
Karst Formation.....	20
Resistivity.....	22
METHODOLOGY.....	31
Light Detection and Ranging (LiDAR).....	31
LiDAR and Digital Elevation Model Processing.....	31
Resistivity.....	41
Command Files.....	43
Data Acquisition.....	45
Field Setup.....	46
Processing.....	51
INTERPRETATION.....	59
Brokeback Cave.....	61
Fern Cave.....	71
LIMITATIONS.....	81
CONCLUSIONS.....	83

FUTURE WORK .....	85
REFERENCES.....	86
APPENDIX A.....	91
VITA.....	102

## LIST OF FIGURES

<b>Figure 1:</b> Map of the location of Fort Hood within Texas.....	3
<b>Figure 2:</b> Map of the physiographic regions of Texas including Fort Hood.....	4
<b>Figure 3:</b> Map of Fort Hood training areas.....	8
<b>Figure 4:</b> Map of major structural features of Central Texas.....	10
<b>Figure 5:</b> Depositional model for the Fredericksburg Group.....	12
<b>Figure 6:</b> Deposition controlling features in the Cretaceous in Central Texas.....	13
<b>Figure 7:</b> Map of the zones of the Edwards Aquifer.....	18
<b>Figure 8:</b> Stratigraphic units within aquifers in Central Texas.....	19
<b>Figure 9:</b> Formation model for epigenetic and hypogenic karst.....	21
<b>Figure 10:</b> Model for current flow paths based on electrode placement.....	25
<b>Figure 11:</b> Schematic of current flow patterns in the subsurface.....	26
<b>Figure 12:</b> Common 2-D survey arrays .....	27
<b>Figure 13:</b> Pole-dipole array layout.....	28
<b>Figure 14:</b> Digital elevation model surrounding Brokeback and Fern Caves.....	33

<b>Figure 15:</b> Fill-difference raster from digital elevation model.....	34
<b>Figure 16:</b> Shapefile of depressions from fill-difference raster.....	36
<b>Figure 17:</b> Delineated sinks surrounding known cave features.....	37
<b>Figure 18:</b> Stream filter used in depression refinement.....	38
<b>Figure 19:</b> Major and minor road filters surrounding both caves.....	39
<b>Figure 20:</b> Landcover filter for the radius around both caves.....	40
<b>Figure 21:</b> Digital elevation model and filtered depressions surrounding both caves.....	42
<b>Figure 22:</b> 2-D command files for surveys.....	44
<b>Figure 23:</b> Schematic for the 2-D dipole-dipole array.....	45
<b>Figure 24:</b> Map showing the locations of survey lines surrounding Fern Cave.....	47
<b>Figure 25:</b> Map showing the locations of survey lines near Brokeback Cave.....	48
<b>Figure 26:</b> Schematic of survey setup in 2-D and 3-D.....	49
<b>Figure 27:</b> Images of survey lines in the field.....	49
<b>Figure 28:</b> Example of a terrain correction.....	52
<b>Figure 29:</b> Initial inversion settings for 2-D surveys.....	53
<b>Figure 30:</b> Inversion settings used for 2-D surveys.....	54

<b>Figure 31:</b> Examples of a data misfit histogram.....	55
<b>Figure 32:</b> Examples of a cross-plot after processing.....	56
<b>Figure 33:</b> Examples of static contours in a 3-D pseudosection.....	57
<b>Figure 34:</b> Examples of dynamic contours in a 3-D pseudosection.....	58
<b>Figure 35:</b> Examples of 3-D contours in a 3-D pseudosection.....	58
<b>Figure 36:</b> Density analysis for the 25 km <sup>2</sup> area containing both caves.....	60
<b>Figure 37:</b> Depression density analysis for Brokeback Cave.....	62
<b>Figure 38:</b> Cave map for Brokeback Cave.....	63
<b>Figure 39:</b> Cross-sections for Brokeback Cave survey lines.....	64
<b>Figure 40:</b> Images showing karst features seen in outcrop near Brokeback Cave.....	66
<b>Figure 41:</b> 2-D processed pseudosections for Brokeback Cave.....	67
<b>Figure 42:</b> 3-D analysis for Brokeback Cave line 1.....	69
<b>Figure 43:</b> 3-D analysis for Brokeback Cave line 2.....	70
<b>Figure 44:</b> Depression density analysis for Fern Cave.....	72
<b>Figure 45:</b> Cave map for Fern Cave.....	73
<b>Figure 46:</b> Cross-sections for Fern Cave survey lines.....	74

<b>Figure 47:</b> Images of karst features seen in outcrop near Fern Cave.....	75
<b>Figure 48:</b> 2-D processed pseudosections for Fern Cave.....	76
<b>Figure 49:</b> 3-D analysis for Fern Cave line 1.....	79
<b>Figure 50:</b> 3-D analysis for Fern Cave line 2.....	80
<b>Figure A1:</b> A general location for the study area within Fort Hood .....	92
<b>Figure A2:</b> Survey analysis for Brokeback Cave line 1 2-D. ....	93
<b>Figure A3:</b> Survey analysis for Brokeback Cave line 2 2-D.....	94
<b>Figure A4:</b> Survey analysis for Fern Cave line 1 2-D.....	95
<b>Figure A5:</b> Survey analysis for Fern Cave line 2 2-D. ....	96
<b>Figure A6:</b> Survey analysis for Fern Cave line 3 2-D.....	97
<b>Figure A7:</b> Survey analysis for Brokeback Cave line 1 3-D.....	98
<b>Figure A8:</b> Survey analysis for Brokeback Cave line 2 3-D.....	99
<b>Figure A9:</b> Survey analysis for Fern Cave line 1 3-D.....	100
<b>Figure A10:</b> Survey analysis for Fern Cave line 2 3-D.....	101

## LIST OF TABLES

<b>Table 1:</b> Filter classification and buffer distances applied to remove depressions not associated with karst formation .....	40
--	----



## LIST OF EQUATIONS

**Equation 1:** Resistance ( $R$ ) (ohm·m) =  $\frac{\text{Potential Difference (Volts)}}{\text{Applied Current (amps)}} = \frac{V}{I}$  .....23

**Equation 2:** Resistance ( $R$ )=resistivity ( $\rho$ ) $\times \frac{\text{length } (l)}{\text{cross-sectional area } (A)} = \rho \times \frac{l}{A}$ .....23

**Equation 3:** Resistivity ( $\rho$ )=resistance ( $R$ ) $\times \frac{\text{cross-sectional area } (A)}{\text{length } (l)} = R \times \frac{A}{l}$ .....23

**Equation 4:**  $k = \pi n (n+1) (n+2) a$ .....43

## **PREFACE**

Karst features have been the focus of extensive geological, biological, and environmental research on the Fort Hood Military Installation. The majority of studies conducted on the base have been focused on surficial karst and caves opened to the surface. A karst database was created by the Natural Resources Management Branch at Fort Hood to document these known features, and reporting was completed manually by personnel conducting traverses and remote sensing techniques. Recent research in western Fort Hood has documented a high density of karst features in the Shell Mountain Province, and specifically showed that there were smaller karst features in the general area near known caves. These surficial karst features may indicate the location of subsurface phenomena that link to known cave passages or previously undocumented karst. Electrical resistivity is a common tool used in exploration of subsurface karst formations and allows for further analyses of known cave passages.

This research was conducted in association with the Natural Resources Management Branch of the Fort Hood Military Installation. This study will be used to expand the current understanding of subsurface karst in the installation training areas in order to maximize military personnel and equipment safety and preserve environmentally sensitive natural habitats. Using non-invasive electrical resistivity in areas surrounding known caves allows researchers and range managers the ability to study and document

the morphology of subsurface features and their potential connection to known karst.

This manuscript has been formatted with guidelines established by the Graduate School of Stephen F. Austin State University. Appendix A contains additional data associated with geophysical surveys.

## **ABSTRACT**

Fort Hood Military Installation is located within the Lampasas Cut Plain in Bell and Coryell counties, Texas, and is characterized by exposures of Lower Cretaceous Trinity and Fredericksburg Group carbonates. The Shell Mountain Province is an elevated plateau located in western Fort Hood utilized by the military for heavy mechanical (troop and wheeled) maneuver training and hosts significant surficial and subsurface karst. Ongoing karst inventories in western Fort Hood conducted by range managers have documented over 100 individual karst features. Recent studies utilizing LiDAR and remote sensing techniques delineated karst potential in this area and identified over 13,909 discrete depressions.

This study used electrical resistivity to characterize subsurface karst potential associated with two known caves in the Shell Mountain Province. Existing cave maps from the Texas Speleological Survey and the Division of Natural Resource Management at Fort Hood were used to select areas in which there may be inaccessible passages. The AGI SuperSting was implemented using the dipole-dipole array method to complete 2-D and 3-D surveys at each of the cave locations. Results showed significant inaccessible subsurface karst features; these data will be utilized by the Fort Hood Natural Resources Management Branch range managers to create karst management plans in Fort Hood training areas to support military readiness and protect environmentally sensitive habitats.

## INTRODUCTION

The Shell Mountain Province is a karst plateau located within the western portion of Fort Hood Military Installation near the city of Killeen, Texas in Bell and Coryell counties. The installation is contained entirely within the Lampasas Cut Plain (Figures 1 and 2) and is one of the largest active military training bases in the United States (Hayden et al. 2001, Pugsley 2001). Western Fort Hood is characterized by outcrops of Lower Cretaceous Trinity and Fredericksburg Group carbonates. The topography consists of relatively flat plateaus capped by the resistant Edwards Formation, while lower elevations contain the less resistant Comanche Peak, Walnut, and Glen Rose carbonates (Figure 3). Karst development in western Fort Hood is extensive and has been documented by ongoing research by range managers and geoscientists (Faulkner and Bryant 2018, Reece 2018, Faulkner et al. 2013, Bryant 2012, Reddell et al. 2001, and Veni 1994)

Subsurface karst exploration using geophysical methods has recently become more common and though there are many effective methods, electrical resistivity is one of the most commonly used for near surface karst exploration techniques (Majzoub 2016, Park et al. 2013, Chalokakis et al. 2011, Zhou et al. 2002). This method can effectively delineate subsurface karst features in the near surface due to changes in the distribution of

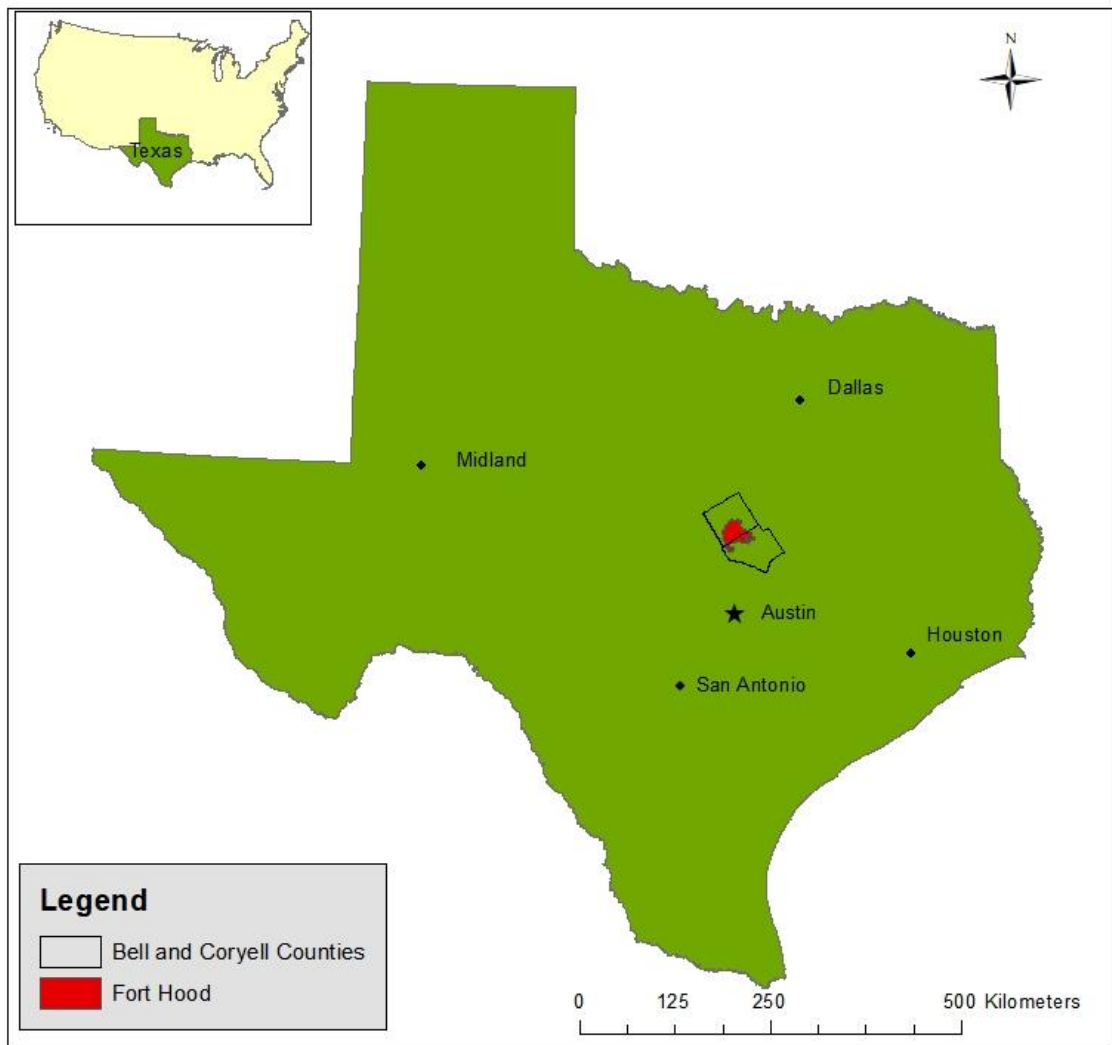


**Figure 1:** Map of the general location of Fort Hood within the State of Texas (modified from Texas Department of Transportation (TXDOT) 2019).

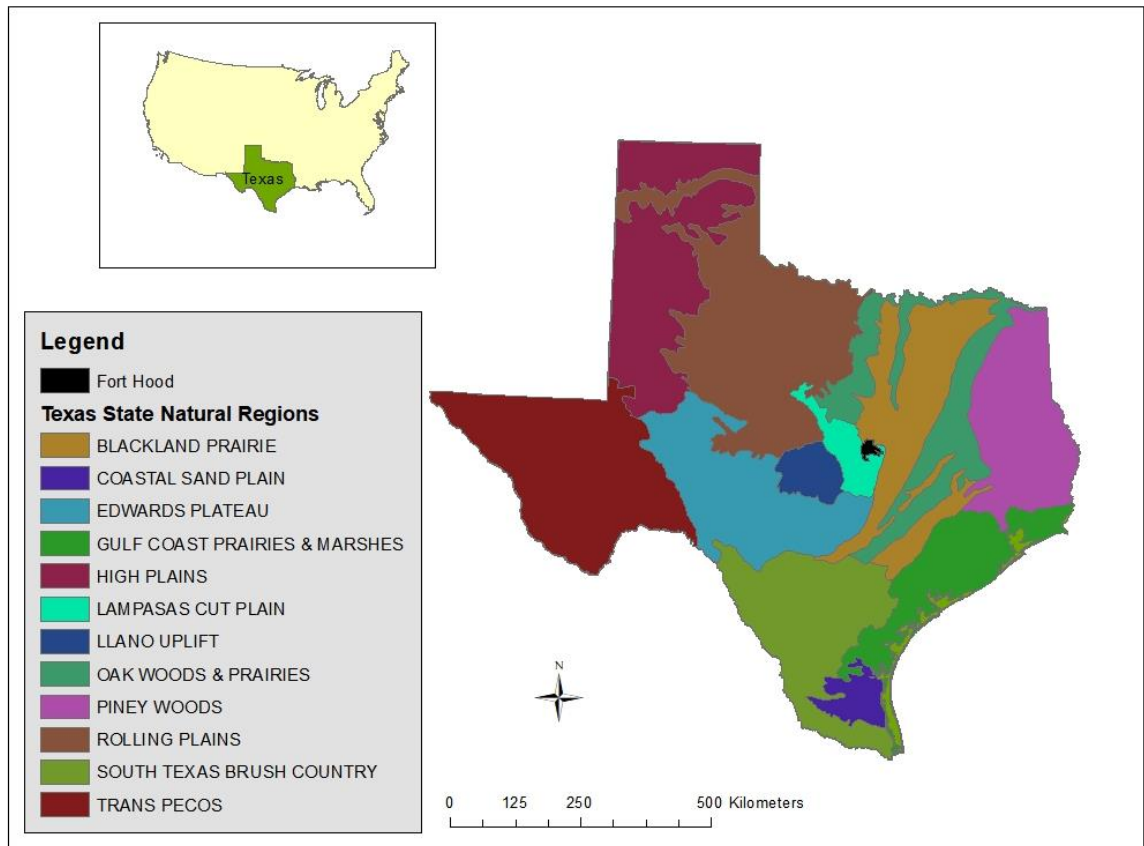


**Figure 2:** The physiographic regions of Texas including those surrounding Fort Hood, labeled in black (modified from Texas Parks and Wildlife 2020).

electrical resistivity of an injected current in a variety of settings. These surveys can be completed as single 2-dimensional slices or as a 3-dimensional volume of the subsurface.

This study focused on using electrical resistivity methods to characterize and delineate the extent of unmapped voids, collapse structures, and potential subsurface conduits associated with known cave features. Caves in the area were previously mapped by the Texas Speleological Survey and determined that there may be the possibility of continued cave passages associated with known karst features (Texas Speleological Survey 2014). Two caves were chosen within this area and were surveyed using a SuperSting R8 56 Electrode System. These surveys were used to determine the likelihood of potential collapse near known cave entrances, which would support enhanced safety protocols for military operations taking place in the area. Using known caves for this study provided the ability to determine the reliability of 2-D and 3-D resistivity within the region, assess the extent of known and newly discovered karst features, and the possible extent of additional karst features associated with known caves.



## **LITERATURE REVIEW**

### **Geologic Setting**

The majority of Fort Hood is dominated by exposures of Lower Cretaceous carbonates that were deposited in a shallow marine environment across the Comanche Shelf. The topography of the area is characterized by plateaued drainage divides capped by resistant limestones with steep slopes and scarps exposing the inter-fingering Edwards and Comanche Peak limestones. Exposures along these scarps reveal significant karst development near the Comanche Peak and Edwards boundaries, including shelter caves that develop on the edges of plateaus (Faulkner 2016). In general, western Fort Hood shows significantly less relief than the eastern portions with broad plateaus, gentle slopes and wide, open lowlands dominating the landscape.

Across the plateaus, karst development in the study area is usually observed in the Edwards, a white to gray limestone that hosts significant karst (Adkins and Arick 1930). Surficial karst features observed in the area include sinkholes, caves with collapse structures, and fractures and joints that have been solutionally widened (Faulkner 2016). Because Fort Hood training areas are utilized for a variety of military training exercises, it is important to understand the location of karst features at the surface and their subsurface extent.

The study area is mostly rural with paved and gravel roads used by military personnel for heavy artillery training, aerial maneuvers, and mobilization drills (Pugsley 2001). The average annual low temperature for the area is 12°C with summer highs commonly reaching 25°C and an average annual rainfall of 83.9 centimeters (United States Climate Data 2019).

### **Shell Mountain Province**

The Shell Mountain Province is located in the northwestern portion of the Fort Hood Military Installation (Figure 3). Shell Mountain an elevated plateau that hosts a variety of karst features as documented by Reece (2018) and Reddell et al. (2001). The two major karst features identified for this study were Fern Cave and Brokeback Cave. These caves are located within Edwards Limestone and have additional karst development proximal to their location. The Shell Mountain Province covers a total of 5,212 acres and is one of the highest elevations in western Fort Hood (Reece 2018).

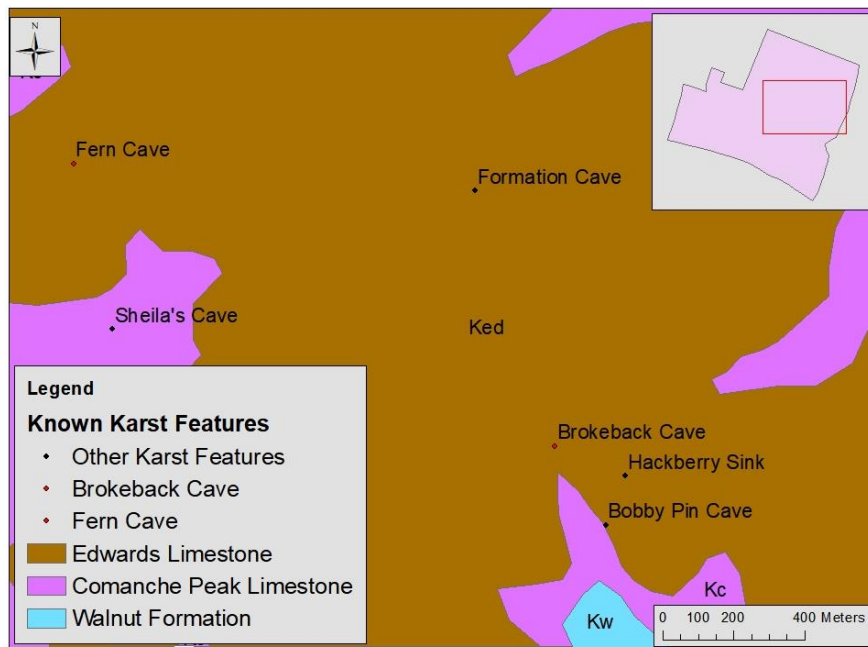
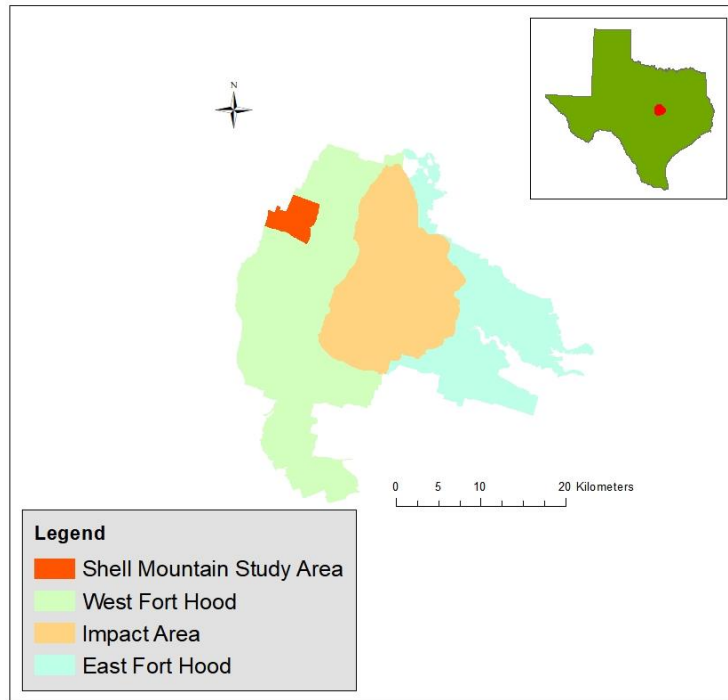


**Figure 3:** Layout of Fort Hood with the Shell Mountain Province highlighted in red (top) and geologic units seen in outcrop (bottom) (modified from Texas Water Science Center 2014).

## **Structural History**

The Edwards Plateau and Lampasas Cut Plain are composed primarily of Lower Cretaceous rocks and sediments overlying Paleozoic and Proterozoic bedrock (Anaya 2004). In the early Proterozoic, deep burial and compressive forces associated with the Grenville Orogeny metamorphosed existing underlying rocks and initiated emplacement of igneous bodies that would form the basement complex for the Llano Uplift region. Extensive erosion began during this time due to subaerial exposure and removed upwards of 200 meters of rock as evidenced in outcrops in the Llano Uplift (Walker 1979). During the Ordovician, extensive shallow seas caused by a transgressive series led to the deposition of the Ellenburger Group, but uplift and erosion of the Edwards Plateau in the middle Ordovician led to the removal of some of these sediments and restricted further deposition (Faulkner and Bryant 2018). Subsidence occurred again in the late Ordovician, and sedimentation continued in marine settings (Walker 1979).

During the Pennsylvanian and Permian, the Ouachita Orogeny occurred as a result of the tectonic plate collisions between the North American, European, and African/South American plates during the formation of Pangea (Anaya and Jones 2009). The folding and uplift brought about by this tectonic event created the Ouachita Mountains that extended from present day Northern Mexico to Oklahoma and Arkansas. Uplift continued through the end of the Paleozoic and led to the development of the

Concho Arch and the Concho Shelf in present day Central Texas (Faulkner and Bryant 2018; Figure 4). Extended periods of erosion removed many of the Early Paleozoic rocks and sediments. As sea level fluctuated, Pennsylvanian-aged sediments of varying composition were deposited over the Proterozoic basement on the Concho Shelf (Faulkner 2016). During this time, reefs began to form along the eastern margin of the Concho Shelf (Walker 1979.)

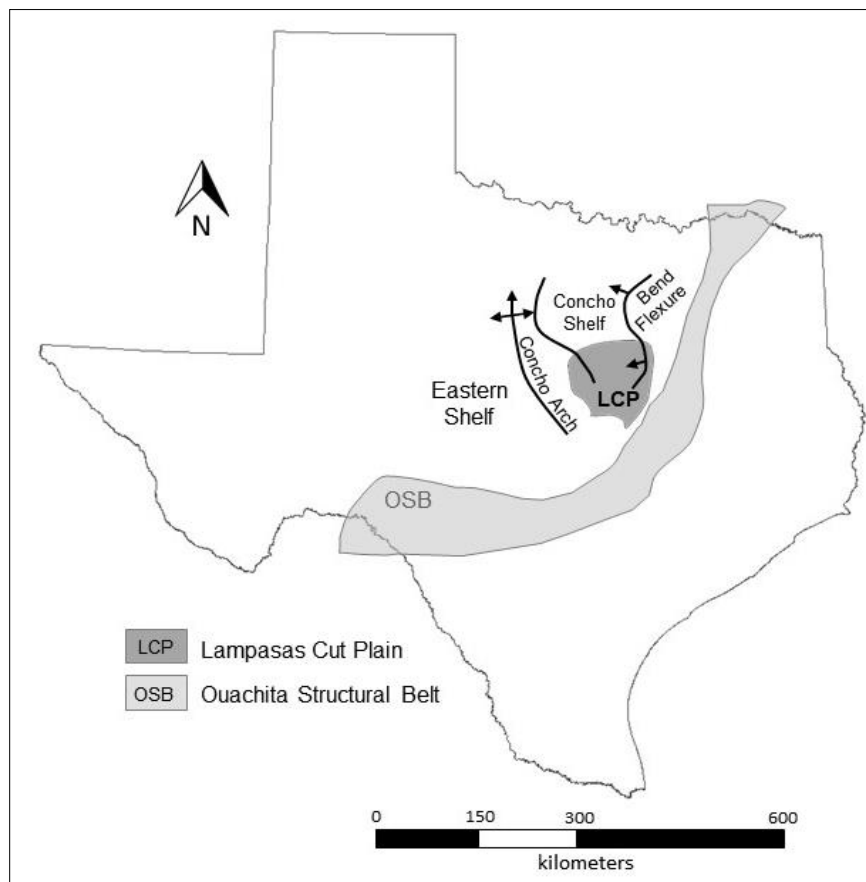


**Figure 4:** Major Paleozoic structures in Texas, including the Ouachita Structural Belt (from Faulkner and Bryant 2018).

Tectonic movement associated with the continuing formation of Pangea in the Permian caused the landmass to tilt westward toward the present-day Midland Basin. To the north and west of the Ouachita orogenic belt, evaporite and carbonate sediments were deposited in the deepening basins of West Texas. Reef structures provided shelter from the open ocean, allowing cyclic sedimentation of gypsum and halite to accumulate in the modern-day Delaware and Permian basins. This area was also the location for the deposition of shale (red beds) within the Permian Basin (Anaya and Jones 2009). At the end of the Permian, Pangea was fully formed, and the Ouachita Tectonic Cycle ended (Walker 1979).

In the Late Triassic, Pangea began to break apart causing major rifting along the southeastern and eastern margins of the North American continent, opening the ancestral Atlantic Ocean. As Laurentia continued to separate from southern landmasses, the Gulf of Mexico began to form and drainage from the interior of Laurentia began to shift from the northwest to the southeast (Anaya and Jones 2009). During the Jurassic, the entirety of the study area was exposed above sea level leading to extensive erosion of the Ouachita Fold Belt, which transported massive amounts of sediments into the newly formed Gulf of Mexico (Faulkner and Bryant 2018). Regional tilting during this time period provided the structural foundation for the formation of new continental shelf deposits of the Lower Cretaceous Trinity and Fredericksburg groups (Anaya and Jones 2009).

In the Cretaceous, transgressive, and regressive sequences led to the deposition of progradational carbonate facies over previously eroded surfaces (Figure 5). The Llano Uplift, formed in the Proterozoic, became the most predominant element in this shelf environment and provided the substrate for the deposition of thick sequences of sedimentary rock (Anaya and Jones 2009). In the Lampasas Cut Plain, these rocks were deposited across a broad plain known as the Comanche Shelf and include the Trinity, Fredericksburg, and Washita groups (Faulkner and Bryant 2018; Figure 6). In the late Cretaceous and early Paleogene, the Central Texas region was influenced by the Laramide Orogeny resulting in regional uplift and further exposure of the Edwards Plateau and Lampasas Cut Plain (Faulkner and Bryant 2018).

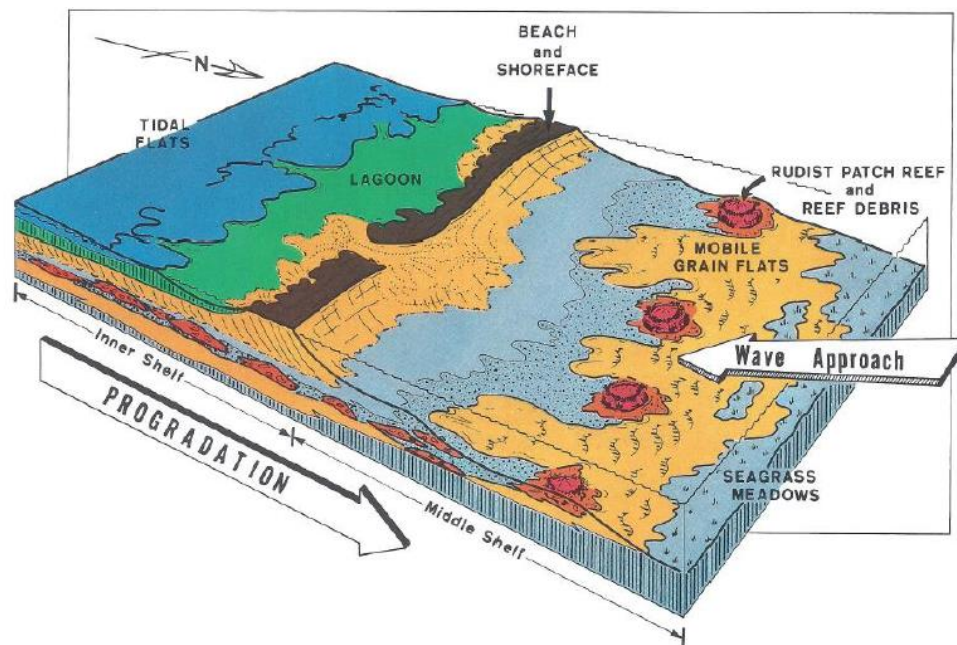


**Figure 5:** General depositional model for the Fredericksburg Group within the middle Comanche Shelf during a progressive stage (from Kerr 1977).

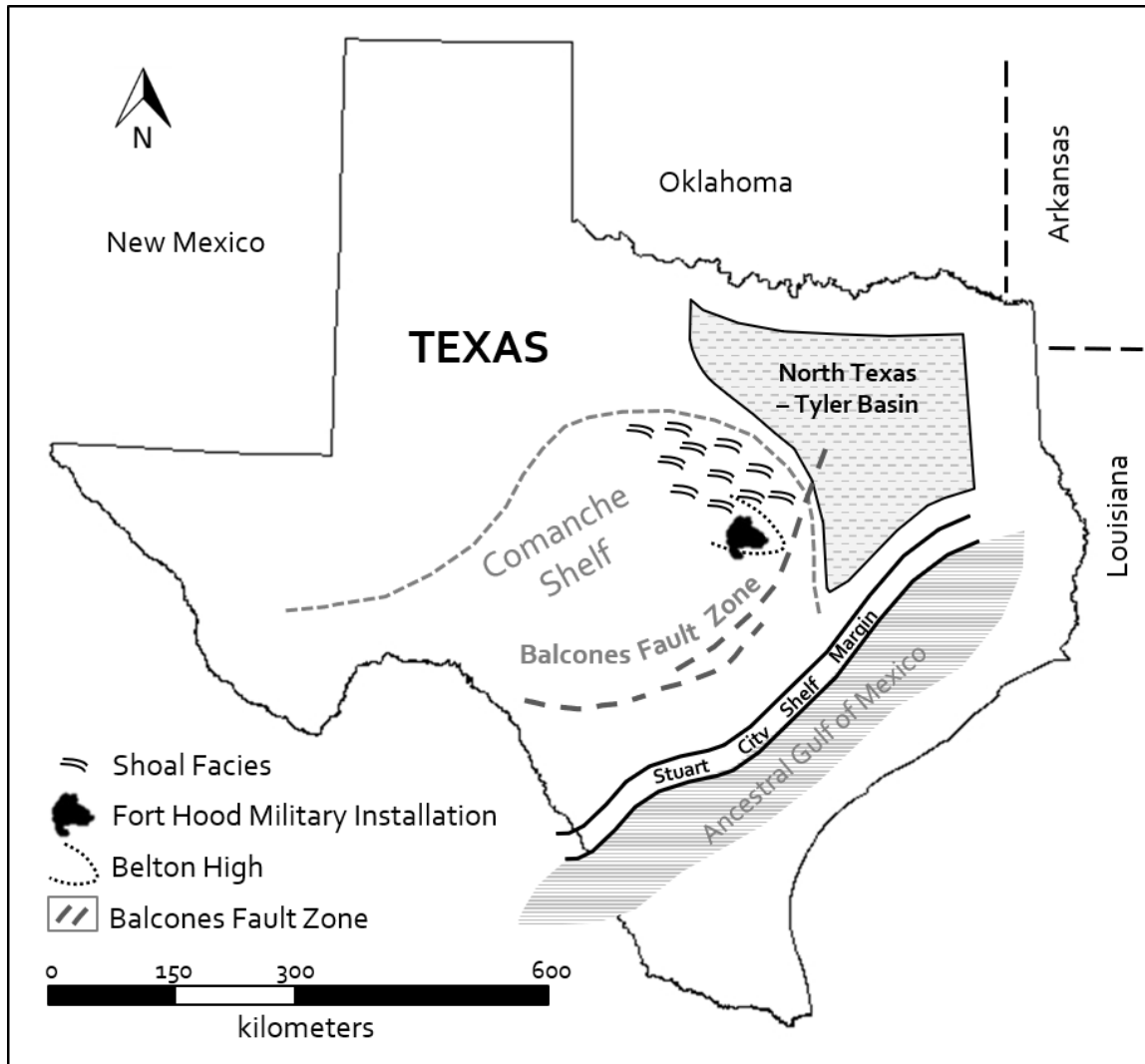


**Figure 6:** Structural features that controlled deposition during the Lower Cretaceous (from Faulkner 2016).

This uplift and exposure led to further erosion of rocks and sediments by rivers and streams (Faulkner and Bryant 2018). The Edwards Limestone was more resistant to this weathering and produced a large, relatively flat plateau that redirected the flow of the major river systems (Faulkner and Bryant 2018). The addition of displaced sediment into



the newly formed Gulf of Mexico along with continued uplift of the region led to the formation of tensional stresses along the buried Ouachita Fold Belt. The release of this stress led to the formation of the Balcones Fault Zone in the Miocene, and further distinguished the extent of the Edwards Plateau (Anaya and Jones 2009).

During the Quaternary, there was a significant change in the climate of Central Texas. Wind-blown loess sediments were deposited that would later develop into fertile soils. Melting glaciers provided excess moisture to enhance the flow volume of major rivers, leading to the erosion and incision of the Edwards Plateau and Lampasas Cut Plain, and the retreat of the Balcones Escarpment (Faulkner and Bryant 2018). Headward erosion of major stream systems occurred throughout the Quaternary, creating the rolling hills and entrenched valleys of the present-day Edwards Plateau and Lampasas Cut Plain (Anaya 2004).

### **Stratigraphy**

The Lampasas Cut Plain is characterized by exposures of Lower Cretaceous carbonates of the Trinity, Fredericksburg, and Washita groups (Scott and Kidson 1977). Most topographic highs are dominated by resistant Washita and Fredericksburg group carbonates, while the Trinity Group carbonates are found in topographic lows associated with stream incision (Nelson 1973). The bedding of these units is mostly horizontal or gently dipping to the southeast. Many of the exposed rock outcrops are irregularly eroded

and host karst features (Amsbury et al. 1984). In the Shell Mountain Province, Fredericksburg Group carbonates are the most common lithologies.

### **Trinity Group**

The Glen Rose Formation is composed of limestone, dolostone and thin interbeds of marls and calcareous shale divided into upper and lower members along a *Corbula* marker bed (Mancini and Scott 2006). The lower portion of the Glen Rose is characterized by cycles of intertidal to tidal mudstones to rudist and coral boundstones (Mancini and Scott 2006). The upper Glen Rose is a high stand carbonate platform that was deposited in a third order depositional sequence (Bryant 2012). The entirety of the Glen Rose has an average thickness of 244 meters with alternating resistant and erosion prone beds that have created characteristic stair-step topography (Collins 2005). Common fossils in the Glen Rose include bivalves, gastropods, echinoids, and foraminifera (Reece 2018).

The Paluxy Formation overlies the Glen Rose and is separated into upper and lower members as well. The lower member is marine to marginal marine fine-grained sandstone, siltstone and claystone. The upper member is classified by bioturbated interbedded quartz sandstone and limestone (Mancini and Scott 2006). The Paluxy Formation is relatively thin with an average thickness of three meters, outcrops infrequently in stream channels in western Fort Hood, and inter-fingers with the overlying Walnut Formation (Collins 2005, Bryant 2012).

## **Fredericksburg Group**

The Walnut Formation is the lowermost formation of the Fredericksburg Group and inter-fingers with the underlying Paluxy Formation in some areas (Bryant 2012). There is a total of six members of the Walnut Formation including the Bull Creek Limestone, Bee Cave Marl, Cedar Park Limestone, Whitestone Limestone, Keys Valley Marl and Upper Marl (Rose 1972). The Whitestone, Bull Creek, and Cedar Park are fossiliferous wackestones and peloidal, oolitic grainstones and packstones, and hardgrounds are common within these members. The Bee Cave, Keys Valley and Upper Marl are claystones, lime mudstones, and wackestones and represent higher order cycles (Mancini and Scott 2006). The most common member in the study area is the Keys Valley Marl and the entirety of this formation laterally grades into the overlying Comanche Peak Formation (Nelson 1973). Common fossils include bivalves, gastropods and echinoids (Amsbury et al. 1984).

The Comanche Peak Formation overlies the Walnut and is composed of nodular limestone with interbedded marl. This formation varies in thickness, but averages between 12 to 21 meters (Collins 2005). Fossils common in this formation are ammonites, bivalves, gastropods and echinoids (Bryant 2012). The chalky texture of the Comanche Peak allows contrast with the crystalline nature of the overlying Edwards Formation (Adkins and Arick 1930). The Comanche Peak is a member of the Edwards

Aquifer, but does not possess the transmissive properties of the overlying Edwards Formation (Klimchouk et al. 2012).

The Edwards Formation overlies the Comanche Peak and is distinguished by mostly white to cream/yellow to gray limestones and dolostones that may contain chert nodules and fossils (Adkins and Arick 1930). There are three component facies that comprise this group: 1) rudist bioherms, 2) platform grainstones, and 3) lagoonal facies (Fisher and Rodda 1969). The Edwards has a variable thickness and thins to the north from its maximum thickness of 90 meters near Austin, Texas (Adkins and Arick 1930). The Edwards Formation is heavily karsted and contains numerous sinks, caves and conduits (Jones 2003).

### **Washita Group**

The Georgetown Formation is comprised of cycles of shale and limestone and overlies the Edwards. The shales are calcareous in nature and the limestones are fossil rich with bivalves ranging in texture from wackestones to grainstones (Mancini and Scott 2006). This formation is included in the northern extent of the Edwards Aquifer and ranges in thickness from approximately 18-34 meters (Collins 2005). The Georgetown is known for its vuggy porosity, which along with the fossil content can be used to distinguish the Georgetown from underlying the Edwards (Bryant 2012). Though the Georgetown Formation is an important unit of the Lampasas Cut Plain, it has not been observed in western Fort Hood (Reece 2018).

## Hydrogeology

The study area lies north and west of the northern extent of the Edwards Aquifer, and may have intermittent connection with the aquifer. The Edwards Aquifer is one of the largest within the State of Texas and many of the major cities within the state are dependent upon this aquifer as their primary water source. The entirety of the Edwards Aquifer is divided into three segments: The San Antonio, Northern and Barton Spring segments (Jones 2003, Figure 7).

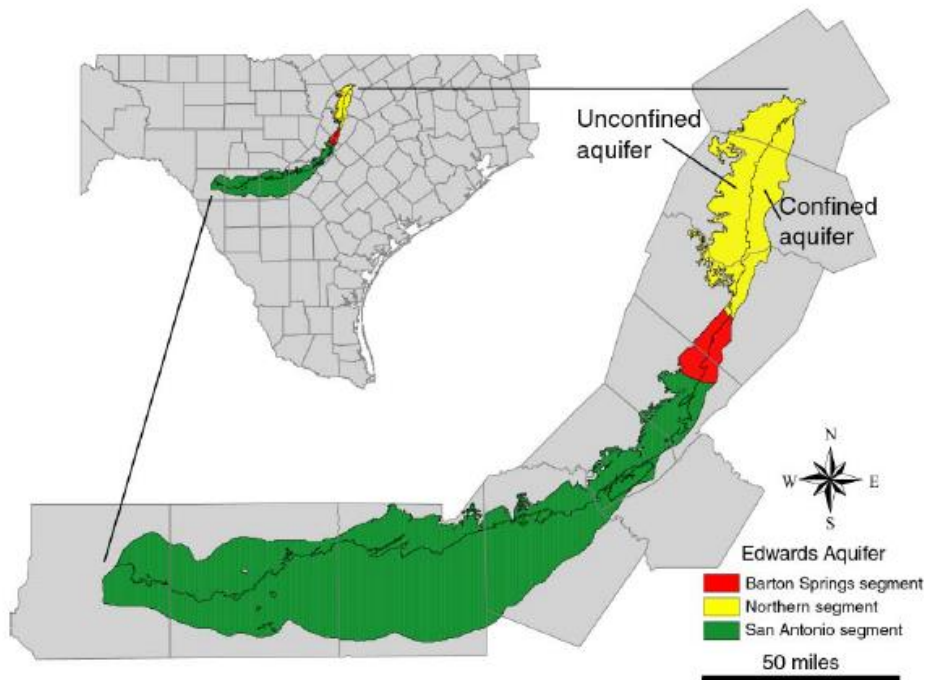


**Figure 7:** The location and zones of the Edwards Aquifer within the State of Texas (from Jones 2003).

In general, the northern segment of the Edwards Aquifer includes the Comanche Peak, Edwards, and the Georgetown formations (Figure 8). The aquifer is underlain by the Walnut Formation and capped by the Del Rio Clay in most areas (Jones, 2006). The Balcones Fault divides the aquifer into an eastern and western portion; the eastern portion is confined, with higher salinity and total dissolved solids (TDS), and longer residence times, while the western portion of the aquifer is unconfined (Jones 2003). To the west, aquifer recharge is transmitted to the subsurface through precipitation events via fractures, collapse and karst features, and the presence of joints (McCann 2012, Veni et al. 2005).

Series	Group	Stratigraphic Unit	Hydrologic Unit	Maximum Thickness (feet)	
Gulf	Navarro		Navarro and Taylor Group	850	
	Taylor				
	Austin		Austin Chalk	450	
Comanche	Eagle Ford			50	
	Washita	Buda Limestone		50	
		Del Rio Clay		60	
		Georgetown Formation		100	
	Fredericksburg	Edwards Limestone	Edwards aquifer	200	
		Comanche Peak Limestone		50	
		Walnut Formation		150	
		Paluxy Formation	Upper Trinity	10	
	Glen Rose	Upper Member		450	
		Lower Member	450		
	Trinity	Travis Peak	Hensell Sand Member	Middle Trinity	100
			Cow Cr. Limestone Member		100
		Hammett Shale Member	50		
		Sligo Member	Lower Trinity	150	
Hosston Member		850			

**Figure 8:** Major stratigraphic units and aquifers in Central Texas (from Jones 2003).

## **Karst Formation**

The majority of karst formation within the Lampasas Cut Plain is confined to the Edwards and Georgetown units and is controlled by lithology. There are a few exceptions in other units that show some bedding plane cave formation. These caves are predominately vertical in flow direction and initial development but can exhibit significant lateral component. Overall, most of the caves in the study area contain features associated with hypogenic and epigenic processes (Faulkner and Bryant 2018).

A recent karst potential survey conducted by Reece (2018) found extensive surficial karst development in western Fort Hood, including caves, shelter caves and sinks. Many of these caves are thought to be derived from hypogenic settings with epigenic overprinting, and form along joints associated with local hydraulic gradients which allowed meteoric waters to percolate through the Edwards Limestone (Landers 2016, Veni 1994, Figure 9). The movement of water along these joints also provides efficient conduits for water flow and dissolution of the surrounding limestone.

The three principle types of sinkholes within the area are dissolution, subsidence, and collapse. Dissolution sinkholes are more common in the eastern portion of Fort Hood, form in areas where there is little soil cover, and rely on water at the surface for widening (Klimchouk et al. 2012). Subsidence sinkholes form due to gradual

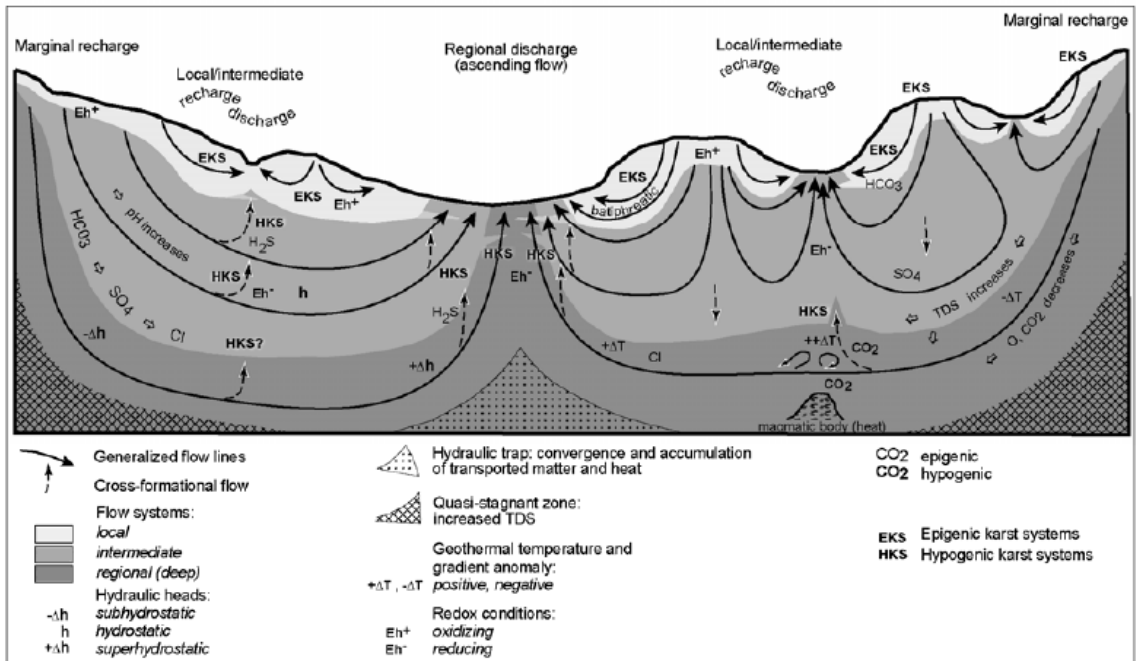


**Figure 9:** A model for the formation of epigenetic and hypogenic karst associated with gravity driven water flow (from Klimchouk et al. 2012).

subsidence and eventual collapse of overburden (Veni 1994). Collapse sinkholes intersect known conduits when roof erosion of subsurface karst features leads to eventual collapse and may be a potential source for cave entrances in the study area (Veni 1994). Collapsed sinks are the most common mapped features on Fort Hood, but this may be due to bias involving investigation of caves rather than minor sinks (Reece 2018).

The study area is not directly connected to the northern extent of the Edwards Aquifer; however, the karst features present in Fort Hood represent a concentrated area of direct recharge sites for water infiltration. Recharge may also accumulate through joint



systems associated with losing streams as water accumulates in the subsurface and travels downward through subsurface conduits and emerges through springs and seeps proximal to recharge sites (Jones 2003). Waters in these seeps may periodically rise to maintain a base level flow during sporadic droughts (Faulkner and Bryant 2018).

## **Resistivity**

Electrical resistivity has been used since the 1830's when natural resistivity anomalies were used to identify sulfide ores. The use of an induced current to determine the location of other ore deposits came nearly one hundred years later in the early 1900's. The use of electrical resistivity in near surface environmental and engineering studies is relatively new, but since its implementation, this geophysical technique has proven to be useful in identifying anomalies in the subsurface (Burger et al. 2006, Loke 1999).

### **Resistivity Theory**

Resistivity is a physical property of a material that measures the relative mobility of electricity through a material in the presence of an electric current. In a resistive environment, the current is impeded and does not propagate effectively through a material. This current, when flowing through a wire, propagates from positive to negative and is measured in amperes (amps). In the subsurface, the measurements are based on potential difference which is usually measured as voltage (V). This potential difference is induced into the ground using a power source such as a battery or generator. The current applied through a given material is proportional to the voltage through Ohm's Law

(Equation 1). The resistance observed is dependent on the composition of the material as well as the dimensions. Resistivity is calculated using this resistance as well as the dimensions of the material (Equation 2 and 3, Burger et al. 2006).

$$\text{Resistance } (R) \text{ (ohm}\cdot\text{m)} = \frac{\text{Potential Difference (Volts)}}{\text{Applied Current (amps)}} = \frac{V}{I} \quad (1)$$

$$\text{Resistance } (R) = \text{resistivity } (\rho) \times \frac{\text{length } (l)}{\text{cross-sectional area } (A)} = \rho \times \frac{l}{A} \quad (2)$$

$$\text{Resistivity } (\rho) = \text{resistance } (R) \times \frac{\text{cross-sectional area } (A)}{\text{length } (l)} = R \times \frac{A}{l} \quad (3)$$

The purpose of electrical resistivity is to measure the potential difference at points on the surface that are produced by directing current flow through the subsurface in order to determine the resistivity distribution throughout the subsurface. Changes in this distribution can be caused by saturation, contamination, mineralogy, soil type, consolidation of sediment, the presence of hydrocarbons, as well as many other factors. When using the AGI SuperSting, the measurement is accomplished by hammering non-polarizable electrodes into the ground at pre-determined intervals and connected with insulated cables to allow for the flow of electricity between electrodes. Measurements are collected when this current is injected into the ground by the current electrodes and collected with the potential electrodes (Figure 10). This current propagates in a hemispherical pattern in the subsurface due to the infinite resistivity of air (Figure 11). The voltage and current values are collected in order to determine the apparent resistivity

of the area. This is not true resistivity and must be inverted in a computer program in order to find the true resistivity (Burger et al. 2006).

Two-dimension (2-D) and three-dimensional (3-D) surveys were conducted in this study and different arrays are commonly used with each of these survey techniques. 2-D surveys are arranged in straight lines and common survey arrangements are Schlumberger, Wenner, and dipole-dipole. 3-D surveys are arranged in an equidistant grid pattern and most commonly use pole-pole, pole-dipole, and dipole-dipole arrays. Each of these arrays are markedly different and have distinct advantages and disadvantages (Figures 12 and 13, Burger et al. 2006).

The basic example of the Wenner array, seen in Figure 12A, involves four electrodes. The inner electrodes are the potential electrodes and the outer electrodes are

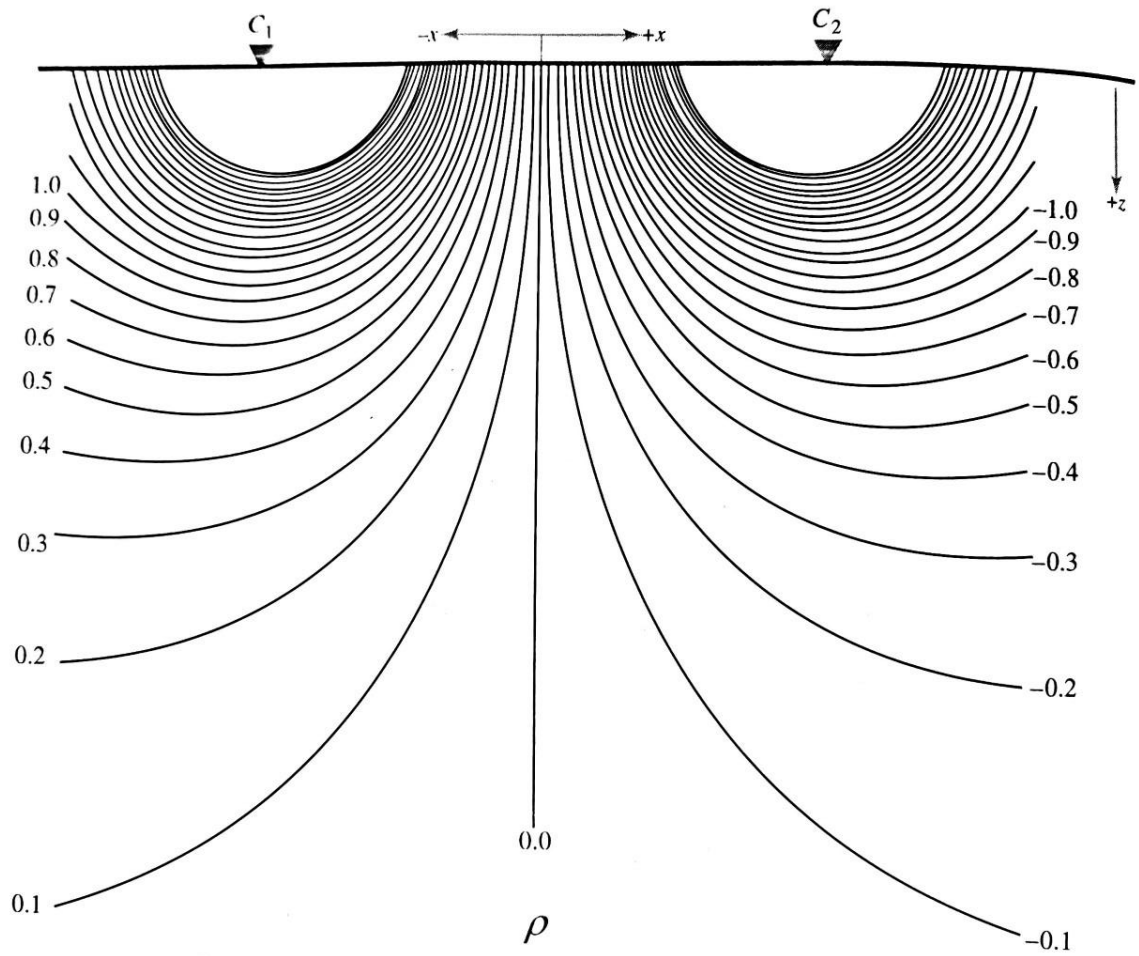


**Figure 10:** A simplified view of electrode placement and current flow paths (from Burger et al. 2006).

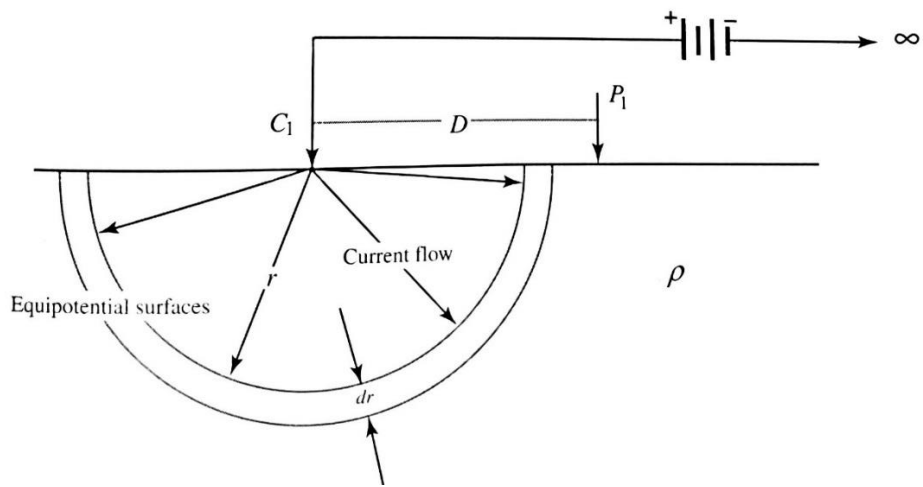


**Figure 11:** A schematic of the hemispherical nature of the current flow patterns of electricity in the subsurface (from Burger et al. 2006).

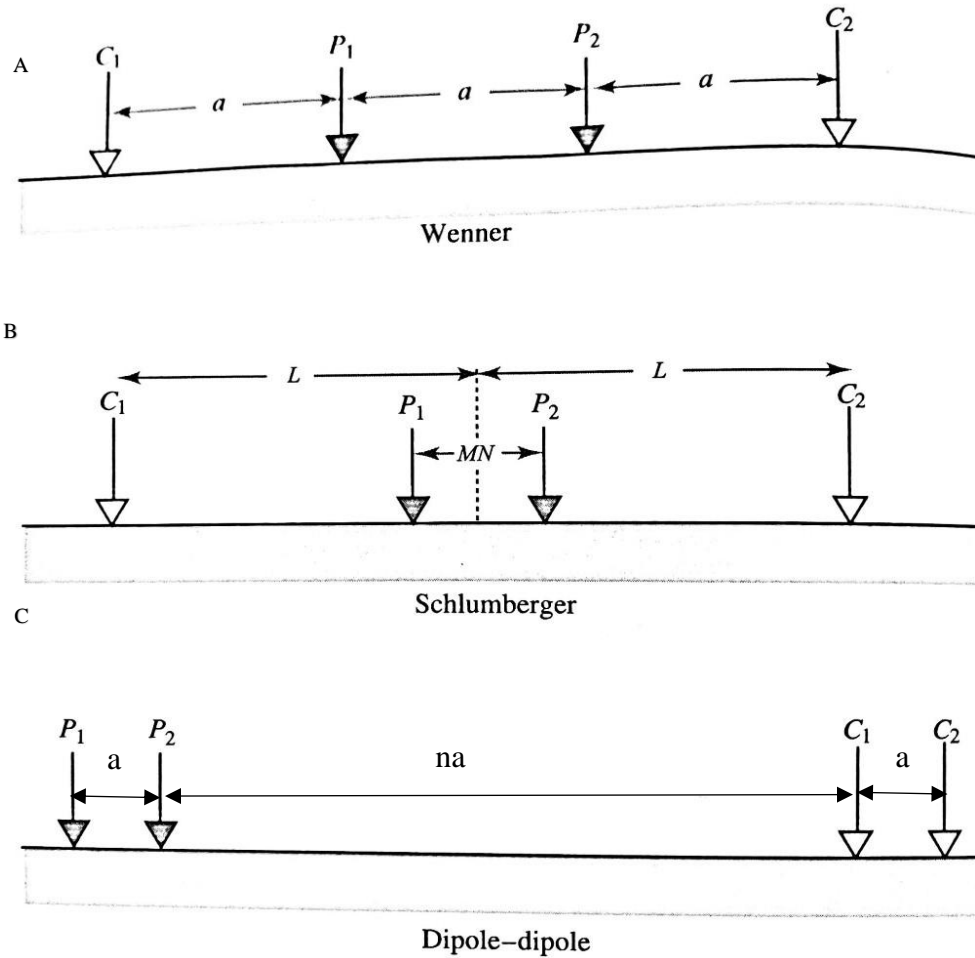


**Figure 12:** Common 2-D survey arrays with **P** being potential electrodes, **C** being the current electrodes, and **a** being the electrode spacing. In B, **MN** is the spacing between potential electrodes that stays constant and **L** is the increasing spacing of the current electrodes (from Burger et al. 2006).

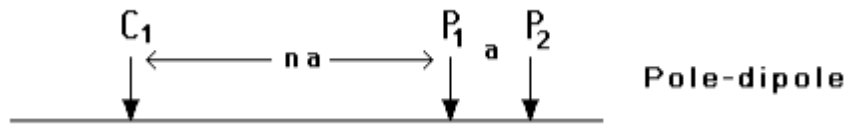


**Figure 13:** General layout of the pole-dipole array where  $\mathbf{a}$  is the spacing between the potential electrode pair ( $\mathbf{P}$ ) and  $\mathbf{n}$  is the multiple of the electrode spacing that is being increased (from Burger et al. 2006).

the current electrodes. In order to collect data throughout an area, the electrode spacing, noted as  $\mathbf{a}$  in the figure, is gradually increased while the midpoint of the survey remains the same. This type of survey is valuable for vertical exploration and it always includes shallow measurements. However, this array lowers horizontal resolution and requires the electrodes to be adjusted more times in the field leading to additional labor and time.

The Schlumberger array, seen in Figure 12B, has the same electrode arrangement as the Wenner array. For resistivity measurements to be collected, the potential electrodes on the inside of the survey remain in the same location and the current electrodes are gradually moved away from the center location. This creates data similar to the Wenner array but reduces the labor and time due to fewer movements of the electrodes.

The dipole-dipole array, seen in Figure 12C, is different than the previous two arrays with a pair of potential electrodes and a pair of current electrodes separated from one another. To collect data, these two pairs are gradually moved apart ( $\mathbf{na}$ ) while keeping spacing within the pairs ( $\mathbf{a}$ ) constant. This allows for the inspection of a cross-section of the earth and the horizontal resolution is greatly increased. The signal strength

decreases drastically with depth and should be used for only near surface investigations (Burger et al. 2006).

The 3-D survey arrays differ slightly from the 2-D arrays. The pole-pole array has one current electrode and one potential electrode that are gradually moved apart. This survey does not feasibly exist because another electrode would have to be included at an infinitely far distance from the first current electrode. However, some studies that attempted to utilize this survey array, using a significantly spaced second current electrode, showed that this type of survey array had poor horizontal resolution and distorted subsurface features. The pole-dipole array, seen in Figure 13, is a solution to the problems with the pole-pole array. This array has one current electrode and two potential electrodes, and these are moved apart in increments. Due to the asymmetrical nature of this survey, another current electrode must be placed significantly far away from the first, but not as impossibly far as in the pole-pole array. The pole-dipole survey also enhances the horizontal resolution seen in the previous array. The dipole-dipole array in the 3-D set up is similar to the 2-D set up, but the electrodes are placed in a grid pattern rather than a straight line and the spreading of electrodes occurs radially. This array is most accurate when used in grids larger than 12x12 electrodes. These surveys can be accomplished by creating a fluid path with electrode cables so that all lines in the grid are connected or by combining a series of parallel 2-D lines (Loke 1999).

Whether implementing the 2-D or 3-D methodology for a survey, there are several factors to consider, including knowledge of the target anomalies, sensitivity and



disadvantages of the array to the geologic features present, the geological environment, and the project budget (Zhou et al. 2002). For the anomaly itself, the size, shape, depth and resistivity contrast must be taken into consideration (Majzoub 2016). Recent studies have determined that dipole-dipole array is the most effective in determining sinkhole collapse areas. This survey is most sensitive to vertical boundaries but is more likely to be affected by near surface variation noise (Majzoub 2016, Redhaounia et al. 2015, Farooq et al. 2012, Youssef et al. 2012, Zhou et al. 2002). Due to the effectiveness of this array type in sinkhole collapse areas, the dipole-dipole array was used to determine the probability of continuation of the cave features in the Shell Mountain study area.

### **Resistivity and Karst**

Karst studies have utilized geophysical techniques for many years that have proven to be effective in delineating subsurface cavities. Though many different geophysical methods have been implemented in the search for subsurface karst, electrical resistivity yielded high reliability and accuracy in determining the location of passages filled with either ground water or clay (Park et al. 2013). Park's (2013) study was conducted in a karst rich area in the southwest portion of the Korean peninsula and determined low resistivity cavities were able to be imaged successfully. Other studies that included passages that were not infilled determined that void space is able to be imaged using this technique as well (Majzoub 2016, Redhaounia et al. 2015, Farooq et al. 2012, Youssef et al. 2012, Zhou et al. 2002).

## **METHODOLOGY**

### **Light Detection and Ranging (LiDAR)**

A detailed LiDAR analysis was conducted in the 25,000 m<sup>2</sup> area surrounding the known karst features of Fern Cave and Brokeback Cave to determine if there were surficial karst features that could be associated with these known caves. The anomalies documented in these surveys were then used to determine the placement of the resistivity surveys in order to identify subsurface features. The elevation data derived from LiDAR were also used for terrain corrections for the resistivity data and accurate geolocation of known cave entrances.

### **LiDAR and Digital Elevation Model Processing**

LiDAR used for this project was collected by Quantum Spatial under contract from the U.S. Army Corps of Engineers in March 2015 (Quantum Spatial 2015). The goal of this project was to produce high resolution geospatial data from airborne LiDAR surveys across Fort Hood Military Installation. This was accomplished by flying 48 flight lines that covered 880 km<sup>2</sup> with 70 control points. The collected data was processed to accurately define the GPS location and correct for variations associated with the motion of the aircraft during collection. This resulted in data calculated to have a horizontal

resolution of 0.52 meters, vertical resolution within 10 cm and a 95% confidence level (Quantum Spatial 2015).

Using the techniques detailed by Ehrhart (2016) and Reece (2018), the LAS bare ground dataset grids collected by Quantum Spatial associated with the two known cave features were uploaded in the ESRI ArcMap software and converted to a multipoint dataset using the *LAS to Multipoint* tool. This multipoint dataset was then converted to a digital terrain model by implementing the *Create a New Terrain Wizard* using a point spacing of 0.5 meters. The *Terrain to Raster* tool was then used to create the digital format for further analyses using the nearest neighbor interpolation method. Cell size was determined by the horizontal resolution of the LiDAR and was set to 0.5 meters. This process resulted in the creation of the Digital Elevation Model (DEM) that was used for the remainder of the analyses. (Reece 2018, Ehrhart 2016; Figure 14).

The DEM was analyzed using tools within the *Hydrology* toolbox in ESRI ArcMap in order to determine the presence of potential karst features. The *fill* tool was utilized to determine areas that did not have a flow direction and would be natural places for potential water accumulation (ESRI 2019). The next step was to create a fill-difference raster to isolate possible depressions. This was accomplished by using the *Raster Calculator* tool to subtract the original DEM from the filled DEM (Figure 15). This created a raster of isolated depressions that could be further analyzed. Depressions

that were below the vertical resolution of the LiDAR were removed using the *Raster Calculator SetNull* function to set values within the fill-difference raster that were less

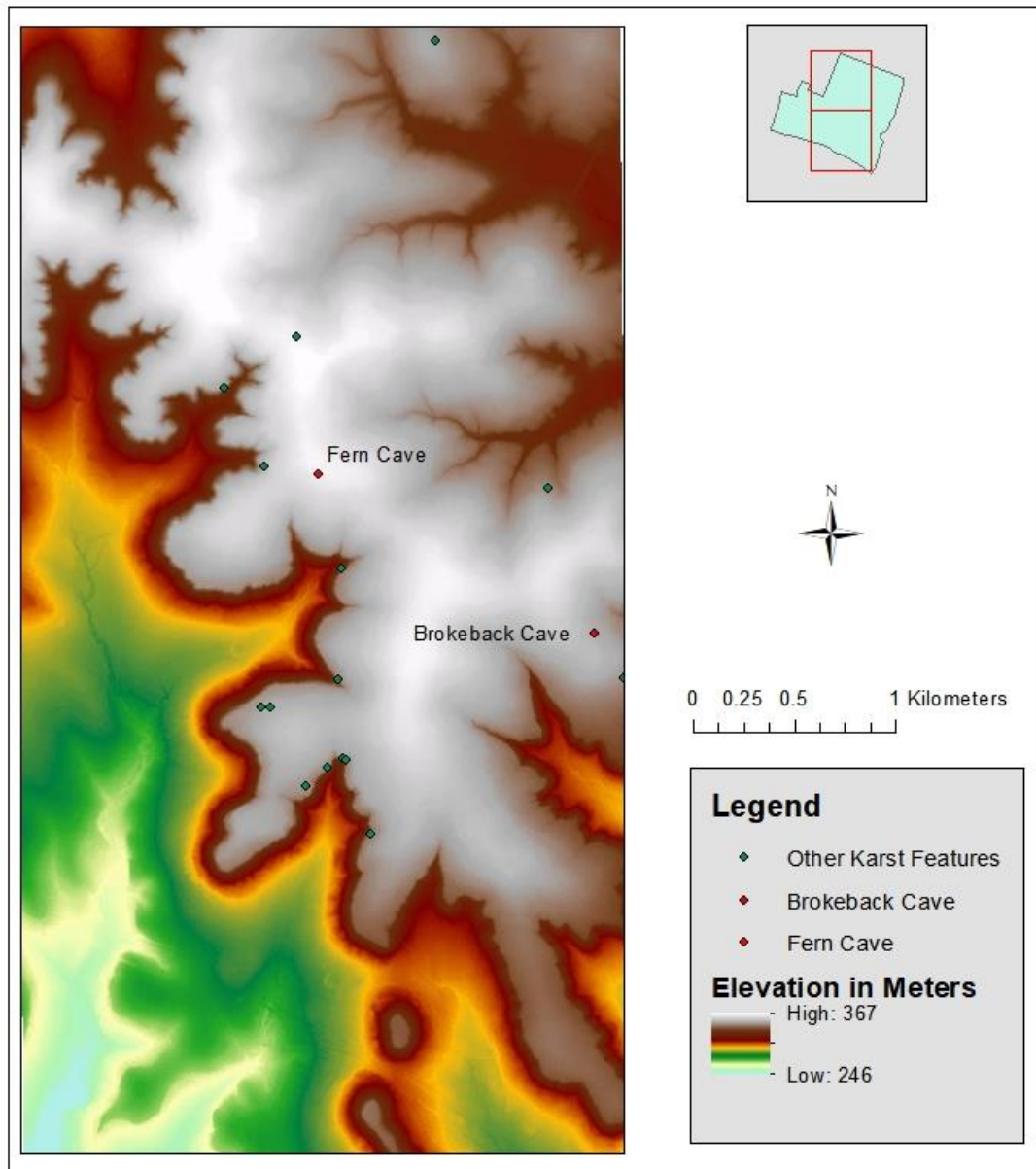


**Figure 14:** Digital Elevation Model (DEM) of LAS grids e04 and f04, areas surrounding Fern and Brokeback Caves (modified from Quantum Geospatial 2015).

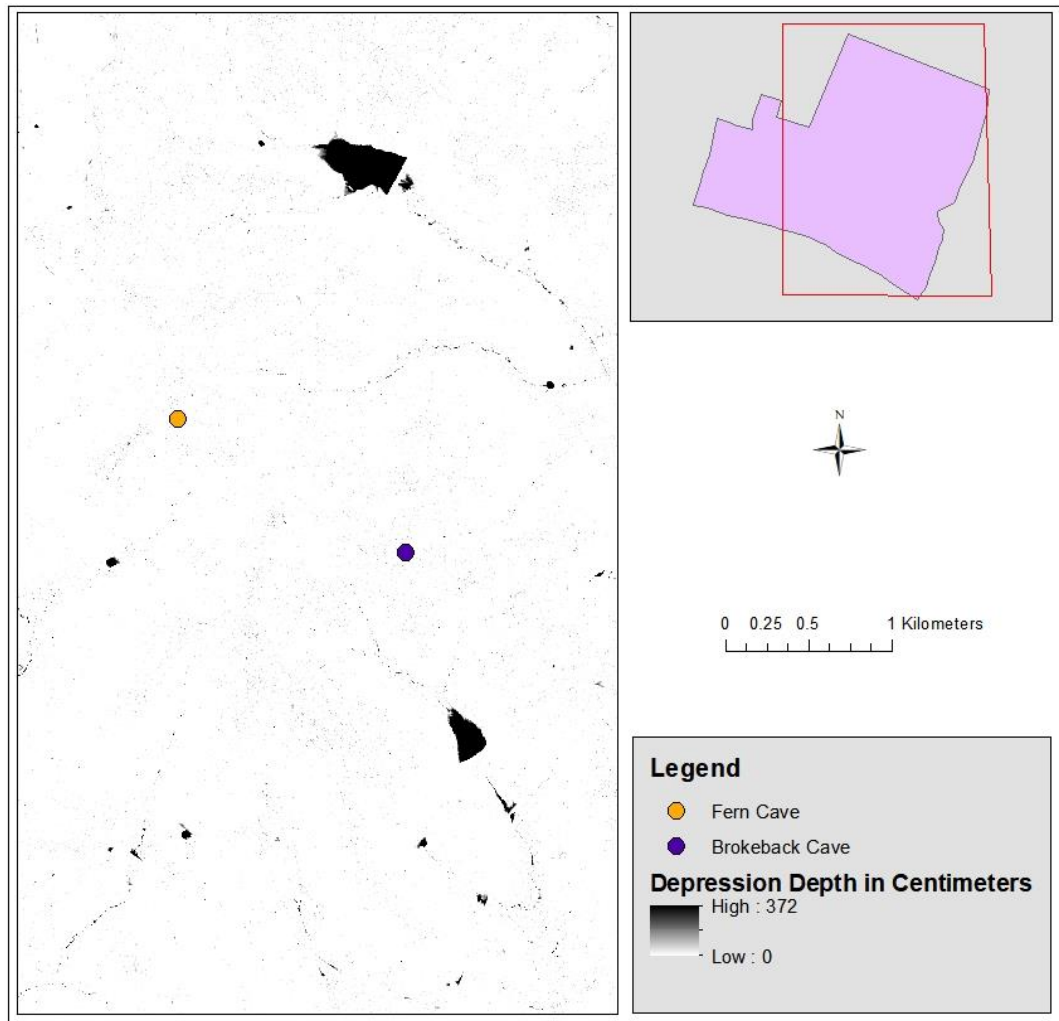


**Figure 15:** Fill-difference raster for LAS grids e04 and f04 showing depth of potential depressions in meters (modified from Quantum Spatial 2015).

than 10 cm to null or no data. This was necessary to reduce artifacts, and exclude features that could not be accurately resolved by LiDAR. The raster was then converted from float to integer to facilitate the *Raster to Polygon* tool. This allowed for the depressions to be drawn as polygons to conserve their shape. The polygons were then buffered and

dissolved to individual features using the *Buffer* tool. Then the *Zonal Statistics as Table* and *Minimum Bounding Geometry* tools were used to add these polygons to a shapefile that included their spatial statistics and geometry (Figure 16). Finally, the grids were cropped using the *Clip* tool so that the DEM, depression shapefile and all associated data were within the 25,000 m<sup>2</sup> radius around the known karst features (Ehrhart 2016; Figure 17).

Streams and other waterways in the area were delineated using the *flow direction* and *flow accumulation* tools in ArcMap. This created a raster of the streams that was then transformed to a polyline shapefile and a 5-meter buffer from the centerline was applied to the lines (Ehrhart 2016, Figure 18). Major and minor roads were delineated using a Color Infrared image (CIR) of the study area and a polyline shapefile was created for both features (Reece 2018. United States Department of Agriculture 2018). A 5-meter buffer from the centerline was applied to the major roads and a 2-meter buffer from the centerline for the minor roads to include depressions caused by vehicles leaving the roadway (Figure 19). Landcover classification was completed using the *classification* tool bar in ArcMap. Signature samples were chosen to represent vegetation and bare ground classes. Each of these contained a minimum of 10 signature polygons and the *interactive supervised classification* was used to determine the landcover classes in each area (Reece 2018, Figure 20). Sinks associated with these features were then removed from the dataset using the *erase* tool. For the landcover filter, only sinks associated with bare ground were removed (Table 1).

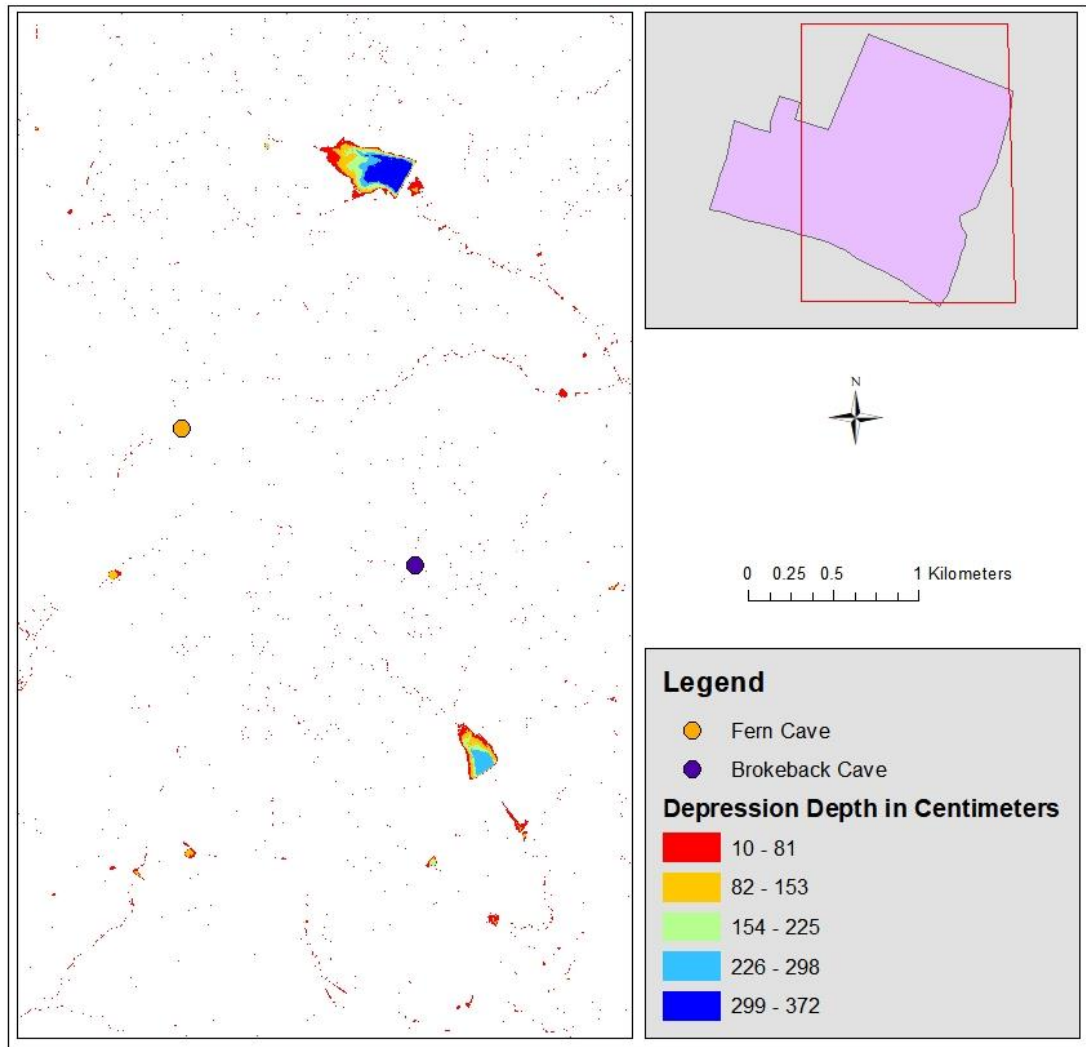


**Figure 16:** Shapefile showing geometry, changing depth and location of depressions (modified from Quantum Spatial 2015).

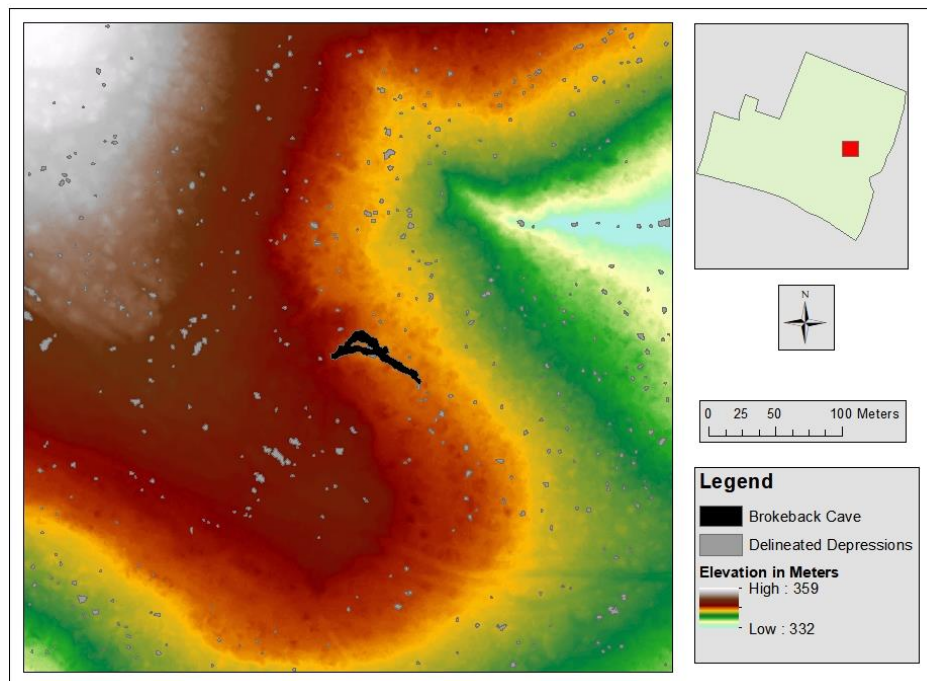
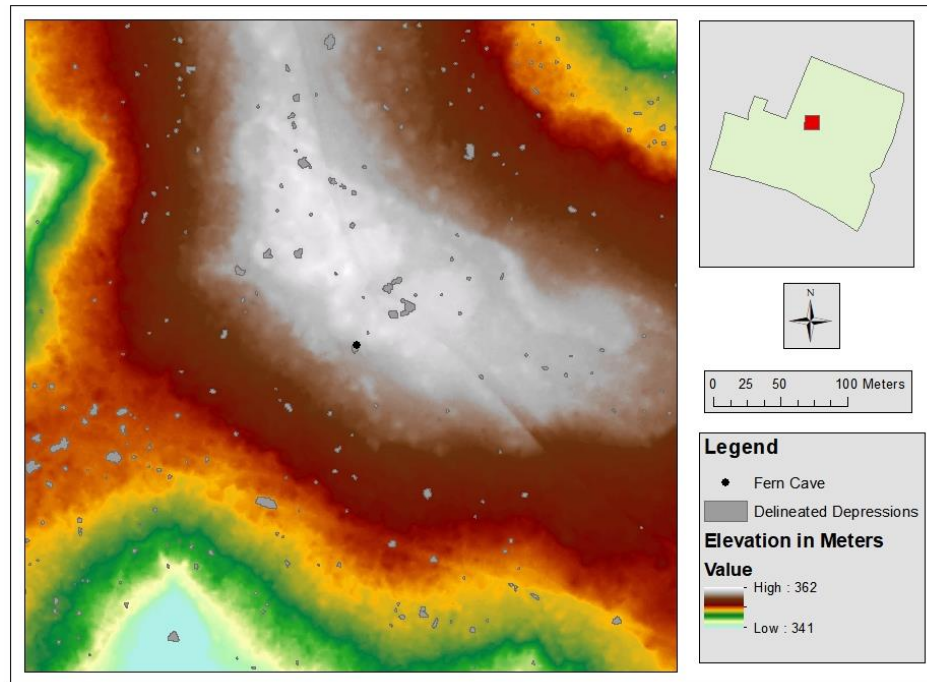


**Figure 17:** Clipped depression analysis for a 25,000  $m^2$  of Fern Cave (top) and Brokeback Cave (bottom) (modified from Quantum Spatial 2015).



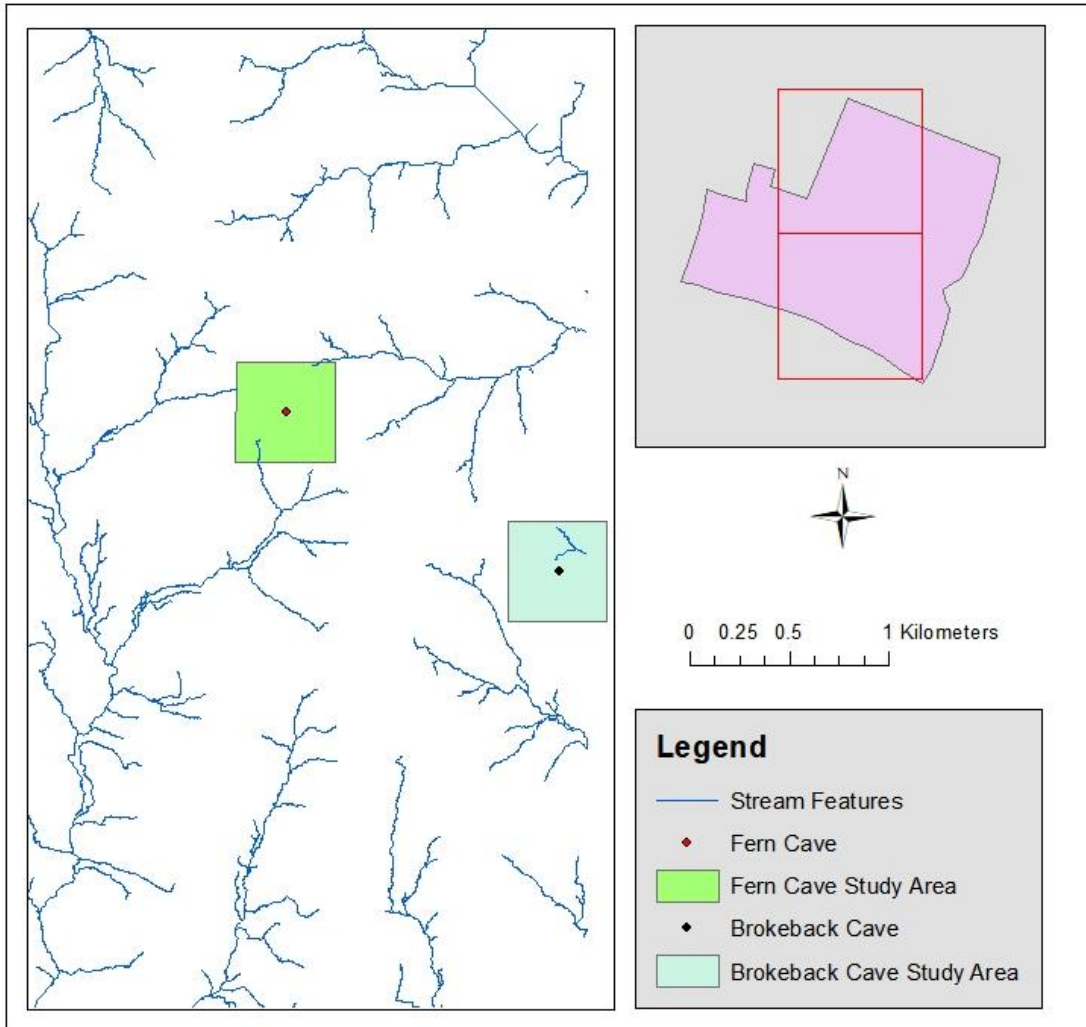


**Figure 18:** Stream features associated with both cave study areas (modified from Quantum Spatial 2015)

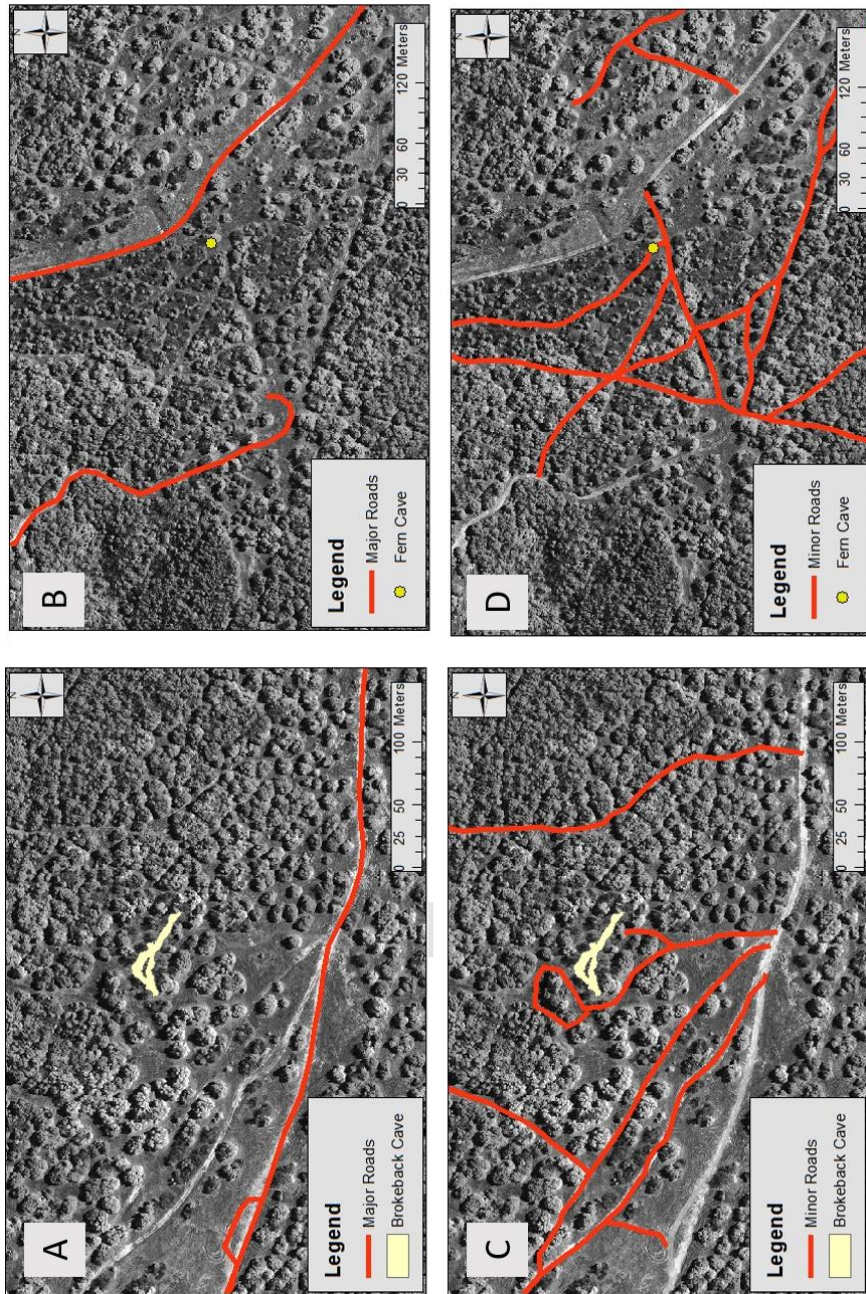


**Figure 19:** Major roads delineated near Brokeback Cave (A) and Fern Cave (B). Minor roads delineated near Brokeback Cave (C) and Fern Cave (D) (modified from United States Department of Agriculture 2018).

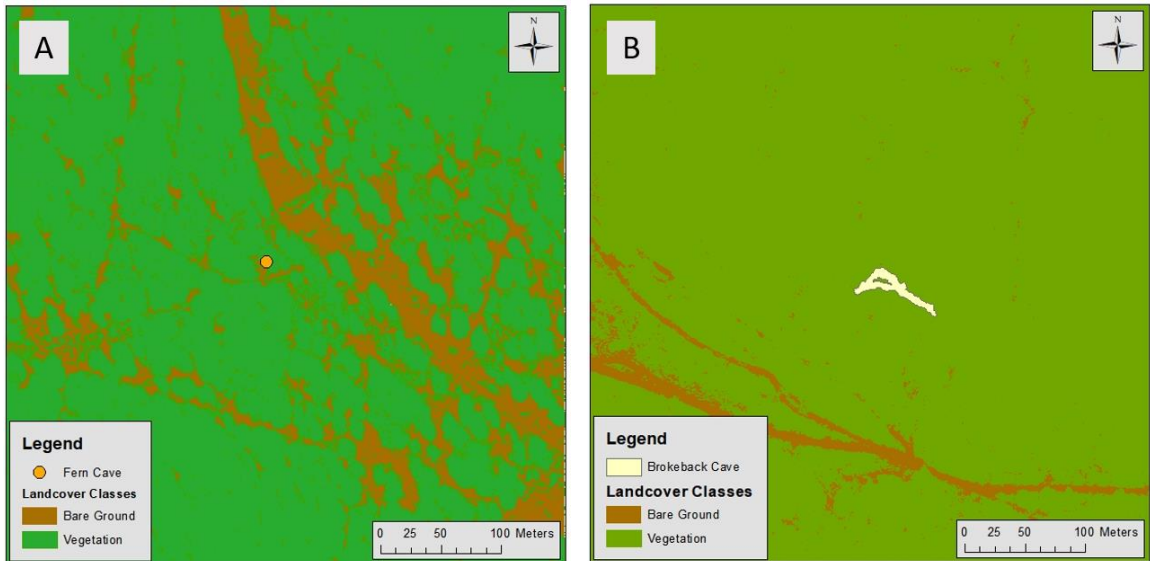


**Figure 20:** Landcover classification maps for Fern Cave (A) and Brokeback Cave (B) (modified from the United States Department of Agriculture 2018).

**Table 1:** Filter classifications and buffer distances applied to remove depressions not associated with karst formation.

FILTER TYPE	BUFFER
Streams	5 m
Major Roads	5 m
Minor Roads	2 m
Land Cover	1 m

Published cave maps from the Texas Speleological Survey (2014) were uploaded to ArcMap, scaled, and aligned to north using the *Scale* and *Rotate* tools on the *Georeferencing* tool bar. The maps were then georeferenced to their locations using known GPS points collected in the field, the LiDAR 3-D point cloud data, a CIR, and the DEM. The use of these four data verification tools allowed for accurate representation of the cave structures in relation to survey locations. The outlines of these caves were then traced and transformed into a new shapefile using the *Editor* toolbar so that the full extent of the caves could be represented and compared to the sinks found through LiDAR processing (Figure 21).

### **Resistivity**

Areas of interest were chosen surrounding Fern Cave and Brokeback Cave due to the high probability of previously undocumented subsurface karst features. Subsurface Direct Current (DC) 2-D and 3-D resistivity analyses were completed using an AGI SuperSting R8 IP/SP system in order to determine subsurface karst potential. Many potential survey areas had to be eliminated due to inaccessibility associated with the terrain, vegetation, and soil cover. Locations of the surveys at both caves took into consideration visible deformation, vegetation cover, proximity to known cave entrances, depressions noted on the LiDAR analyses, and soil depth.



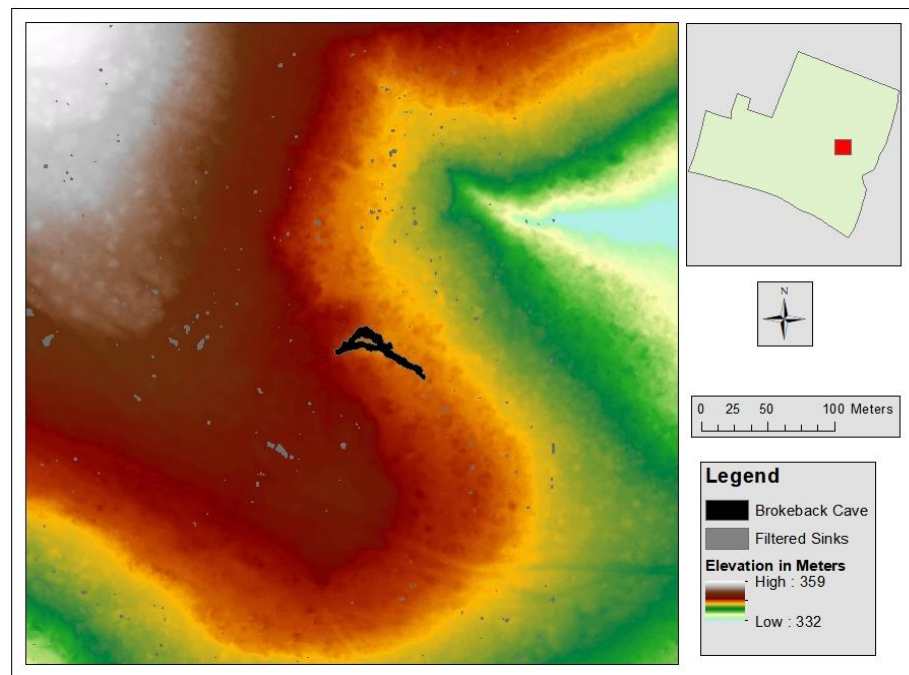
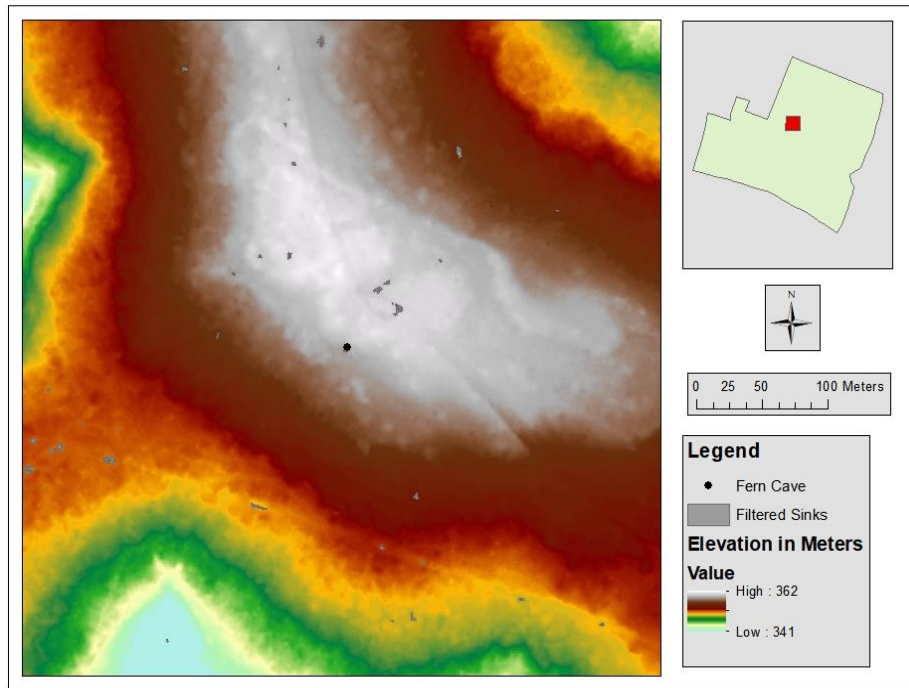


**Figure 21:** DEM showing the location of Fern Cave (top) and Brokeback Cave (bottom) in relation to possible depressions (modified from Quantum Spatial 2015).

## Command Files

Before going to the field, command files were created so that the automatic mode of the SuperSting could be implemented to complete the survey using the specified parameters. This was accomplished using the Administrator function of the EarthImager 2D and 3D software (Figure 22). These commands were downloaded onto the SuperSting via a data cable from the computer and contained vital information including array type, number of electrodes, and electrode spacing. 2-D and 3-D surveys performed during this study deployed 56 electrodes. For 2-D surveys the dipole-dipole array was chosen and spacing between the individual potential ( $P_1$  and  $P_2$ ) and transmitting electrode pairs ( $C_1$  and  $C_2$ ) was kept constant ( $a$ ), but the distance between the pairs were increased gradually by a factor of  $n$  (Burger et al. 2006; Figure 23). The electrode spacing was set to a minimum of one meter and maximum of six meters. The 3-D surveys used the equivalent array of radial dipole-dipole. This array type increased electrode spacing similarly to the dipole-dipole but operated in a grid containing four rows of 14 electrodes at two meters spacing. The increase of the spacing was done automatically using the switch box which removed the need for repositioning of the electrodes in the field. The dipole-dipole array geometric factor  $k$  is determined using the following equation:

$$k = \pi n (n+1) (n+2) a \quad (4)$$

Where  $n$  is the geometric distance factor, and  $a$  is the separation between electrode pairs with a maximum  $a$  value of six and maximum  $n$  value of eight used to complete this

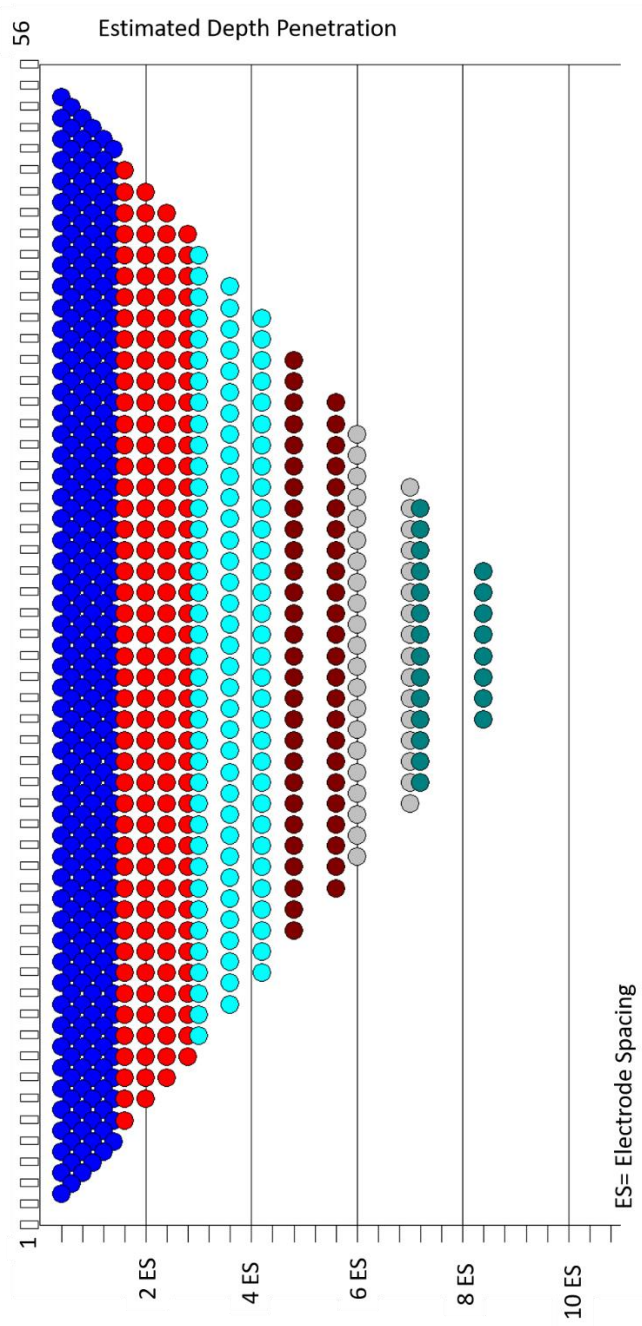


**Figure 22:** Command file used for 2-D surveys.

study. The geometric factor was used with the resistivity measurements to calculate the apparent resistivity.

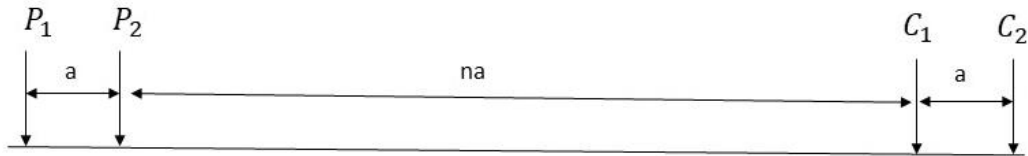


**Figure 23:** A schematic of the 2-D dipole-dipole array.  $P_1$  and  $P_2$  are the potential electrodes,  $C_1$  and  $C_2$  are the current electrodes,  $a$  is the electrode spacing, and  $n$  is the factor influencing the increasing distance between the two pairs (modified from Burger et al. 2006).

### Data Acquisition

The length and positioning of the 2-D surveys were determined by the proximity of the known cave features, areas indicated on the cave maps for possible continuation, and karst potential areas indicated on the LiDAR survey. Due to density of vegetation surrounding the cave features, surveys were limited to areas that had been used as vehicle trails and those that were dominated by grassy vegetation. Length restrictions due to vegetation determined that survey parameters should include a 56-electrode array at one meter spacing between electrodes in order to cover the greatest possible area. The survey locations were altered slightly so that adequate soil cover was present for proper coupling of the electrodes. These electrodes were implanted in the soil at the appropriate spacing



and cables were connected to each electrode. When possible, 3-D surveys were in the same general area as the 2-D surveys for data continuity (Figures 24 and 25).

### **Field Setup**

Both 2-D and 3-D surveys used a total of four sections of electrode cables that were numbered sequentially 1-56 and each cable section included 14 electrode connectors. Cable 1 (1-14) and cable 2 (15-28) were considered low address cables and cables 3 (29-42) and cable 4 (43-56) were considered high address cables. The stainless-steel electrode stakes were hammered into the ground and connected sequentially to the electrodes on the cables. Cables 1 and 2 were connected sequentially, and the end of cable 2 was connected to the low address input on the SuperSting 1-56 switchbox. The connector closest to electrode 29 on cable 3 was connected to the high address input on the switch box and the opposite end was connected to cable 4. The connector nearest electrode 1 on cable 1 and electrode 56 on cable 4 were left unattached. The switchbox connected to the SuperSting module by a data cable and the module was powered by two 12 volt deep-cycle marine batteries (Figures 26 and 27).

Survey files were created using the command files that had been downloaded onto the SuperSting prior to field work. These command files contained valuable information about survey parameters such as array type but lacked essential programming information

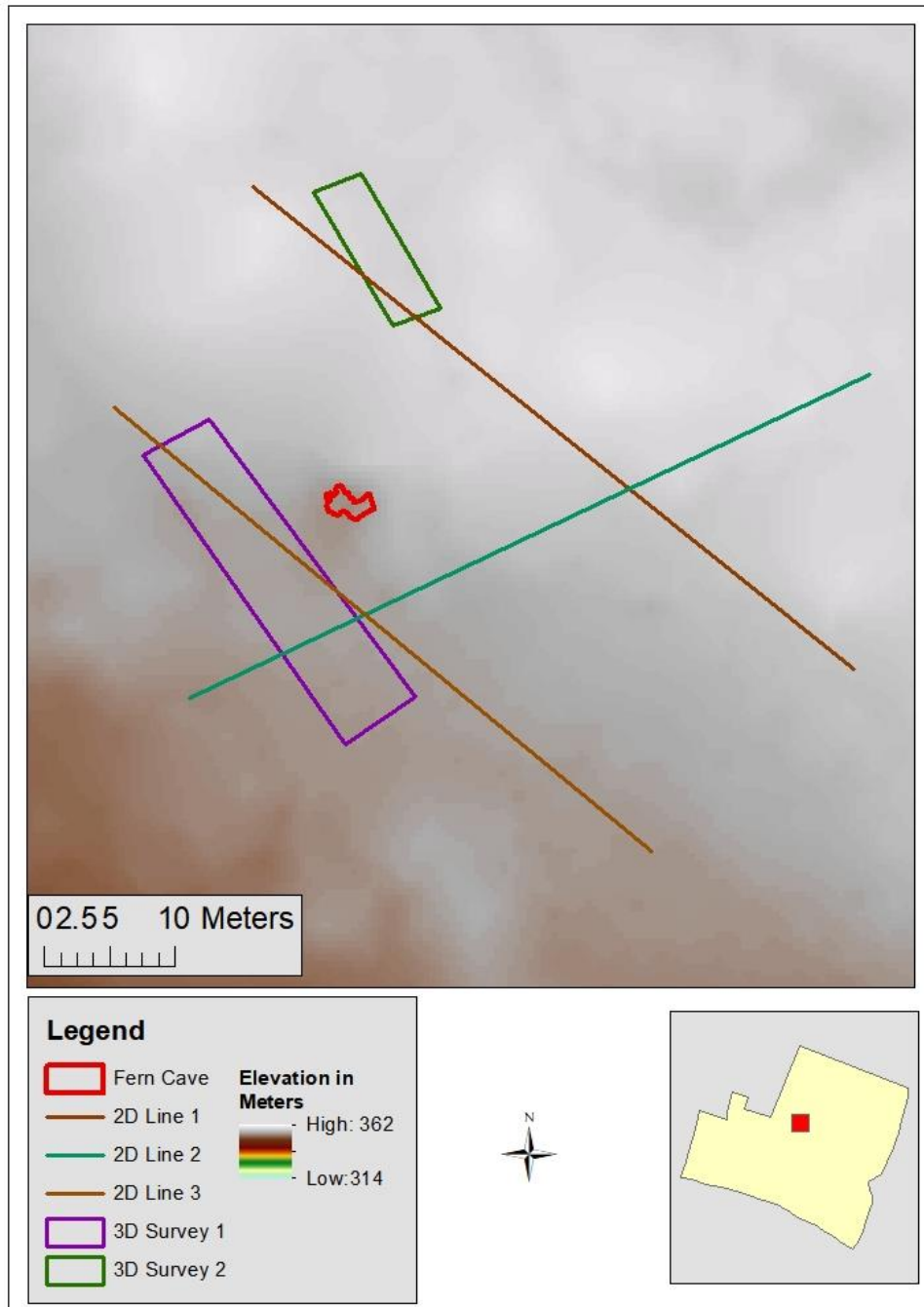


**Figure 24:** 2-D and 3-D survey lines surrounding Fern Cave (modified from Quantum Spatial 2015).

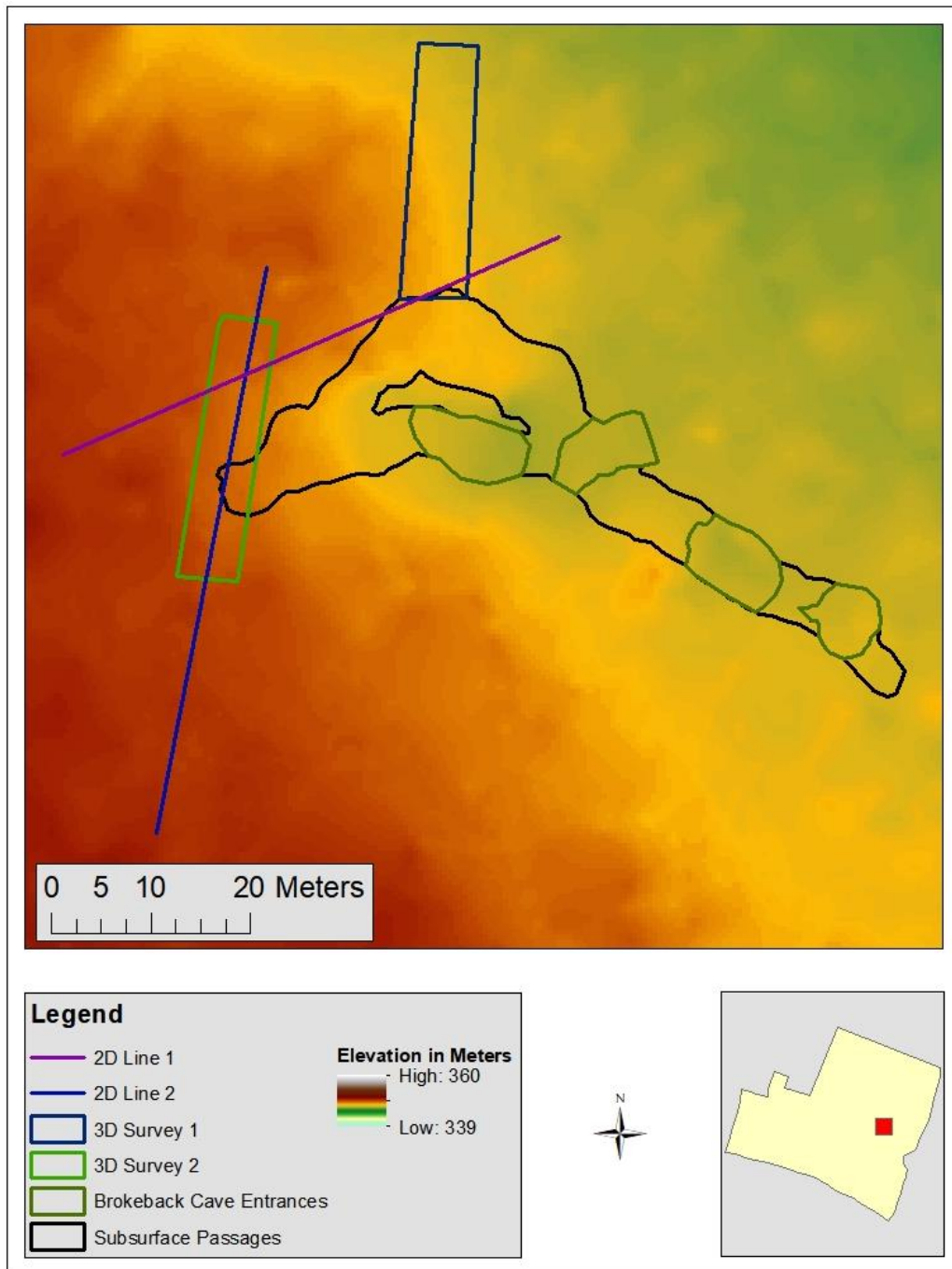


**Figure 25:** 2-D and 3-D survey lines surrounding Brokeback Cave (modified from Quantum Spatial 2015).

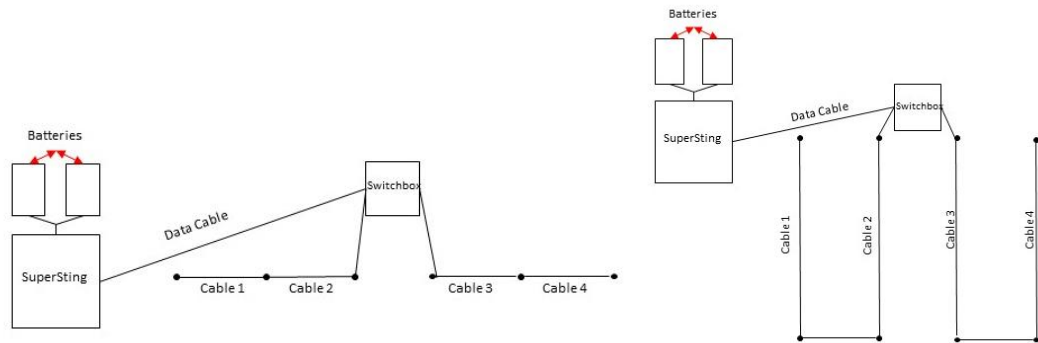


**Figure 26:** A schematic showing SuperSting and cable setup for a 2-D survey (left) and 3-D Survey (right).

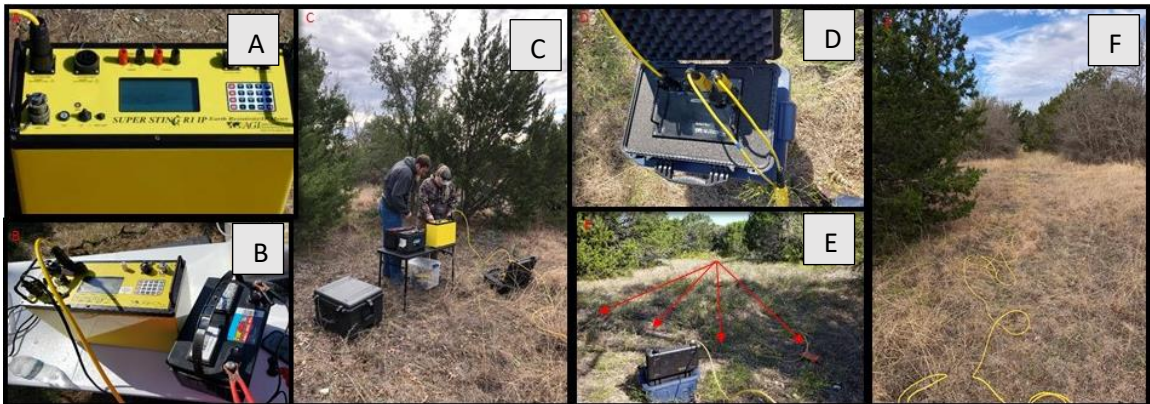


**Figure 27:** **A)** SuperSting module with data cable connected in upper left corner. **B)** SuperSting Module with batteries connected. **C)** Typical field set up with SuperSting, field computer, power source and switchbox. **D)** Switchbox showing cables 1 and 2 connected to low address, cables 3 and 4 connected to high address and data cable connecting to Super Sting. **E)** Typical field view of a 3-D survey grid with cables marked by the red arrows. **F)** Typical view down a 2-D survey line, image taken from electrode 56.

necessary for the module to complete the survey in automatic mode. Meters was selected unit of measurement, and electrode spacing (scaling factor) was set to one meter for 2-D surveys and two meters for 3-D surveys. The remainder of the settings were roll-along survey was turned off, a maximum of 2% error between measurements, and contact resistance maximum of 2000 mA. Once these settings were selected, the switch box was selected from the menu and programmed to be *Switchbox 26*, which informed the SuperSting module that the switchbox was connected after electrode 26. Then the electrode cables sections were entered to inform the module of the number of electrodes per cable (i.e. 1-14, 15-26, 27-42, 43-56) (Advanced Geosciences (AGI) 2005).

Once these parameters were completed, a contact resistance test was conducted to ensure there was acceptable coupling to the ground and that the cables were connected correctly. If the contact resistance was greater than 2000 mA, the electrode was adjusted to a better position, and/or the electrode was planted more firmly in the soil. When the contact resistivity test was satisfied, the survey was initiated on the module. While the surveys were being completed, field personnel kept a safe distance from the cables, and moved machinery away from the survey site to ensure that the stability of the cables were left intact. Upon completion of the surveys, data was uploaded to the field computer via data cable from the module for initial processing to take place.

## Processing

Raw data collected during the surveys were uploaded to the EarthImager software and included both the 2-D and 3-D equivalents of the software. Terrain corrections, derived from the DEM created in the LiDAR survey, were applied to the 2-D survey lines to accurately define the topography (Figure 28). When the 2-D data were uploaded, the software automatically created an apparent resistivity pseudosection. The criteria for processing was then determined to invert the resistivity pseudosection in order show the true earth resistivity. Due to the nature of the study, surface settings were used for the initial settings as well as the smooth model inversion. This allowed for the smoothest possible model of the inverted data and the removal of some noise (Figures 29 and 30).

Though the inversion pseudosection shows the true earth resistivity, not all the data aligns with this inversion and results in the root-mean square error (RMSE) percentage. This misfit data is termed noise and can come from a variety of sources including resident signals in the ground, high contact resistivity, and anthropogenic objects in the surrounding area. Some of this noise is filtered in the inversion settings, but not all is automatically removed. To manually remove the noisy data, the data misfit histogram was generated within the EarthImager software (Figure 31). This allowed for a visualization of the data points that did not coincide with the inversion, and for the removal of this data. This removal was done slowly to ensure that artifacts and other errors in the data were avoided. Data was removed until the Root Mean Square Error

```
;TRN File
unit=meters
1
0,361.863922
1,361.861694
2,361.830048
3,361.699097
4,361.670741
5,361.676086
6,361.662323
7,361.548798
8,361.600372
9,361.596130
10,361.595032
11,361.613220
12,361.602417
13,361.609039
14,361.628357
15,361.655853
16,361.684723
17,361.706970
18,361.742157
19,361.722076
20,361.677826
21,361.707489
22,361.741974
23,361.755585
24,361.764313
25,361.655243
```

**Figure 28:** Terrain correction for Fern Cave line 1.

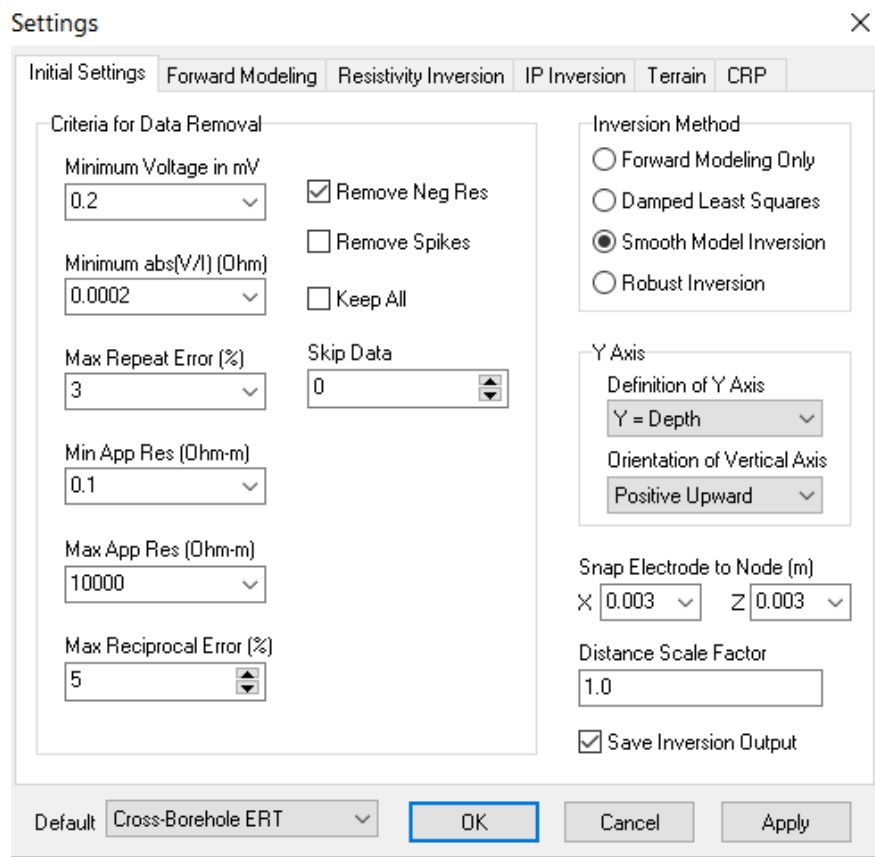


**Figure 29:** Initial settings for the 2-D resistivity surveys.



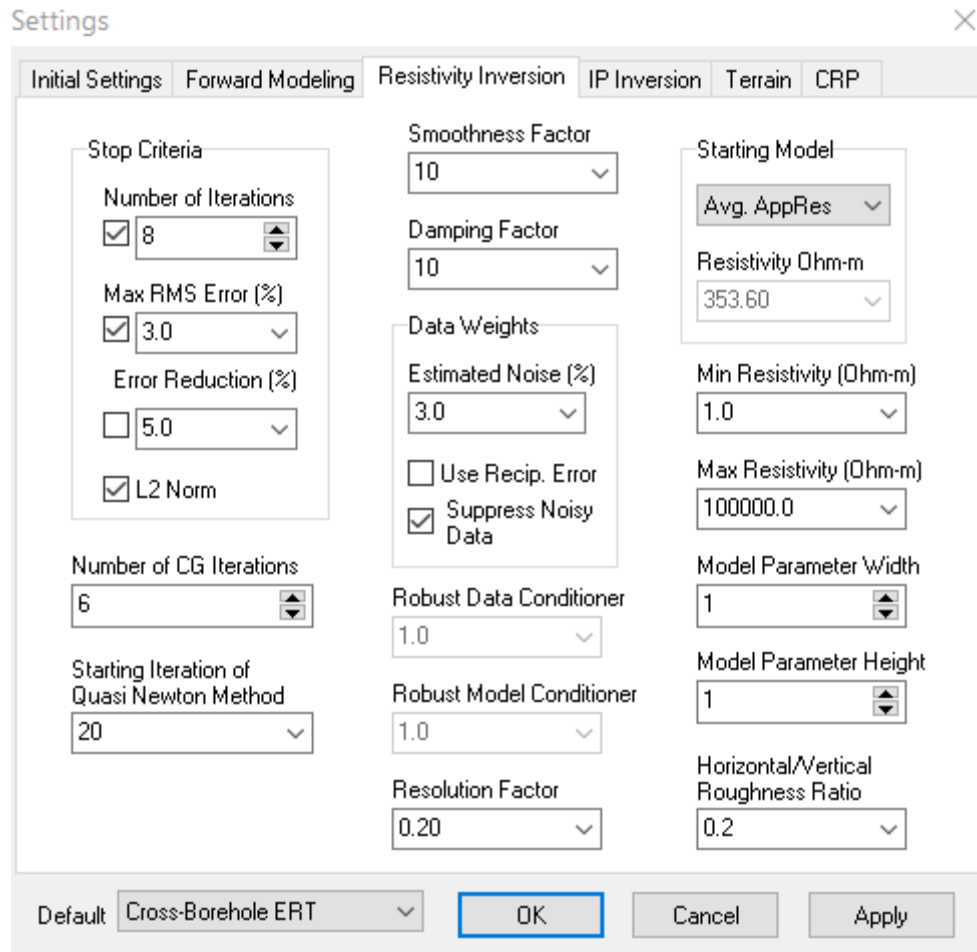


**Figure 30:** Inversion settings for 2-D resistivity surveys.

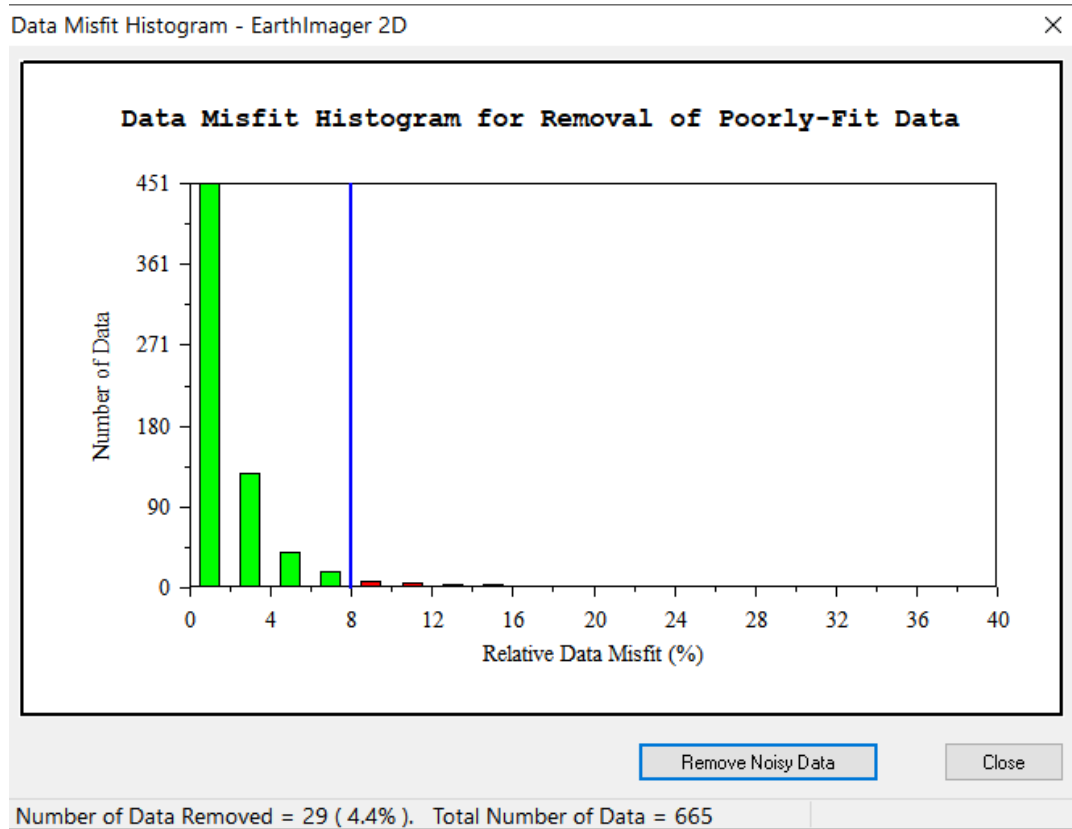


**Figure 31:** Data misfit histogram for Fern Cave line 1 highlighting noisy data.

(RMSE) was less than 10% for each of the survey lines and to ensure that artifacts were avoided, the data misfit cross plot was generated for each line (Figure 32). No more than 10% of the total data was removed from the surveys to reduce bias. A complete data set for each 2-D and 3-D survey can be found in Appendix A.

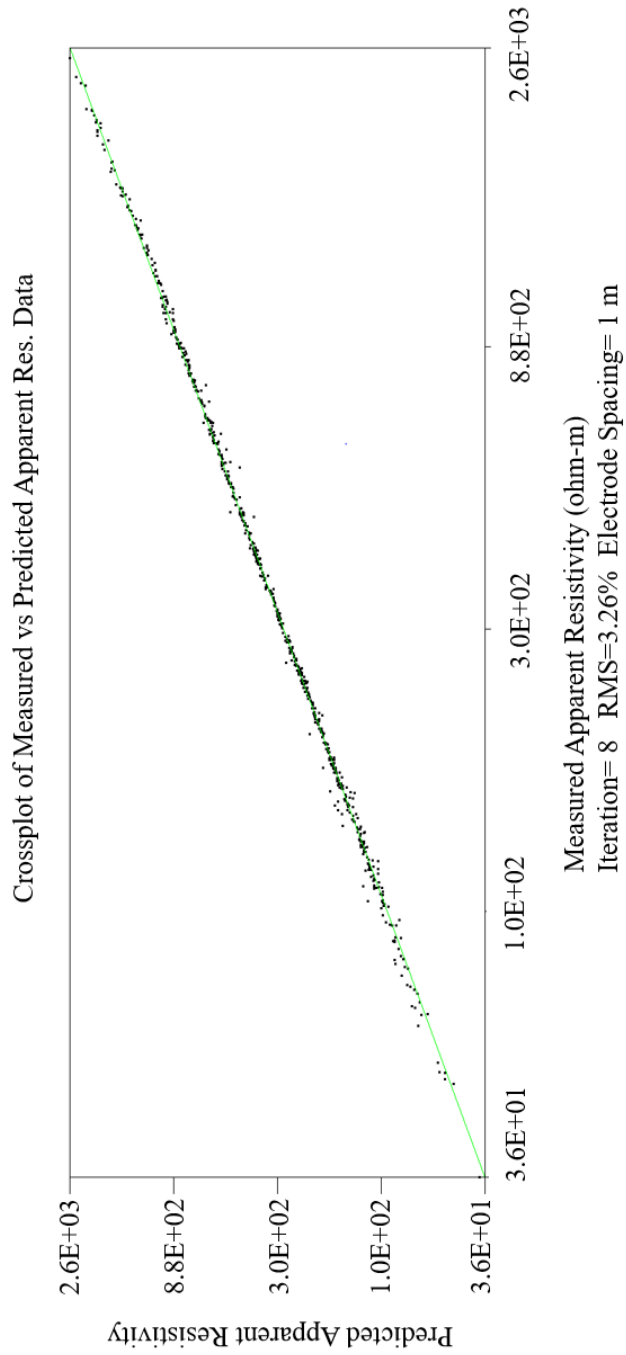


**Figure 32:** Cross plot for Fern Cave line 1 after processing.

The initial processing for 3-D surveys was similar to the steps outlined for 2-D surveys, but additional techniques aided in interpretation of the 3-D data. Static contours for each survey were analyzed and edited to create 2-D images by slicing the 3-D model in either the x-, y-, or z-direction (Figure 33). This allowed for continuity in the data analyses in all directions. The dynamic contour feature is like the static contours but includes two directions at once allowing for internal analyses of the 3-D survey (Figure 34). 3-D contours allow users to highlight certain resistivity values and create 3-D representations of these values (Figure 35). These tools are useful in the determining morphology of potential karst features.

### X Slices of Inverted Resistivity

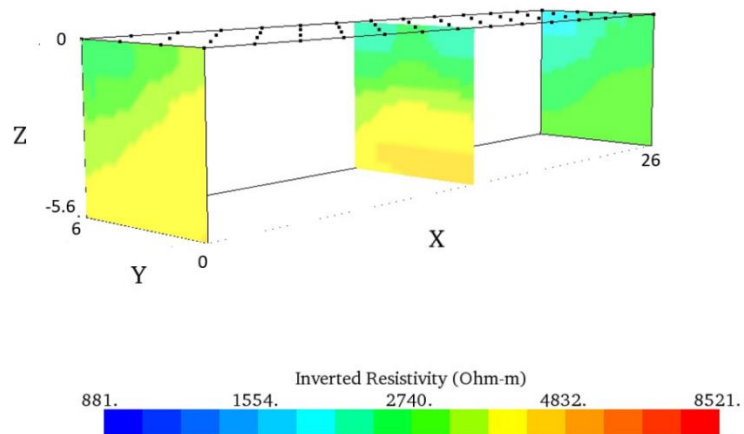


**Figure 33:** Static contours in the x-direction for the first 3-D survey at Fern Cave.

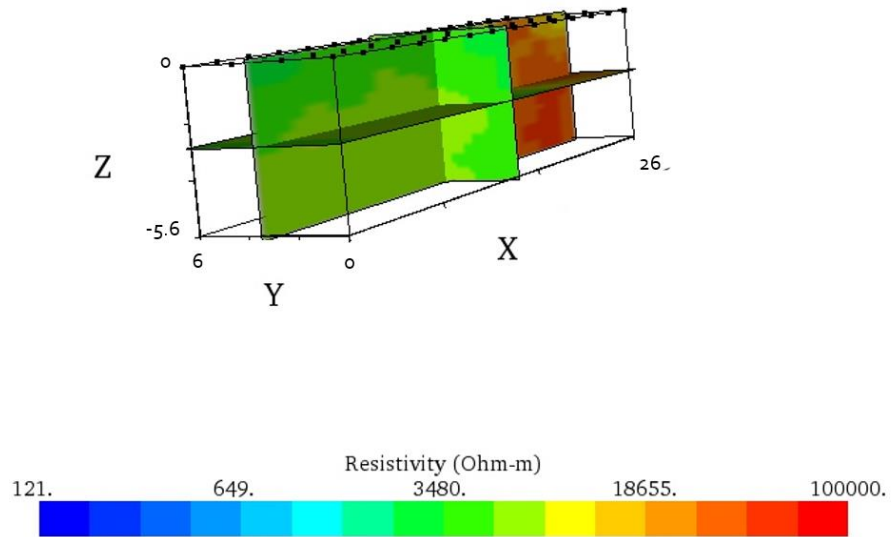


**Figure 34:** Dynamic contour example on the first 3-D survey at Fern Cave.

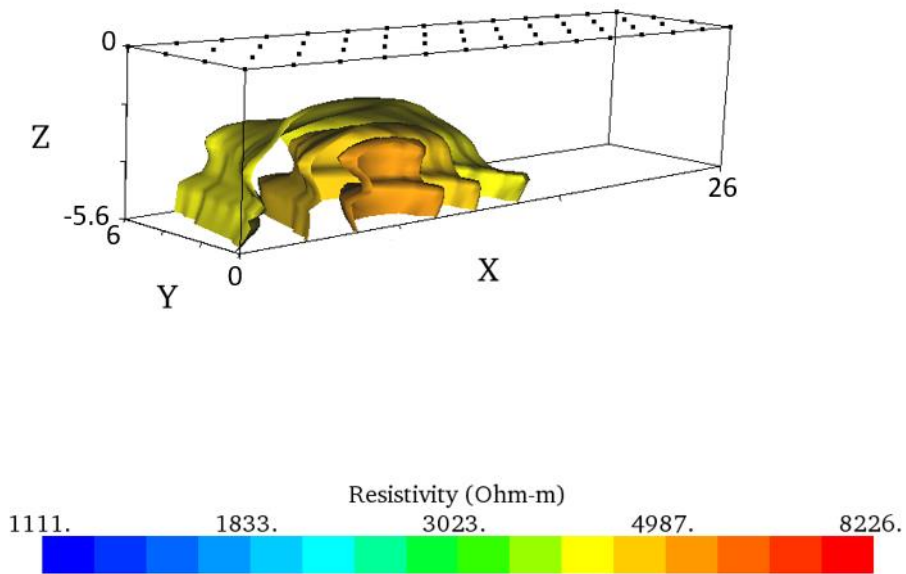


**Figure 35:** 3-D contours for the first 3-D survey at Fern Cave.

## **INTERPRETATION**

All 2-D and 3-D surveys were completed in the days following precipitation in the study area to reduce contact resistivity with the ground surface and reduce coupling errors. The excess moisture may have contributed to misidentification between soil and bedrock; therefore, the survey lines were interpreted to include a saturated and unsaturated boundary rather than a soil-bedrock boundary. The average soil depth at the survey line locations ranged from 20 to 30 centimeters, and this shallow overburden may have contributed to coupling errors when implementing the SuperSting system.

Cross-sections were generated for all 2-D survey lines using estimations derived from cave maps, field images, and observations during field exploration. Resistivity values used for the interpretations of the surveys were based on measurements observed in similar resistivity environments (Redhaounia et al. 2015, Farooq et al. 2012, Youssef et al. 2012). Karst density analyses were completed in the 25 km<sup>2</sup> area encompassing both cave features; these analyses showed an increase in the surface area percentage of karst features following the trend of the plateau edge (Figure 36). Excavation in the areas surrounding Fern and Brokeback caves was not permitted and anomaly interpretations were not verified using this technique.

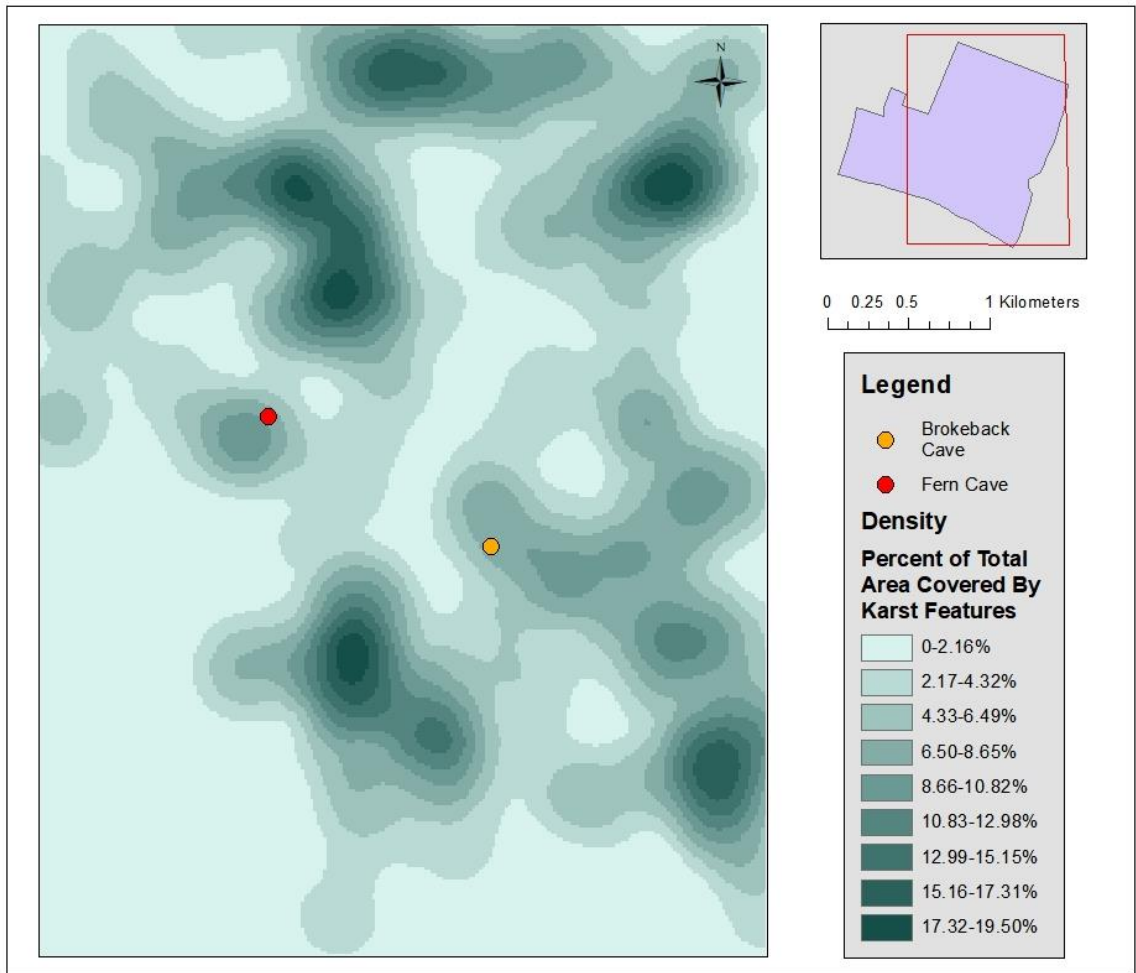


**Figure 36:** Density analysis for 25 km<sup>2</sup> radius including Fern and Brokeback Cave (modified from Quantum Spatial 2015).

## **Brokeback Cave**

The LiDAR karst survey results provided information about 226 depressions in the area surrounding Brokeback Cave. The filtering mechanisms (Table 1) removed sinks that were associated with roadways, water bodies, and other anthropogenic activity in the area, reducing the number of sinks to 190 potential karst depressions. The density model showed the greatest concentrations of karst sinks at areas of high elevation and clustered pockets of soluble rock along the edges of the plateau (Figure 36). The area immediately adjacent to Brokeback Cave showed moderate karst development, although few features were observed in the field (Figure 37 and 38). The open nature of this cave and the ability to enter the portions that were not collapsed allowed this cave to serve as an accuracy assessment for the SuperSting resistivity meter parameters and further characterization of the known cave passages. The overburden in these cave passages were measured from the entrances to the passages with a measuring tape, their morphology derived from the cave map and direct observation, and their locations along the survey line were noted prior to the survey analyses. 2-D survey lines were completed on the northern and western extent of Brokeback Cave. Cross-section diagrams were constructed along both 2-D survey lines (Figure 39).

Areas of high resistivity, denoting the probability of a cave passage, were delineated at the appropriate depths, size, ceiling height, and locations along the survey line in both 2-D survey lines. In addition to these known passages, the first survey line



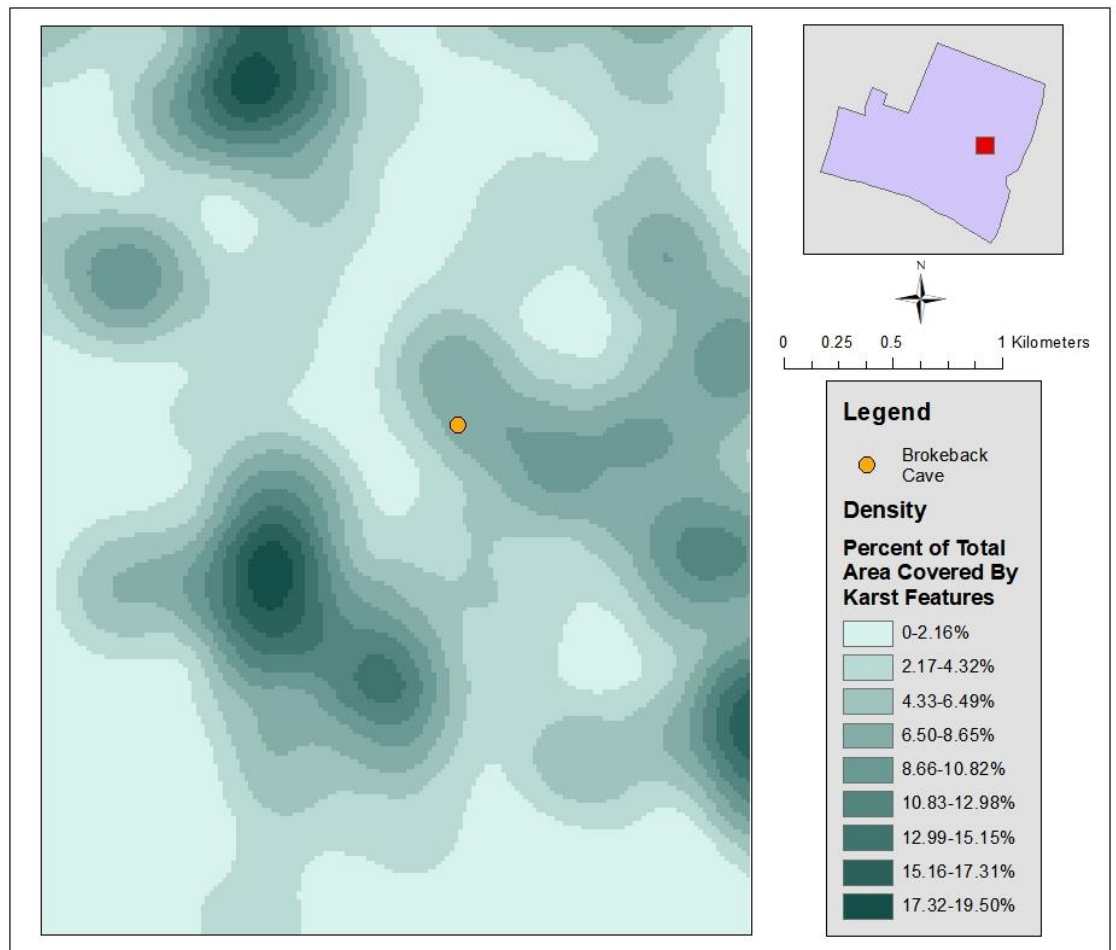


**Figure 37:** Density map of karst features in the 500-meter radius of Brokeback Cave (modified from Quantum Spatial 2015)

**BROKEBACK CAVE**  
**Fort Hood Military Reservation**  
**Coryell County, Texas**

Brunton and Tape Survey  
17 March 1963  
J. Arnold, D. McKenzie, J. Reddell  
Drafted by A.R. Smith

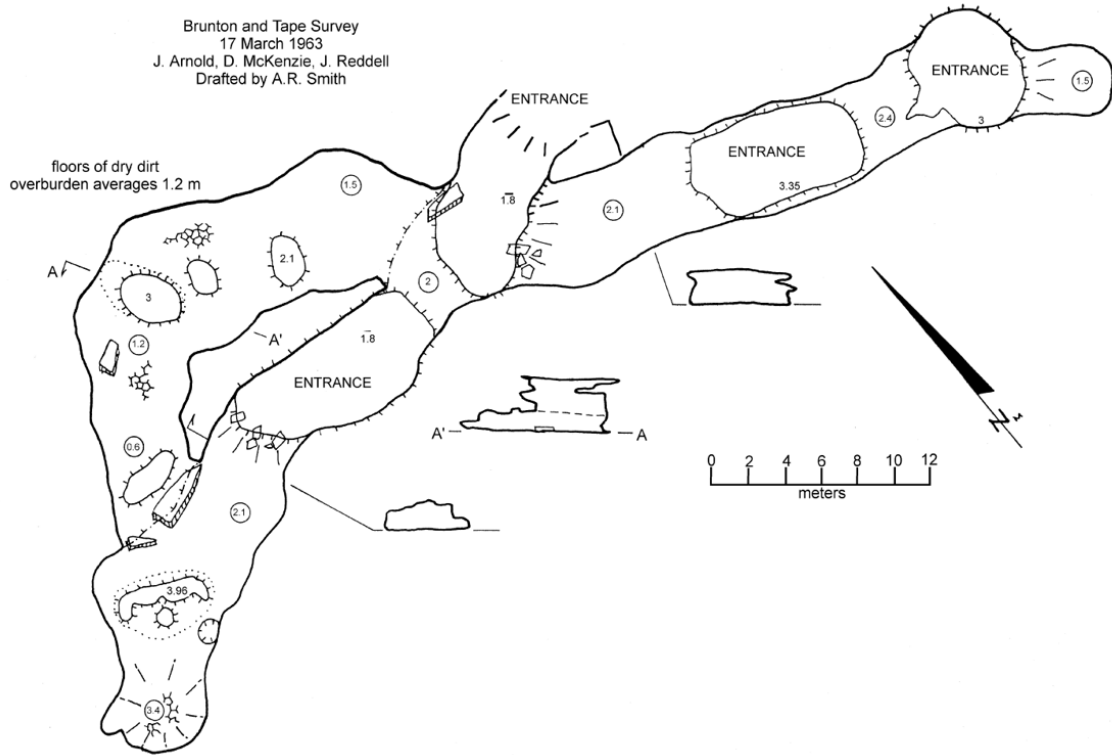


**Figure 38:** Brokeback Cave map (Texas Speleological Survey 2014).

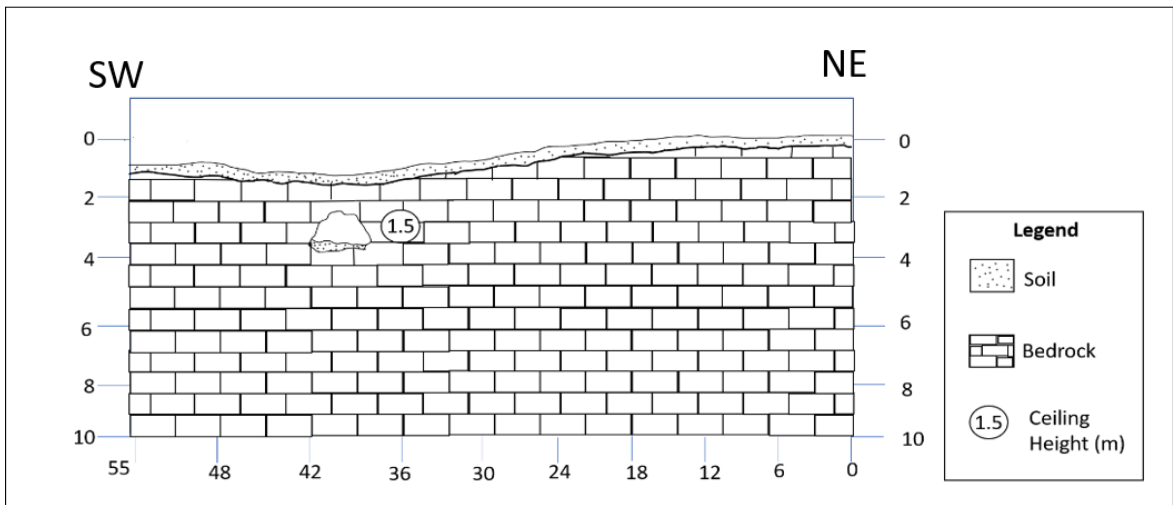
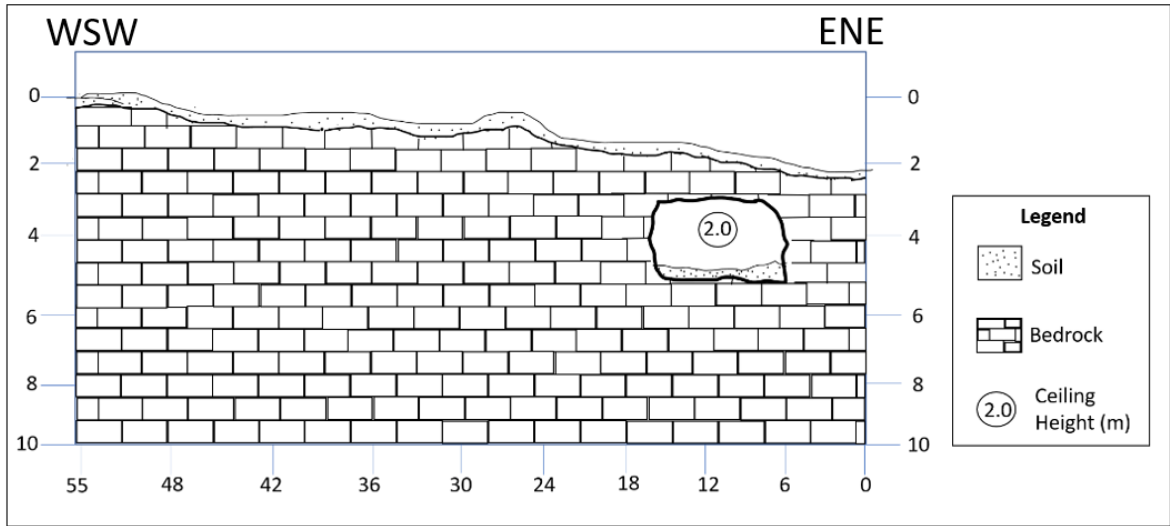


**Figure 39:** Cross sections for Brokeback Cave Line 1 (top) and Line 2 (bottom).

showed a zone of low resistivity at the 18-meter mark and below the estimated saturated-unsaturated contact boundary. A small opening in the ground surface near the location of this anomaly may be a conduit for soil piping proximal to the known cave passage. A potential high porosity zone was observed from the 30-36-meter mark (Figures 40 and 41A).

The second survey included a high resistivity anomaly across the known cave passage. This survey also showed a low resistivity anomaly at the 30-meter mark below the estimated saturated zone. Due to the lack of evidence at the surface, this low resistivity could be attributed to irregular dissolution or a partially collapsed sink, but verification of this feature was not possible. Below the known cave passage, a secondary area of high resistivity was noted at the 45-meter mark. The resistivity of this anomaly suggested the presence of open air at a depth greater than what was estimated for the floor of Brokeback Cave. Field observations noted that the cave floor sloped downward to the southwest in the area proximal to this anomaly within the known passage. This area has been interpreted as a potential unknown passage based on the high resistivity anomaly on the survey and field observations in the cave passage. The size of this anomaly may have also masked the known cave passage resulting in the distortion of the known passage (Figure 41B).

3-D surveys were conducted in the same general areas as the 2-D surveys in order to preserve continuity in subsurface interpretation. 3-D survey 1 at Brokeback Cave was

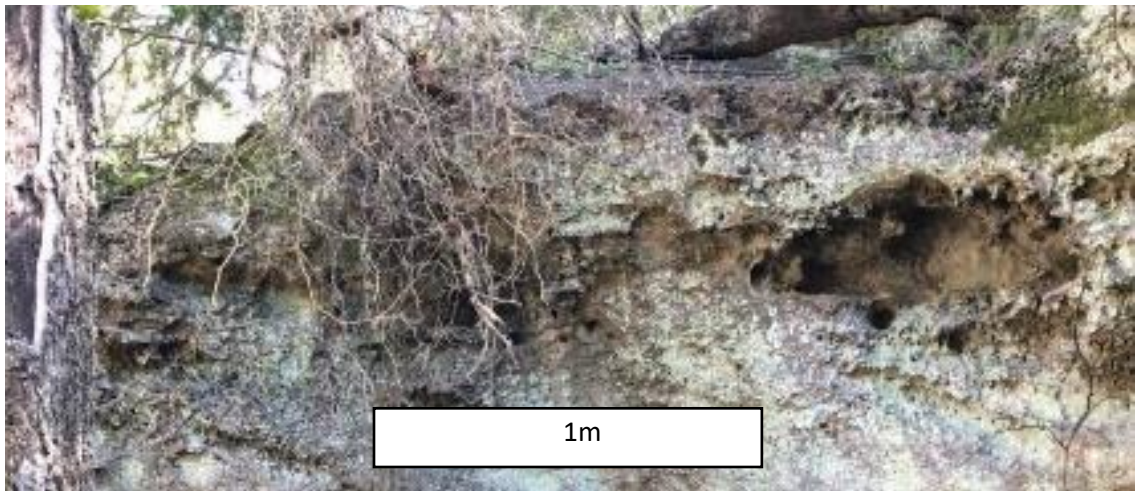
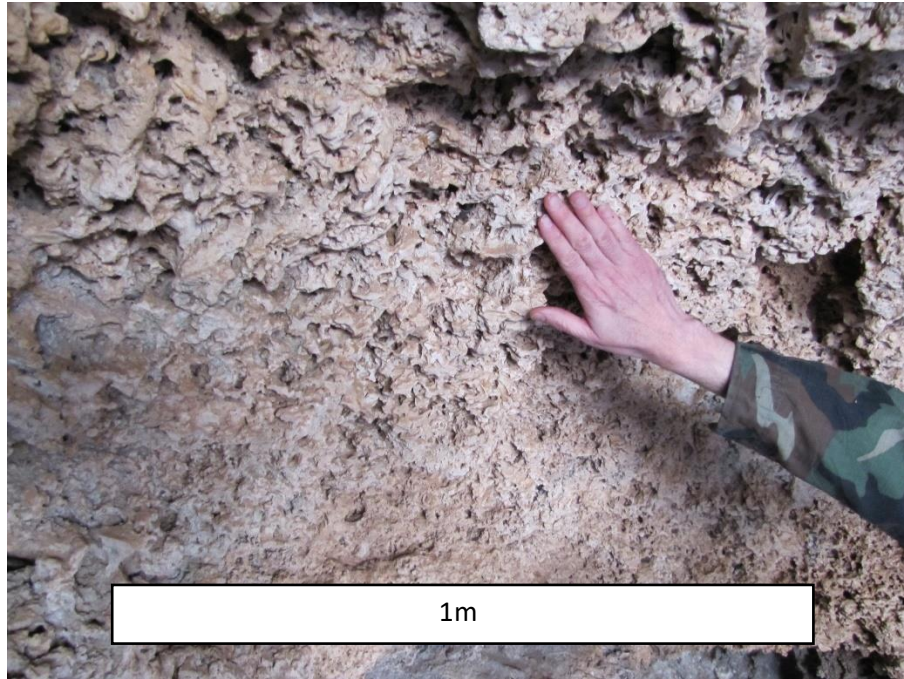


**Figure 40:** Example of highly porous zone located within Brokeback Cave (top) and a larger void located in outcrop near Brokeback Cave (bottom)

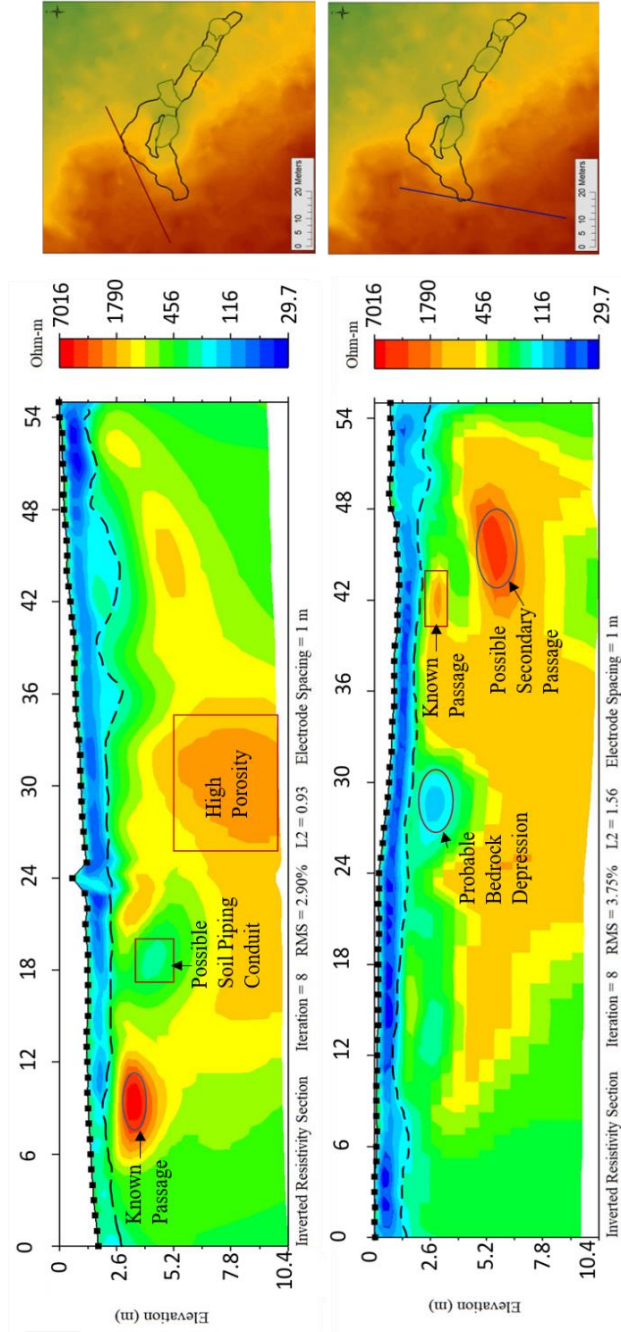


**Figure 41:** (A) Interpreted and corrected 2-D line 1 at Brokeback Cave conducted in the northern regions of the cave. (B) Interpreted and corrected 2-D line 2 for Brokeback Cave conducted in the western regions of the cave. Dashed lines in the figures above represent the separation between the saturated and unsaturated layer.

conducted perpendicular (south to north) to its 2-D counterpart due to constraints in soil cover and to encompass the same known passage. The full volume of the survey showed high resistivity anomalies near the 0-meter mark and the 26-meter mark (Figure 42A). The dynamic contours showed that the general morphology and size of the anomaly near the 0-meter mark coincided with the known cave passage, but the northern anomaly reported a lower resistivity value. This second anomaly was interpreted as a high porosity zone associated with the dissolution of depressions delineated by the LiDAR survey (Figure 42B). The 3-D contours showed the outline of the highest resistivity seen in the survey, and this shape is consistent with the shape, depth, and location of the known cave passage at Brokeback Cave (Figure 42C). Therefore, the zone associated with the 3-D contours was interpreted to be the known cave passage. Location of the survey in reference to the known cave passages can be seen in Figure 42D.

The second 3-D survey was conducted across the portion of 2-D line 2 that contained the known cave passage. The full volume model does not reveal any high resistivity anomalies (Figure 43A). However, the dynamic slices show a high resistivity anomaly near the 17-meter mark in the center of the survey (Figure 43B). The outline shown by the 3-D contours on this line represents the same general shape as the known cave passages (Figure 39 and 43C). Location of the survey in reference to the known cave passages can be seen in Figure 43D. Reduced depth in the 3-D survey did not allow for delineation of the probable secondary passage noted in the 2-D survey.



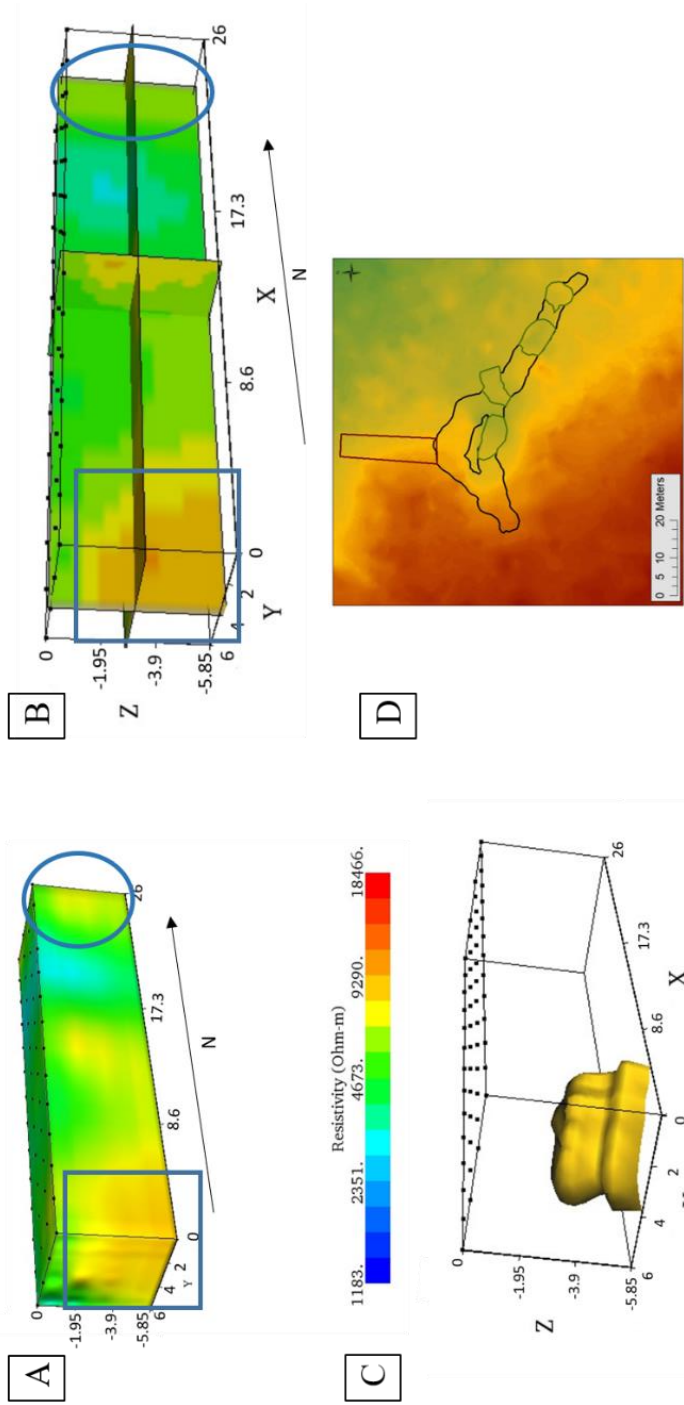


**Figure 42:** (A) Full volume for 3-D survey 1 for Brokeback Cave taken in the northern region of the cave. (B) Dynamic slices for survey 1 at Brokeback. (C) 3-D contours for survey 1 at Brokeback. (D) Location of 3-D survey 1 in relation to Brokeback Cave.



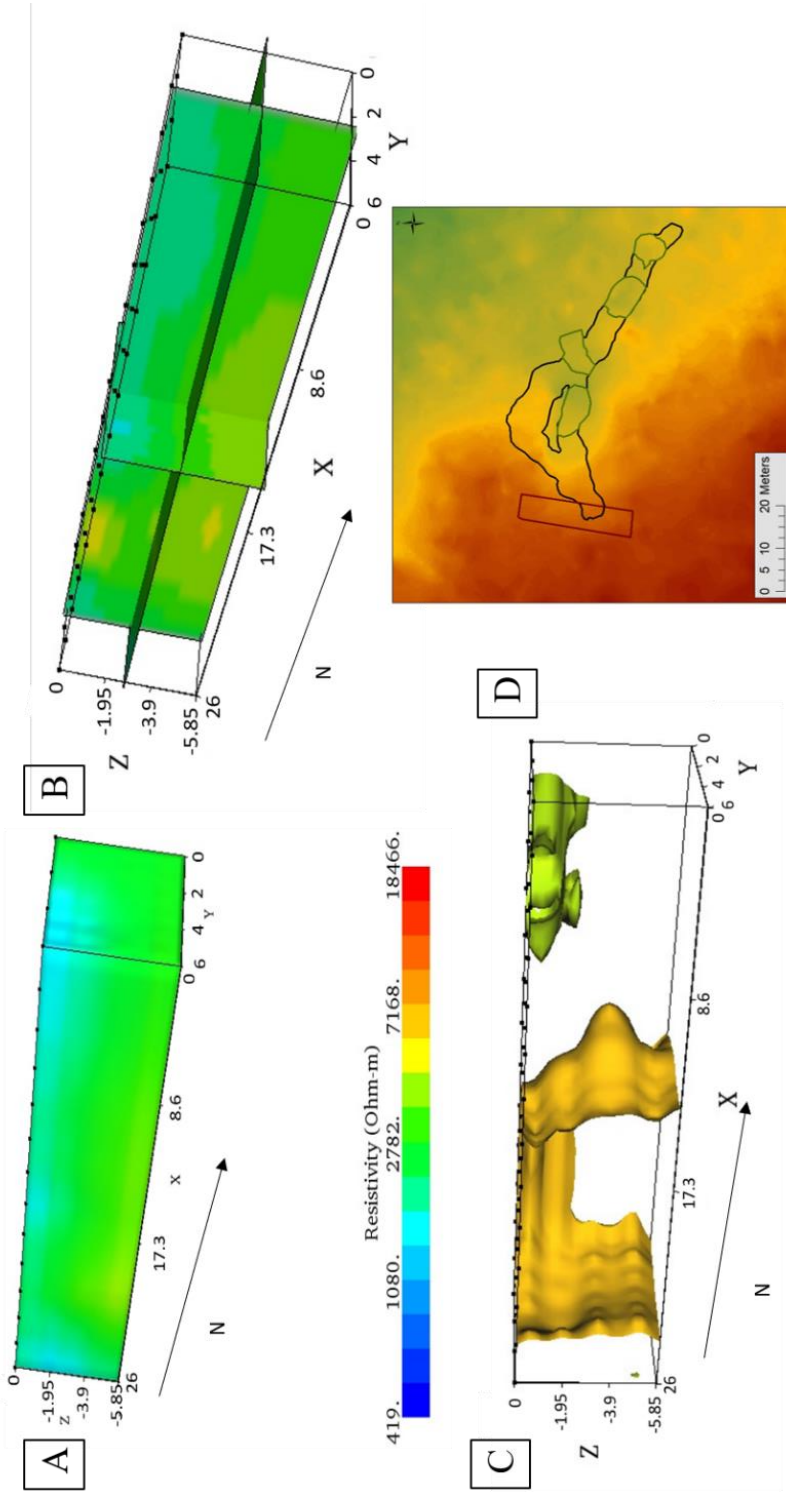


**Figure 43:** (A) Full volume for 3-D survey 2 at Brokeback Cave conducted to the west of the cave. (B) Dynamic contours for 3-D survey 2 at Brokeback Cave. (C) 3-D contours for 3-D survey 2. (D) Location of 3-D survey 2 in relation to Brokeback Cave.

## **Fern Cave**

The LiDAR karst survey results provided information about 235 depressions in the area surrounding Fern Cave, after filtering mechanisms were applied (Table 1), this number was reduced to 171 potential karst depressions. Similar to Brokeback Cave, Fern Cave is located in an area of moderate karst density though few features were observed during field operations. The cave map suggested that Fern Cave may have an infilled passage continuing to the northeast from the known extent of the cave (Figure 44 and 45). 2-D survey lines were completed to the northeast, southeast, and southwest of Fern Cave. This cave contains cultural remains and has been gated to preserve important archeological evidence. The iron gate could mask smaller anomalies in the resistivity data, so survey lines were kept at least five meters away from this gate during data collection. Cross-sections were estimated along survey lines intersecting probable passages (Figure 46).

2-D line 1 survey at Fern Cave was completed northeast of the known extent of the cave. A small zone of low resistivity was located at the 16-meter mark; this feature was approximately the same size and shape as similar structures at Brokeback Cave and was interpreted to be a suffosion feature related to soil piping (Figure 41A and 47). A high resistivity anomaly was located between the 28-34-meter marks with similar morphology

and resistivity values seen in the known cave passages at Brokeback Cave (Figure 41A and 41B). The anomaly coincided with the location of the possible infilled passages. Due to the shape and location of this feature, this anomaly is most likely associated with the infilled passage suggested in the cave map (Figure 48A).

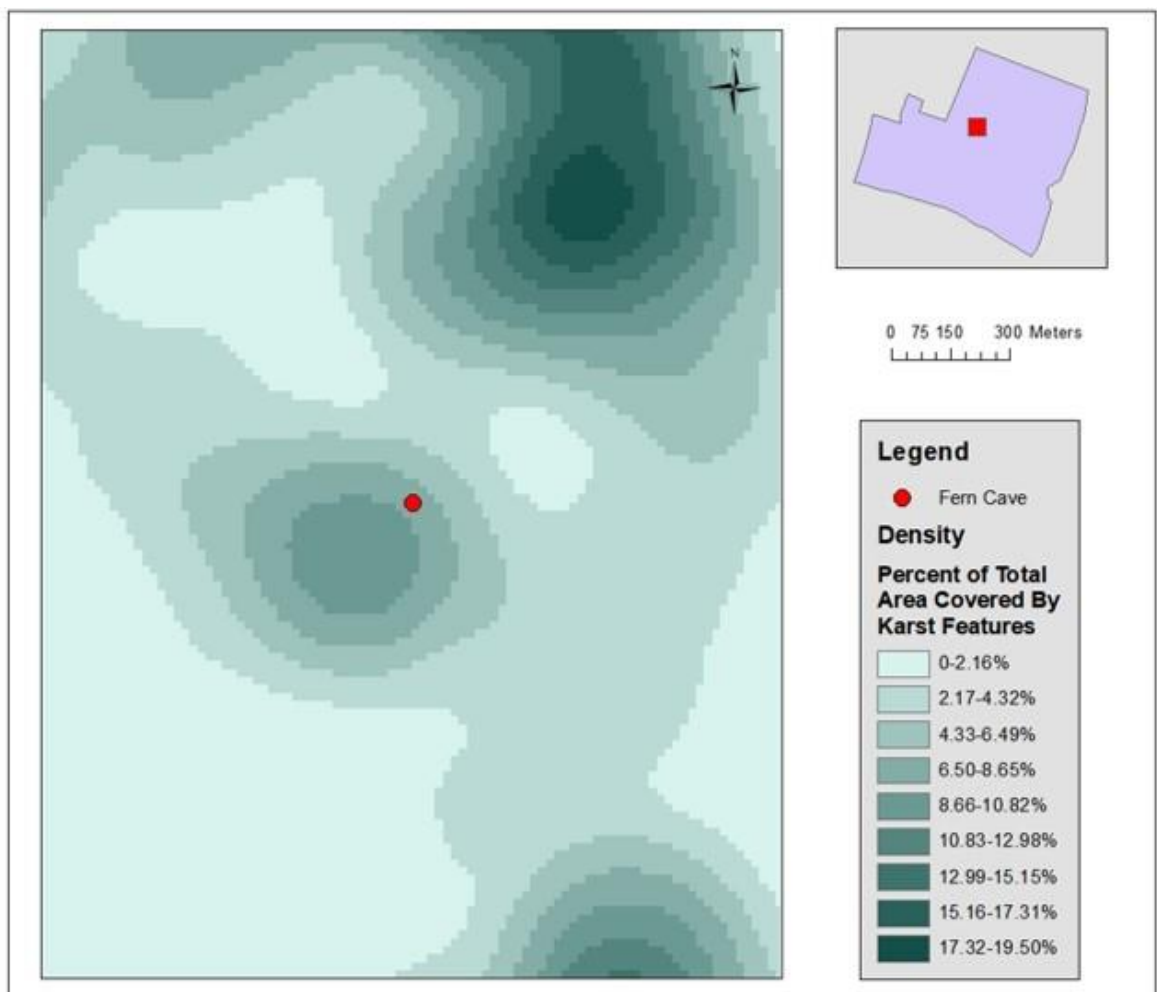


**Figure 44:** Density map of karst features surrounding Fern Cave ( modified from Quantum Spatial 2015).

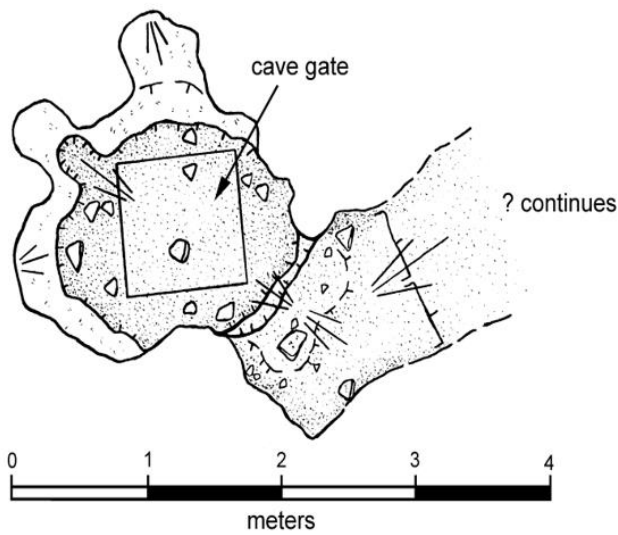


**FERN CAVE**  
**Fort Hood Military Reservation**  
**Coryell County, Texas**

Suuntos and Tape Survey  
26 July 2001  
J. Reddell, M. Reyes, M. Warton, B. Wetuski  
Drafted by M. Warton

Length: 5.60 m    Depth: 1.80 m

**PLAN**



**PROFILE**  
viewed at 0°

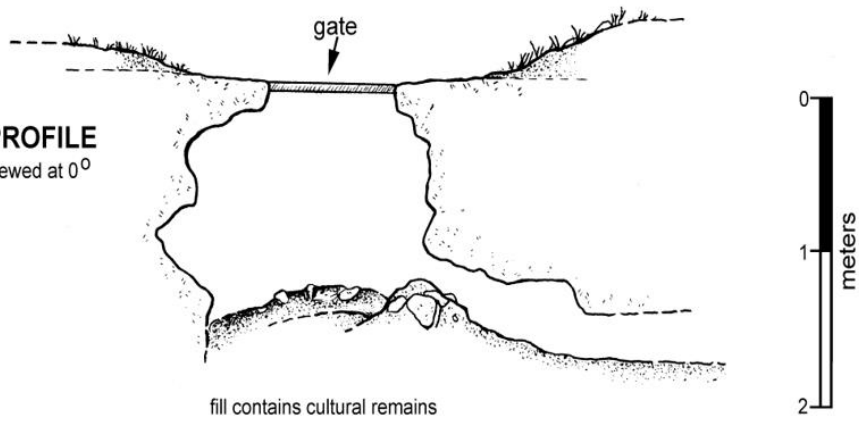


**Figure 45:** Cave map for Fern Cave (Texas Speleological Survey 2014).

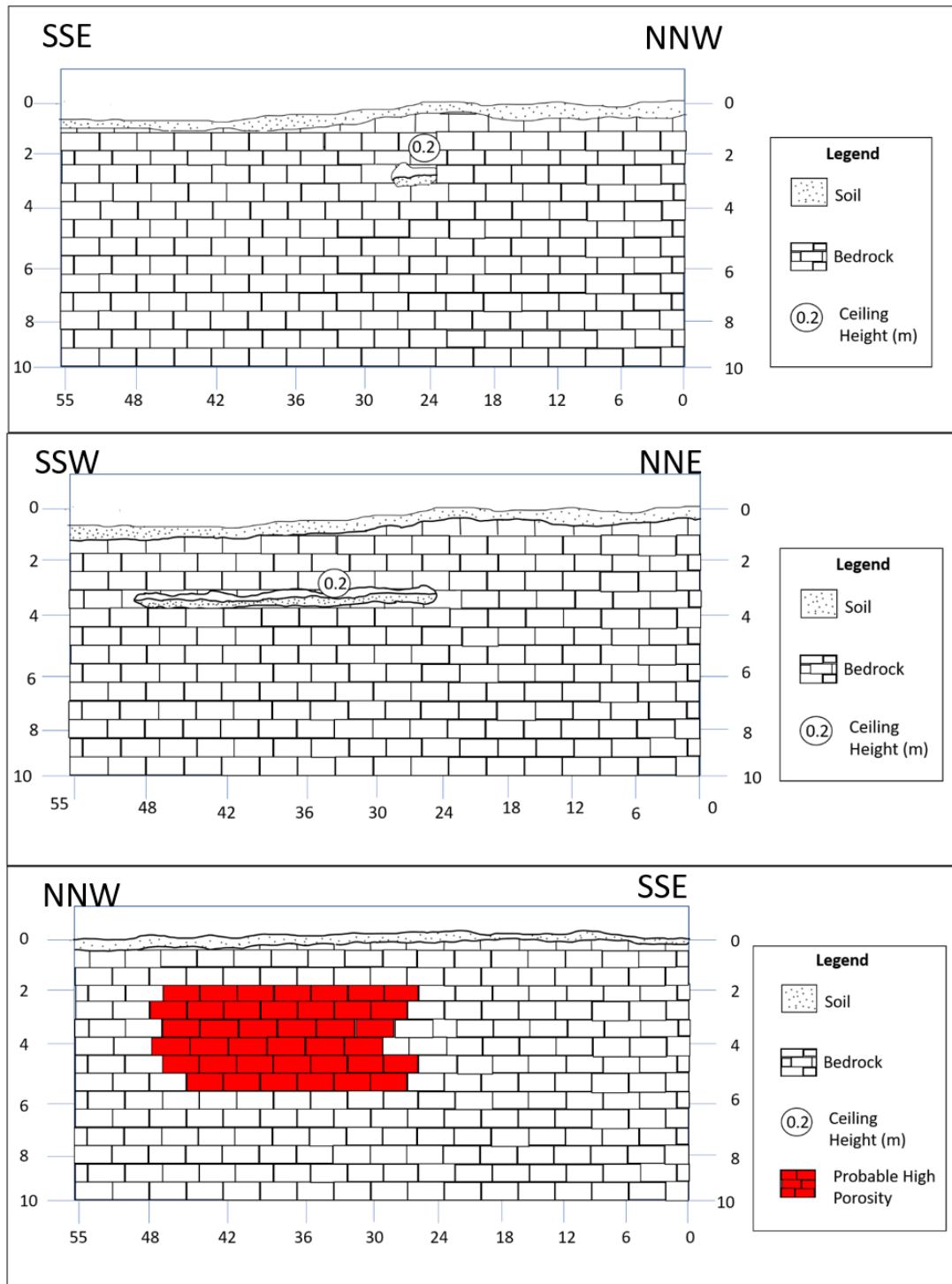


**Figure 46:** Cross-sections for Fern Cave line 1 (top), line 2 (middle), and line 3 (bottom).

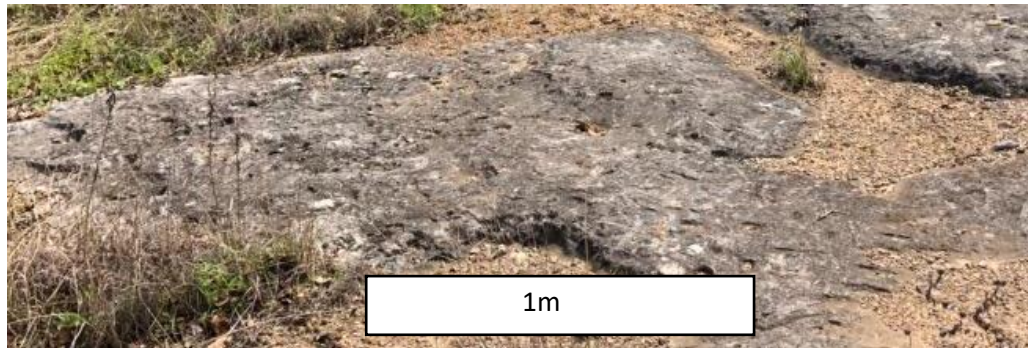


**Figure 47:** Example of soil piping conduit near survey line 1 (top) and vuggy porosity (bottom) near Fern Cave.



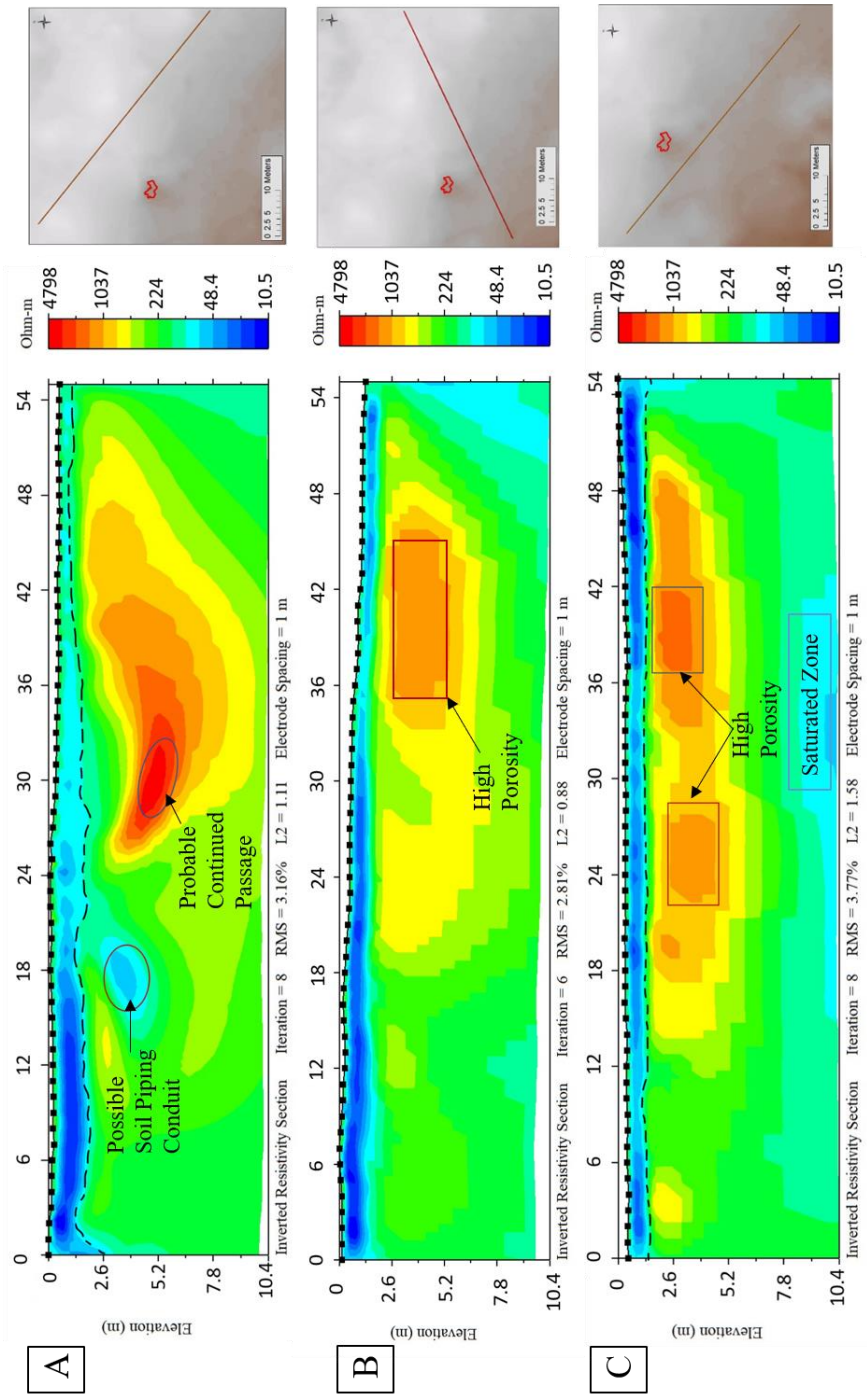


**Figure 48:** (A) 2-D Survey line 1 for Fern Cave. (B) 2-D survey line 2 for Fern Cave. (C) 2-D survey line 3 for Fern Cave. The dashed line in each section represents the boundary between the saturated and unsaturated zones.

The second 2-D survey line was conducted southeast of Fern Cave. Two zones of high porosity were discovered near the 24-meter mark and 36-48-meter marks. The anomaly near the 24-meter mark in Figure 48B highlighted a region of increased resistivity located parallel to the probable passage seen in survey line 1. The location and similar morphology to the possible cave passage seen in line 1 supports the determination that this could represent high porosity associated with the formation of the infilled passage. The second anomaly had higher resistivity values and was located parallel to the location of the mapped portion of Fern Cave, but the resistivity value was not high enough to denote open air. Due to the location and morphology of this anomaly, the area was interpreted to be a high porosity zone associated with the mapped passage of Fern Cave (Figure 48B). No cave features were identified along survey line 3. There was a large zone of higher resistivity in the center of the survey interpreted to be a high porosity zone, possibly similar to the larger voids seen in outcrop at Brokeback Cave (Figure 40), and low resistivity values in the deeper regions were interpreted to be a secondary zone of saturation (Figure 48C).

3-D survey 1 at Fern Cave was completed southwest of the cave feature and coincided with 2-D survey line 3 and was conducted to confirm the absence of cave features. The full volume of the survey showed a moderately high resistivity anomaly near the first electrode (Figure 49A). The dynamic contours show that the anomaly does not have high enough resistivity to denote a significant open area conduit in the subsurface (Figure 49B). The 3-D contours show the morphology of this high porosity



zone and the shape correlates with that seen in 2-D line 3 (Figure 49C). For this reason, the 3-D survey confirmed the lack of cave features in the survey area. Location of the survey in relation to Fern Cave can be seen in Figure 49D.

The second 3-D survey completed at Fern Cave was located to the northeast of the cave and correlated to the location of the probable soil piping location seen in 2-D line 1. The electrode spacing for this survey had to be reduced due to vegetation and soil constraints so the possible passage could not be delineated with this survey. The full volume showed a low resistivity anomaly along line 0 near the 13-meter mark (Figure 50A). The dynamic slices showed that resistivity decreased toward the 4-meter mark (Figure 50B) and the 3-D contours allowed for the analysis of the anomaly morphology. The low resistivity anomaly seen with the 3-D contours between the 4-8-meter marks is parallel to the potential soil piping feature identified in the field and may show a link between this feature and the low resistivity anomaly in 2-D survey line 1 (Figure 47 and 50C). The sloping of this anomaly into the subsurface coincides with the estimated depth of the anomaly in 2-D and supports the conclusion that there could be soil piping in the area. Location of the survey in relation to Fern Cave can be seen in Figure 48D. A 3-D survey was not completed on the southeast side of the cave due to vegetation and soil constraints.

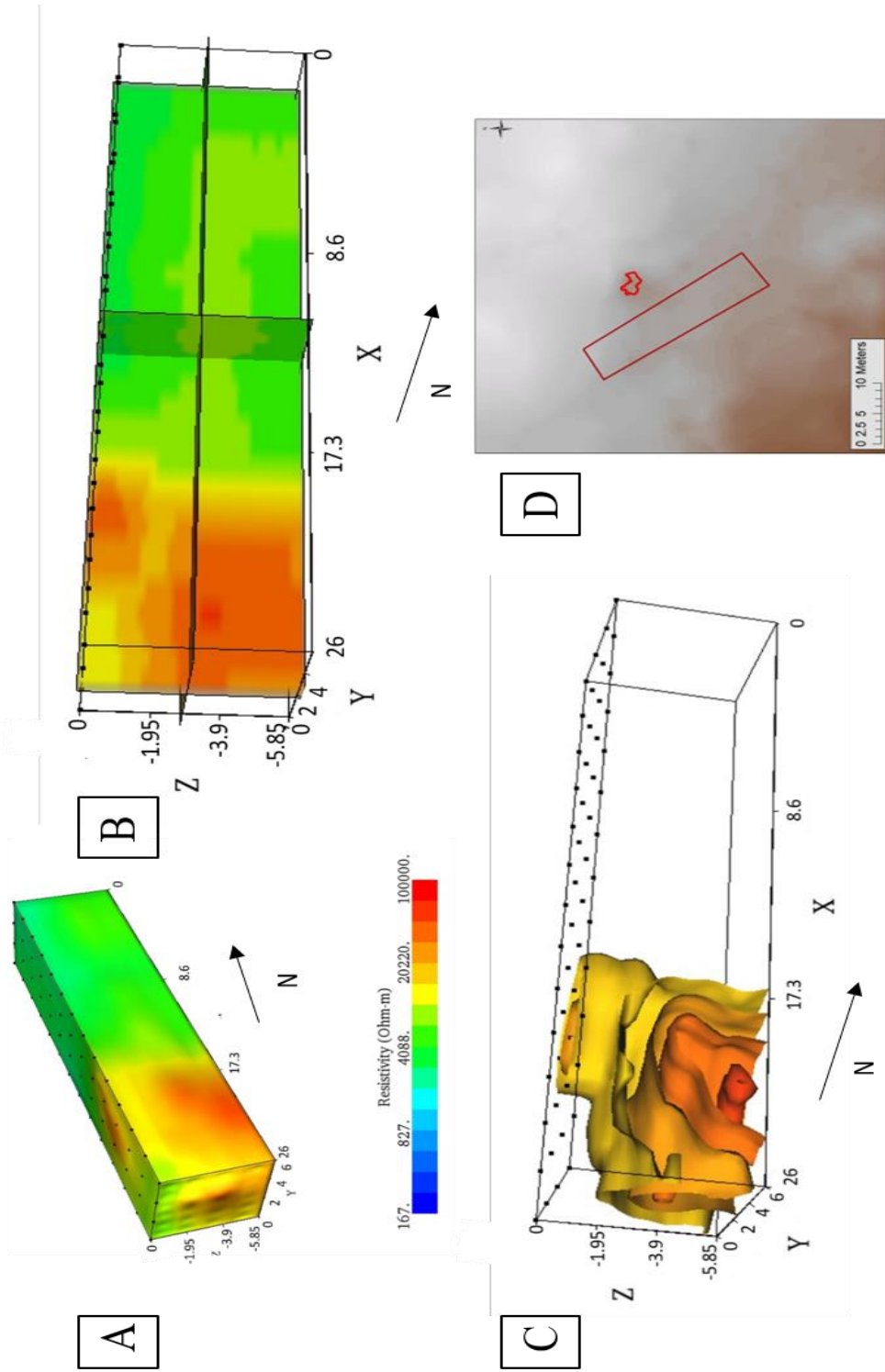


**Figure 49:** (A) Full volume for Fern Cave 3-D survey 1. (B) Dynamic contours for 3-D survey 1. (C) 3-D contours for 3-D survey 1. (D) Location of survey 1 for Fern Cave.

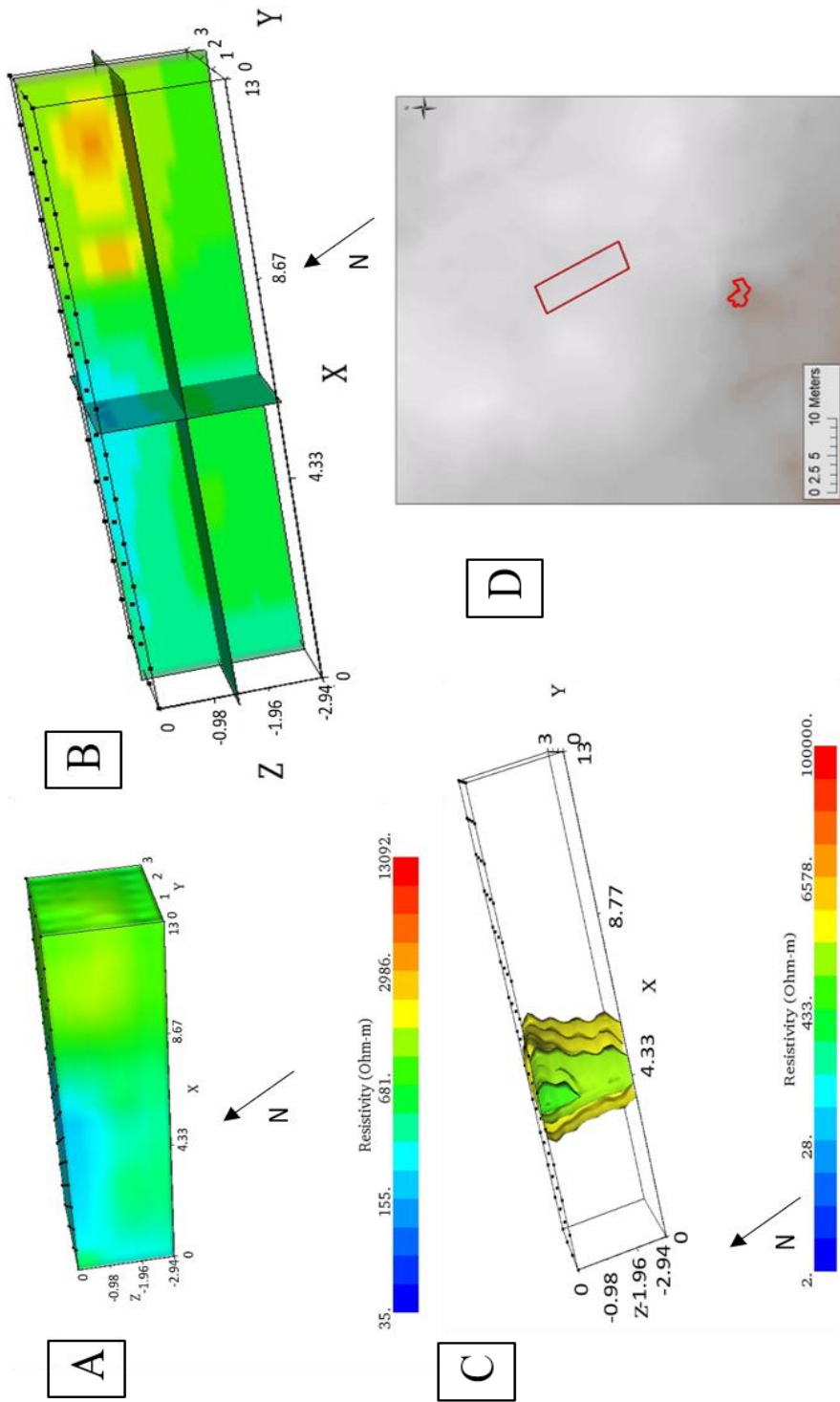


**Figure 50:** Due to constraints caused by vegetation, electrode spacing was reduced to 1 meter. (A) Full volume for Fern Cave 3-D survey line 2. (B) Dynamic contours for 3-D survey line 2. (C) 3-D contours for 3-D survey line 2. (D) Location of 3-D survey 2 in relation to Fern Cave.

## LIMITATIONS

LiDAR used in this study was collected in 2015 by flying an aircraft in a grid pattern across the entirety of Fort Hood Military Installation. Due to military land use and maintenance in the Shell Mountain Province, the ground surface is a continually evolving landscape used to support military training activities. This can include clear cutting of vegetation, prescribed burns, mulching, and large vehicle traverses near karst features. Continuous modifications to the training areas can lead to inconsistencies associated with field observations and LiDAR interpreted surfaces.

The SuperSting system for these surveys relied on the presence of adequate soil cover due to restrictions in bedrock drilling. Generally, this is the depth of about 2/3 of the electrode stake (20 centimeters). Many of the known cave features were characterized by extensive exposures of bedrock and lacked adequate soil cover. The Natural Resources Management Branch would not permit drilling into exposed rock surfaces which led to high contact resistance at the selected survey sites. For these reasons, survey locations were limited to those areas with adequate soil cover. At Brokeback and Fern caves, survey lines were placed in areas where conditions were optimal for electrode coupling, ultimately reducing the number of surveys and potential data collection. This may increase bias in the data as all areas surrounding the known cave features were not able to be explored using this electrical resistivity methodology.

Dense vegetation was located in proximity to cave features, and surveys completed near these vegetation stands have reported increased error within datasets. Vegetation could not be removed, and surveys were limited to areas that contained minimal plant cover, which reduced the number of survey lines that could be completed at each site. Lastly, drilling and digging around the cave sites was prohibited, and verification of subsurface anomalies was restricted.

## CONCLUSIONS

Exposed karst features are prevalent in the western training areas of Fort Hood. The LiDAR analyses completed during this survey showed that surface karst features are more prevalent than previously known, and sinks are located within the general proximity of known cave features. Electrical resistivity proved to be useful for determining the location and morphology of subsurface karst features. The identification of these features is vital to predicting areas that may pose a danger to military training personnel. Knowledge of the geologic setting, hydrologic environment, and known features in the area was necessary to accurately determine the nature of subsurface karst features.

The LiDAR analyses determined the potential locations for electrical surveys, provided accurate elevation data and aided in the geolocation of caves maps. 2-D direct current surveys were completed longer, linear surface areas and were useful in determining the location of subsurface karst features. The survey parameters allowed for the delineation of known passages at Brokeback Cave, and probable new passages in the areas surrounding both caves. 3-D surveys were able to establish the outline of the cave passages delineated in the 2-D surveys. The known morphology of the passages at Brokeback Cave were imaged successfully and at the appropriate depth, but the unknown features surrounding Fern Cave were harder to distinguish due to the reduced depth in the

3-D surveys. This reduced depth precludes the probability of discovering unknown features if used independently.

Anthropogenic alterations in the training areas may have created bias in assessing exposed karst features due to the covering of cave openings and sinks. The lack of adequate soil cover and dense vegetation near the cave locations prevented complete surveying of known karst features. The volume of karst features present throughout the entirety of Fort Hood supports the conclusion that additional surveys should be completed with the SuperSting system where adequate soil is present, and other electrical resistivity or geophysical methods should be employed in areas where soil is not sufficient. The non-invasive nature of electrical resistivity surveys is crucial to the management of karst geohazards in areas of high anthropogenic activity. The high-resolution resistivity data, while useful, must be associated with other geologic monitoring techniques in order to accurately assess karst features in this area.

## **FUTURE WORK**

Additional survey lines should be completed in the vicinity of Brokeback Cave and Fern Cave that were unavailable due to soil restrictions and inaccessible cave locations. These could be completed using the Geometrics OhmMapper or a similar device that is not limited by the lack of soil or presence of dense vegetation. Other geophysical methods should also be implemented in the vicinity of these caves to further characterize the presence of subsurface voids, including ground penetrating radar and gravity measurements. These different techniques could be applied to other training areas on Fort Hood and regions that show high karst density but no known karst manifestations. Lastly, results from this study could be used to create a karst geohazard map needed to ensure the safety and integrity of military personnel, equipment, environmentally sensitive habitats.



## REFERENCES

- Adkins, W.S., Arick, M.B., 1930, Geology of Bell County, Texas: The University of Texas Bulletin, No. 3016, Bureau of Economic Geology, pgs. 1-92.
- Advanced Geosciences (AGI), 2005, The SuperSting™ with Swift™ automatic resistivity and IP system Instruction Manual: Advanced Geosciences Inc, Austin, Texas.
- Amsbury, D.L., T.A. Jr. Bay, and F.E. Lozo, 1984, A Field Guide to Lower Cretaceous Carbonate Strata in the Moffatt Mound Area near Lake Belton, Bell County, Texas. Guidebook for SEPM Field Trip NO. 3. San Antonio: Gulf Coast Section of the Society of Economic Paleontologists and Mineralogists Foundation, pgs. 1-19.
- Anaya, R., 2004, Conceptual model for the Edwards-Trinity (Plateau) Aquifer System, Texas. Aquifers of the Edwards Plateau: Texas Water Development Board Report, 360, pgs. 21-62.
- Anaya, R., and Jones, I., 2009, Groundwater Availability Model for the Edwards-Trinity (Plateau) and Pecos Valley Aquifers of Texas: Report 373, Texas Water Development Board.
- Bryant, A. W., 2012, Geologic and Hydrogeologic Characterization of Groundwater Resources in the Fredericksburg Group, North Nolan Creek Province, Bell County, Texas: M.S. Thesis, Stephen F. Austin State University, Nacogdoches, Texas.
- Burger, H.R., Sheehan, A.F., and Jones, C.H., 2006, Introduction to Applied Geophysics: W.W. Norton & Company Inc.
- Chalokakis, K., Plagnes, V., Guerin, R., Valois, R., Bosch, F. P., 2011, Contribution of Geophysical Methods to Karst-System Exploration: An Overview: Hydrogeology Journal, v. 19, pgs. 1169-1180, doi: 10.1007/s10040-011-0746-x.

- Collins, E.W., 2005, Geologic Map of the West Half of the Taylor, Texas, 30 x 60 Minute Quadrangle: Central Texas Urban Corridor, Encompassing Round Rock, Georgetown, Salado, Briggs, Liberty Hill, and Leander, Miscellaneous Map No. 43: Bureau of Economic Geology, pg16.
- Ehrhart, J., 2016, Speleogenesis and Delineation of Megaporosity and Karst Geohazards Through Geologic Cave Mapping and LiDAR Analyses Associated with Infrastructure in Culberson County, Texas: M.S. Thesis, Stephen F. Austin State University, Nacogdoches, Texas.
- ESRI, 2019, ArcGIS Desktop 10 Resource Center: <https://support.esri.com/en/Products/Desktop/arcgis-desktop> (first accessed December 2019).
- Farooq, M., Park, S., Song, Y.S., Kim, J.H., Tariq, M., and Abraham, A.A., 2012, Subsurface Cavity Detection in a Karst Environment Using Electrical Resistivity (er): a Case Study From Younfweol-ri, South Korea: Earth Sciences Research Journal, vol 16, p 75-82.
- Faulkner, Melinda S., Stafford, K., and Bryant, A., 2013, Delineation and Classification of Karst Depressions Using LiDAR: Fort Hood Military Installation, Texas, 459-467. 10.5038/9780979542275.1157.
- Faulkner, M.G., 2016, An Investigation of Hydrogeologic, Stratigraphic, and Structural Controls on Acer Grandidentatum Communities in a Karst Landscape, Owl Mountain Province, Fort Hood Military Installation, Texas: Dissertation, Nacogdoches: Stephen F. Austin State University.
- Faulkner, Melinda S. and Bryant, Aaron W., 2018 Hypogene Karst of the Lampasas Cut Plain: Texas Speleological Society publication Hypogene Karst of Texas (accepted), Austin, Texas
- Fisher, W.L., and Rodda, P.U., 1969, Edwards Formation (Lower Cretaceous), Texas: Dolomitization in a Carbonate Platform System: American Association of Petroleum Geologists 53, no. 1: pgs 55-72.
- Hayden, T.J., Cornelius, J.D., Weinburg, H.J., Jette, L.J., and Melton, R.H., 2001, Endangered Species Management Plan for Fort Hood, Texas: FY01-05. Construction Engineering Research Laboratory. Army Corps of Engineers.

- Jones, I.C., 2003, Groundwater Availability Model: Northern Segment of the Edwards Aquifer, Texas. Report 358: Austin, Texas Water Development Board, pg. 75.
- Jones, I.C., 2006, Defining Groundwater Flow Characteristics in the Northern Segment of the Edwards Aquifer Based on Groundwater Chemistry: Austin Geological Society Bulletin, v. 2, pgs. 54-75.
- Kerr, R. S., 1977, Development and diagenesis of a Lower Cretaceous bank complex, Edwards Limestone, north central Texas, D. Bebout and L. Loucks, eds., Cretaceous carbonates of Texas and Mexico: Austin, Texas Bureau of Economic Geology, pgs. 216-233.
- Klimchouk, A.B., Tymokhina, E.I., Amelichey, G.N., 2012, Speleogenetic Effects of the Interaction Between Deeply Derived Fracture-Conduit Flow and Intrastratal Matrix Flow in Hypogenetic Karst Settings: International Journal of Speleology, v.41 (2). Pgs. 37-55. doi: <http://dx.doi.org/10.5038/1827-806X.41.2.4>
- Landers, A.N., 2016, Speleogenesis of Critchfield Bat Caves and Associated Hydrogeology of the Northern Edwards Aquifer, Williamson County, Texas: Master's Thesis, Nacogdoches: Stephen F. Austin State University.
- Loke, M.H., 1999, Electrical Imaging Surveys for Environmental and Engineering Studies: A Practical Guide to 2-D and 3-D Surveys.
- Majzoub, A., 2016, Characterization and Delineation of Karst Geohazards Along RM652 Using Electrical Resistivity Tomography, Culberson County, Texas: Master's Thesis, Nacogdoches: Stephen F. Austin State University.
- Mancini, E. A., and R. W. Scott, 2006, Sequence stratigraphy of Comanchean Cretaceous outcrop strata of northeast and south-central Texas: Implications for enhanced petroleum exploration: Gulf Coast Association of Geological Societies Transactions, v. 56, pg. 539-550.
- McCann, A.J., 2012, Surficial Fractures and Their Interferences on Fluid Movement in Hydrogeologic Reservoirs, Central Texas: M.S. Thesis, Stephen F. Austin State University, Nacogdoches, Texas, p. 1-234.
- Nelson, H.F., 1973, The Edwards Reef Complex and Associated Sedimentation. The Geological Society of America, Dallas: Bureau of Economic Geology, 1-35.

- Park, M.K., Park, S. Yi, M.J., Kim, C., Son, J.S., Kim, J.H., and Abraham, A.A., 2013, Application of Electrical Resistivity Tomography (ERT) Technique to Detect Underground Cavities in a Karst Area of South Korea: Environmental Earth Sciences, v.71, pg. 2797-2806.
- Pugsley, W.S., 2001, Imprint on the Land: Life Before Camp Hood, 1820-1942; Prewitt and Associates, Inc.
- Quantum Spatial, 2015, Field Survey Report of Photo ID Ground Control Points: Quantum Spatial Inc.
- Reddell, JR., Fant, J., Reyes, M., and Warton, M., Karst Research on Fort Hood, Bell and Coryell Counties, Texas. Unpublished Report, Fort Hood (TX): Fort Hood Natural Resources Management Branch
- Redhaouia B. & Ilondo B., Gabtni H., Khomsi S., Bédir, M., 2015. Electrical Resistivity Tomography (ERT) Applied to Karst Carbonate Aquifers: Case Study from Amdoun, Northwestern Tunisia. Pure and Applied Geophysics. 173. 10.1007/s00024-015-1173-z.
- Reece, C., 2018, Delineation of Karst Potential Using Lidar and GIS Analysis, Fort Hood Military Installation, Texas: M.S. Thesis, Stephen F. Austin State University, Nacogdoches, Texas.
- Rose, P.R., 1972. Edwards Group, Surface and Subsurface, Central Texas: Report of Investigations, no. 74, Bureau of Economic Geology, pg 198.
- Scott, R.W. and Kidson, E.J. 1977. Lower Cretaceous Depositional Systems, West Texas: pp. 169- 182, in Bebout, D.G. and Loucks, R.G. (Eds.), Cretaceous Carbonates of Texas & Mexico. University of Texas at Austin, Austin. pg 332..
- Texas Department of Transportation (TXDOT), 2019. Texas County Boundaries. Web. 2019-06-14. [https://services.arcgis.com/KTcxITD9dsQw4r7Z/arcgis/rest/services/Texas\\_County\\_Boundaries/FeatureServer](https://services.arcgis.com/KTcxITD9dsQw4r7Z/arcgis/rest/services/Texas_County_Boundaries/FeatureServer)
- Texas Parks and Wildlife Department (TPWD). Natural Regions: 2014-02-01. Web. 2020-03-23. Accessed through TNRIS, <https://data.tnr.is.org/collection/28c30f70-e4a8-4f69-9b40-b6ca8b2d32b7>
- Texas Speleological Survey (TSS) 2014, TSS Map CD: Map of Brokeback Cave and Fern Cave.

- Texas Water Science Center (USGS TWSC). Geologic Database of Texas, 2014-02-01. Web. 2020-03-30. Accessed through TNRIS  
[https://webservices.tnris.org/arcgis/services/Geologic\\_Database/GeologicDatabasesofTexas\\_250k/MapServer/WMSServer](https://webservices.tnris.org/arcgis/services/Geologic_Database/GeologicDatabasesofTexas_250k/MapServer/WMSServer)
- United States Department of Agriculture (USDA). Texas NAIP Imagery: 2018-12-31. Web. 2020-03-24. Accessed through TNRIS,  
[https://webservices.tnris.org/arcgis/services/NAIP/NAIP18\\_NC\\_CIR\\_60cm/ImageServer/WMSServer](https://webservices.tnris.org/arcgis/services/NAIP/NAIP18_NC_CIR_60cm/ImageServer/WMSServer).
- United States Climate Data, 2019, Climate Killeen Texas, Web. 2019-12-14.  
<https://www.usclimatedata.com/climate/killeen/texas/united-states/ustx0692>
- Veni, G., 1994, Hydrogeology and Evolution of Caves and Karst in the Southwestern Edwards Plateau, Texas: The Caves and Karst of Texas, National Speleological Society, Huntsville, Alabama. pg. 252.
- Walker, L.E., 1979, Occurrence, Availability, and Chemical Quality of Ground Water in the Edwards Plateau Region of Texas: Report 235, Texas Department of Water Resources, p 336.
- Youssef, A.M., El-Kaliouby H., and Zabramawi Y.A., 2012, Sinkhole Detection Using Electrical Resistivity Tomography in Saudi Arabia, Journal of Geophysics and Engineering, p 655-663. <https://doi.org/10.1088/1742-2132/9/6/655>.
- Zhou, W., Beck, B., and Adams, A., 2002, Effective Electrode Array in Mapping Karst Hazards in Electrical Resistivity Tomography: Environmental Geology, v.42, pg. 922-928.

**APPENDIX**  
**2-D AND 3-D SURVEY RESULTS**

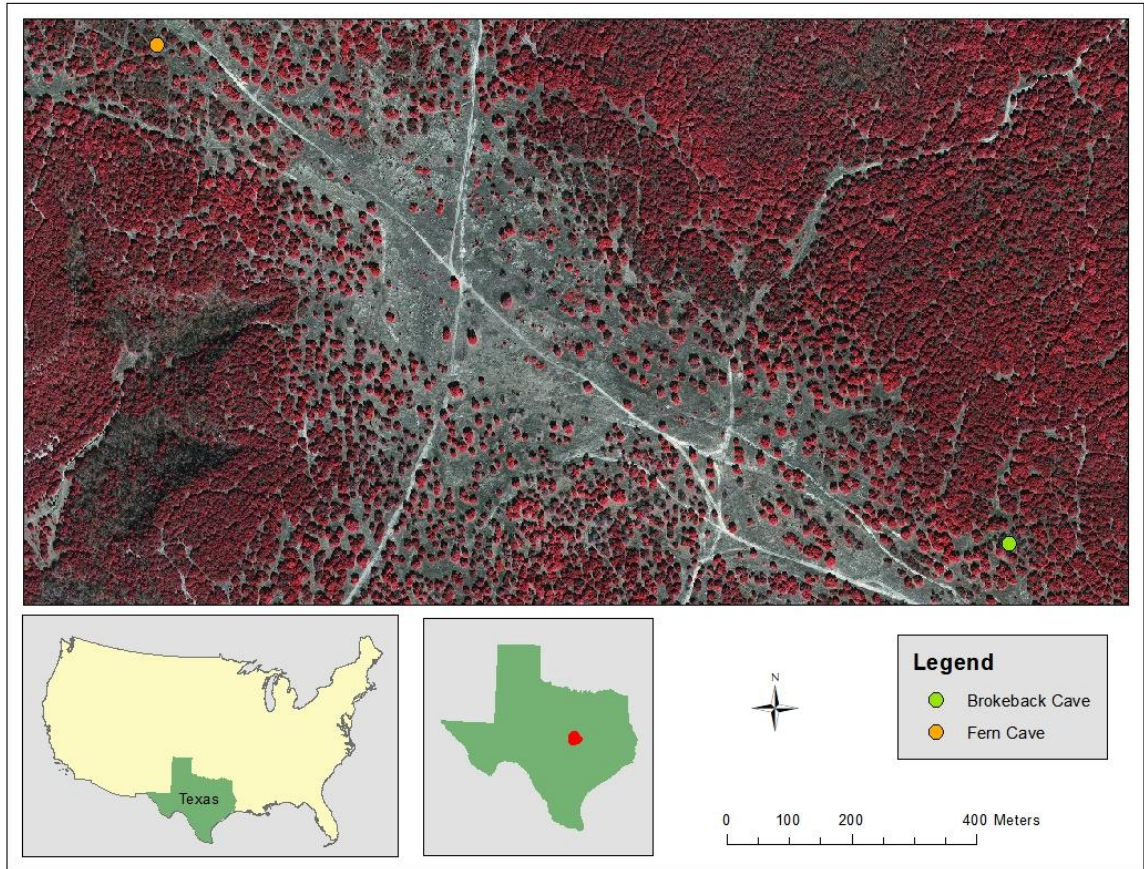
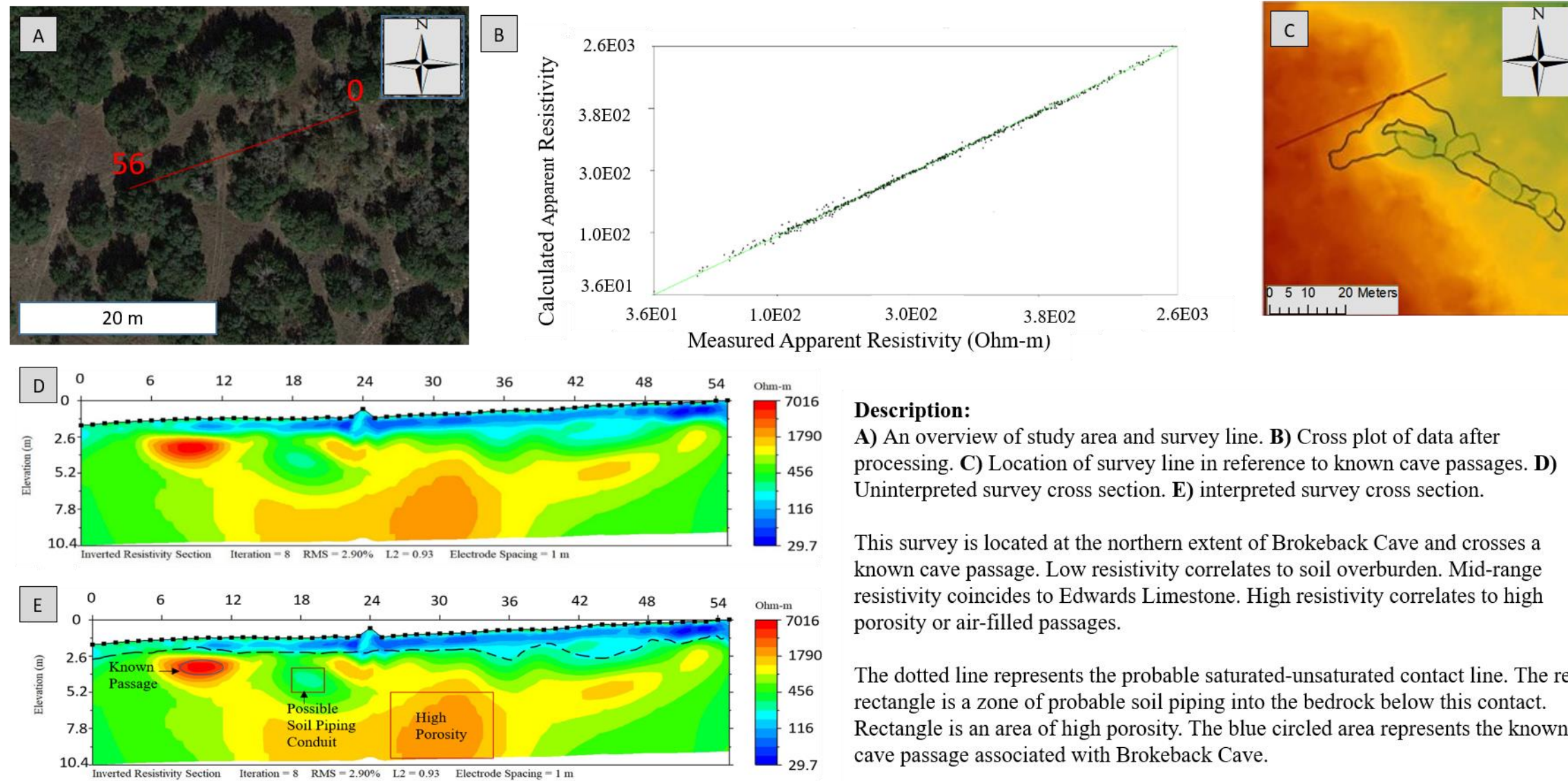


**Figure A1:** A general location map for the study area within Fort Hood and the state of Texas (modified from the United States Department of Agriculture 2018).





**Description:**

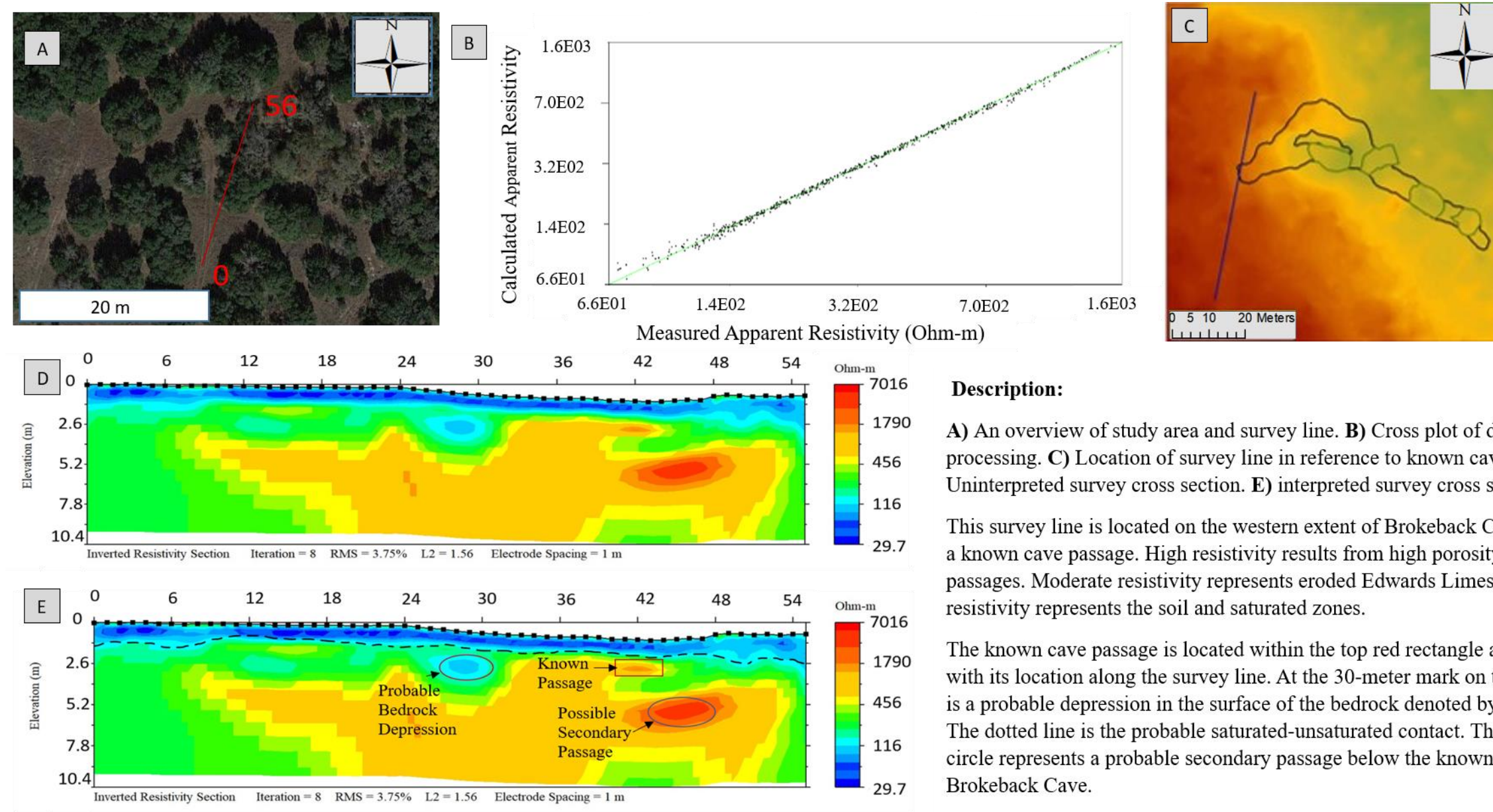
**A)** An overview of study area and survey line. **B)** Cross plot of data after processing. **C)** Location of survey line in reference to known cave passages. **D)** Uninterpreted survey cross section. **E)** interpreted survey cross section.

This survey is located at the northern extent of Brokeback Cave and crosses a known cave passage. Low resistivity correlates to soil overburden. Mid-range resistivity coincides to Edwards Limestone. High resistivity correlates to high porosity or air-filled passages.

The dotted line represents the probable saturated-unsaturated contact line. The red rectangle is a zone of probable soil piping into the bedrock below this contact. Rectangle is an area of high porosity. The blue circled area represents the known cave passage associated with Brokeback Cave.

**Figure A2:** Survey analysis for Brokeback Cave 2-D line 1. Maximum resistivity is 6184 Ohm-m and RMS of 2.90%. Maximum depth penetrated was 10.4 meters using 56 electrodes at 1 meter spacing.





**Description:**

**A)** An overview of study area and survey line. **B)** Cross plot of data after processing. **C)** Location of survey line in reference to known cave passages. **D)** Uninterpreted survey cross section. **E)** interpreted survey cross section.

This survey line is located on the western extent of Brokeback Cave and crosses a known cave passage. High resistivity results from high porosity or air-filled passages. Moderate resistivity represents eroded Edwards Limestone and low resistivity represents the soil and saturated zones.

The known cave passage is located within the top red rectangle and coincides with its location along the survey line. At the 30-meter mark on the survey there is a probable depression in the surface of the bedrock denoted by the red circle. The dotted line is the probable saturated-unsaturated contact. The bottom blue circle represents a probable secondary passage below the known extent of Brokeback Cave.

**Figure A3:** Survey analysis for Brokeback Cave 2-D line 2. Maximum resistivity is 2448 ohm-meters and RMS is 3.75%. Maximum depth penetrated was 10.4 meters using 56 electrodes at 1 meter spacing.

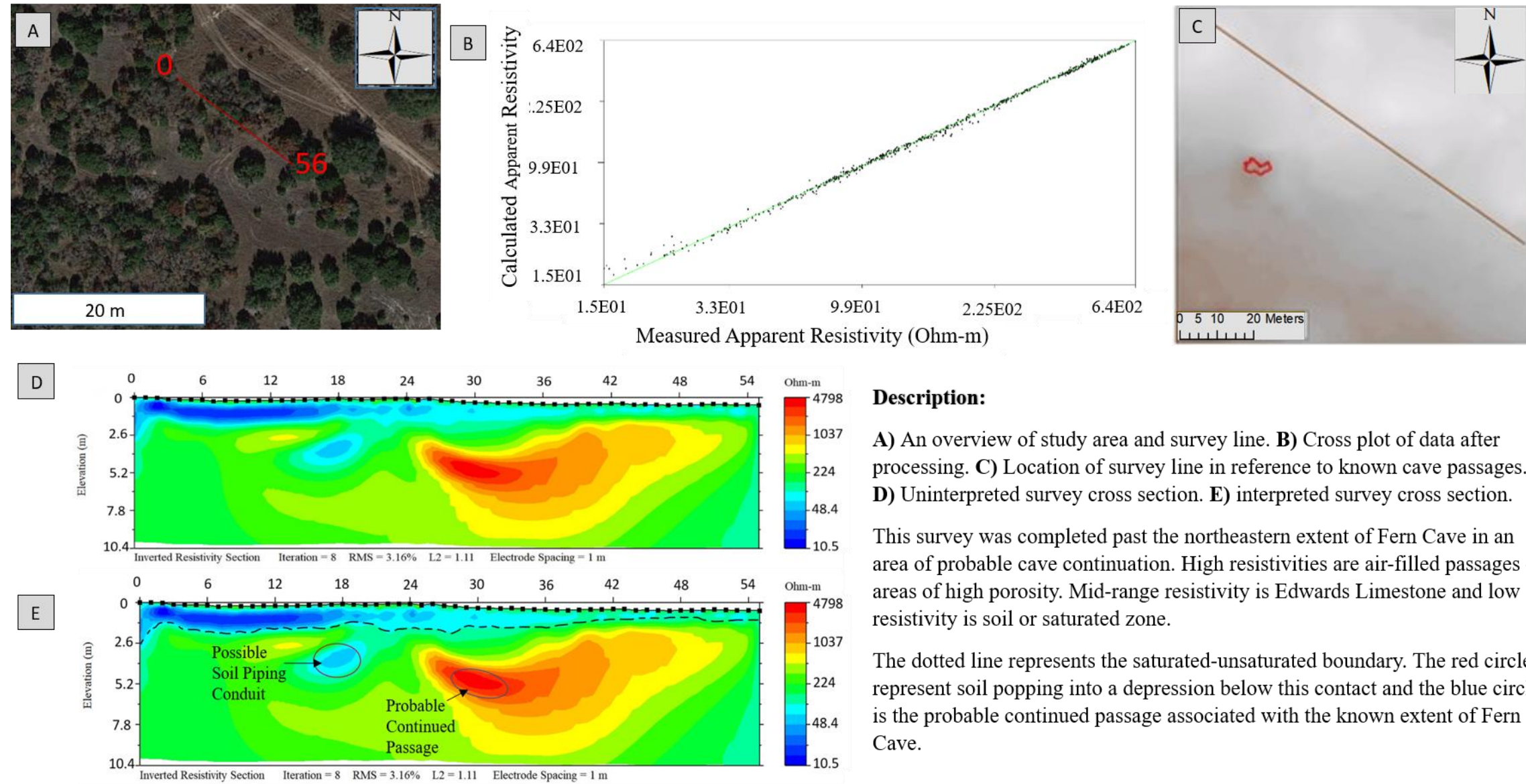


**Figure A4:** Survey analysis for Fern Cave 2-D line 1. Maximum resistivity values are 3496 ohm-meters and RMS is 3.16%. The maximum depth achieved in this survey was 10.4 meters using 56 electrodes at 1 meter spacing.



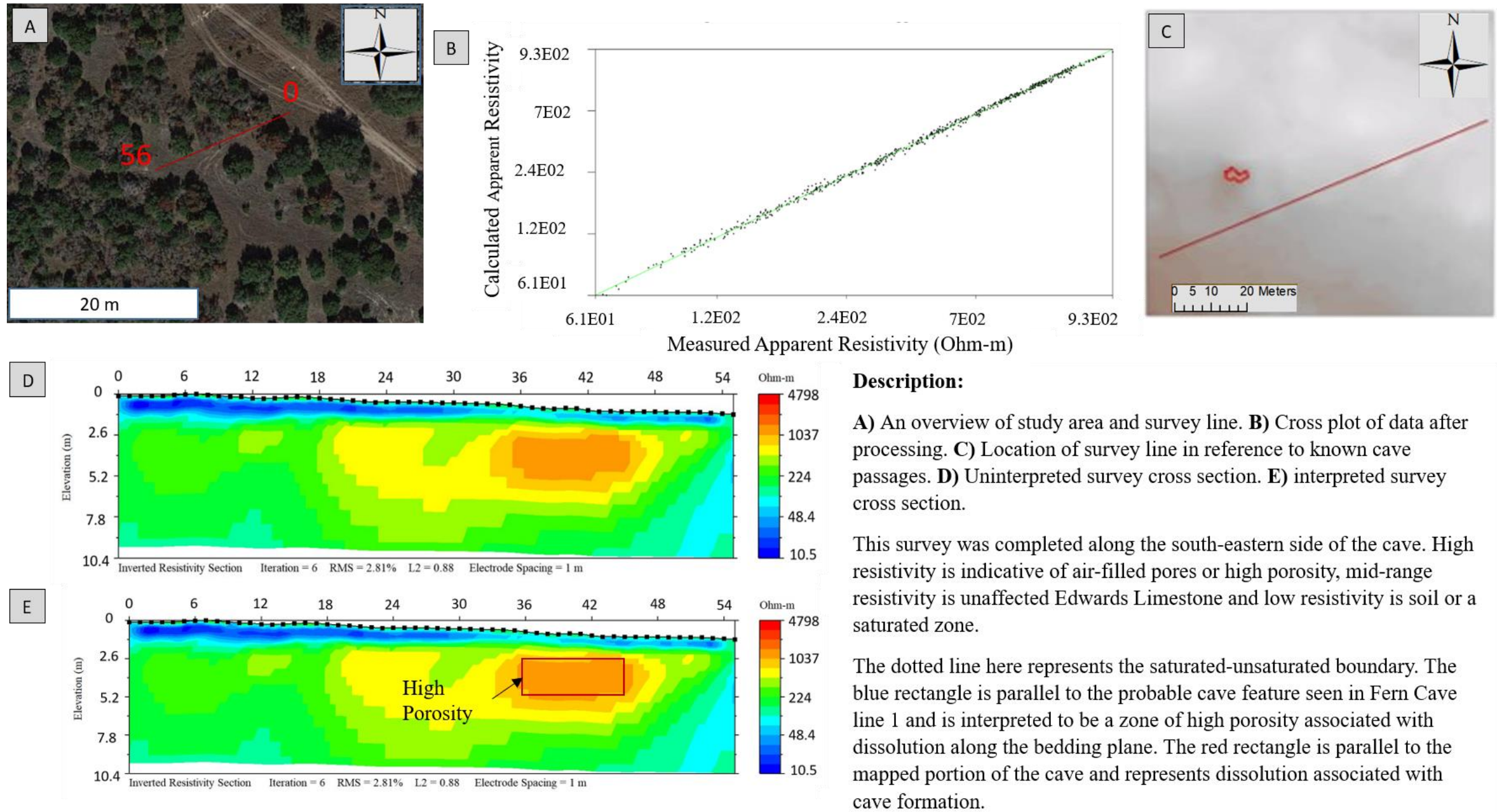
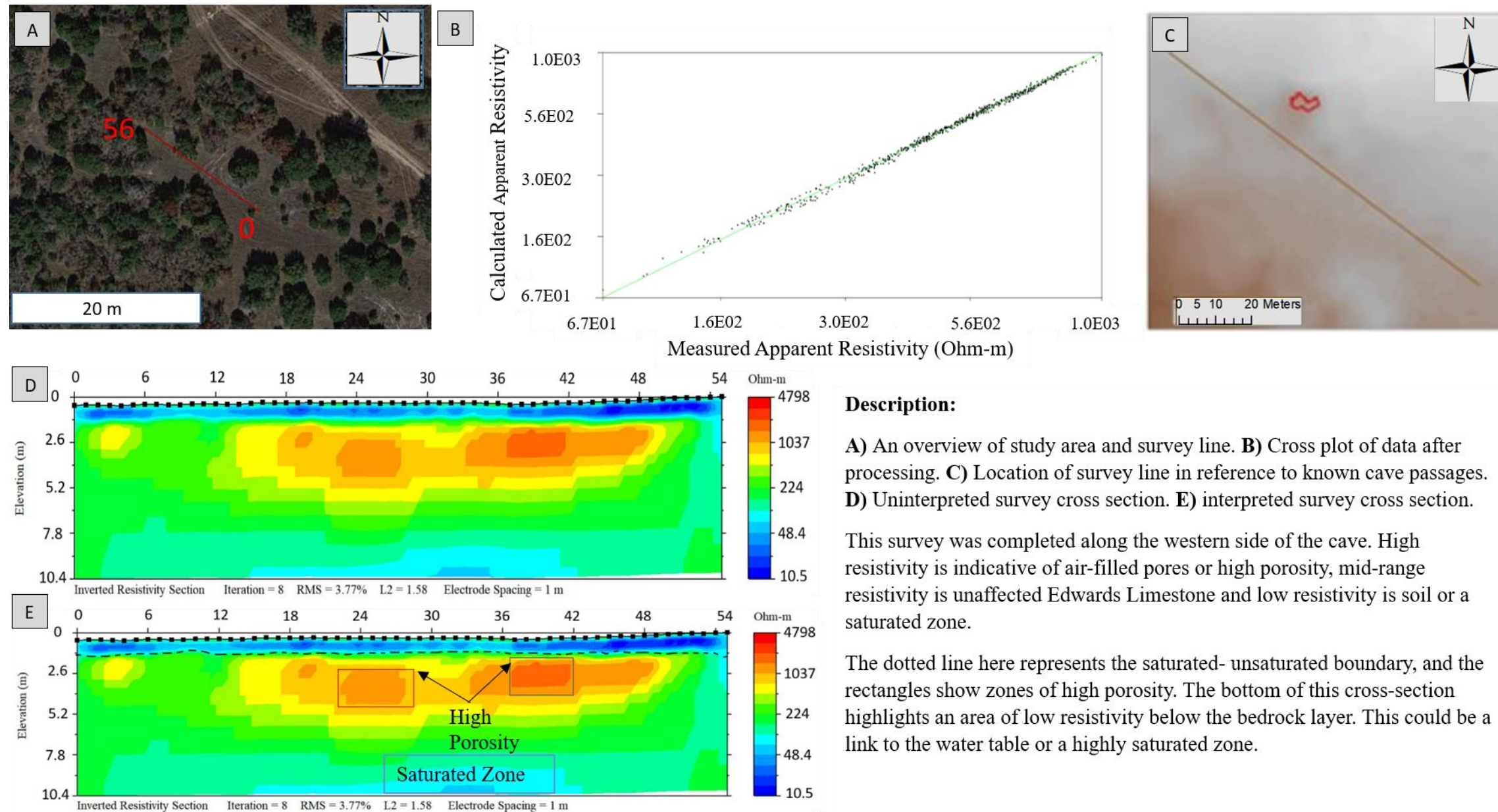


**Figure A5:** Survey analysis for Fern Cave 2-D line 2. Maximum resistivity values are 2420 ohm-meters and RMS is 2.81%. The maximum depth achieved in this survey was 10.4 meters using 56 electrodes at 1 meter spacing.



**Description:**

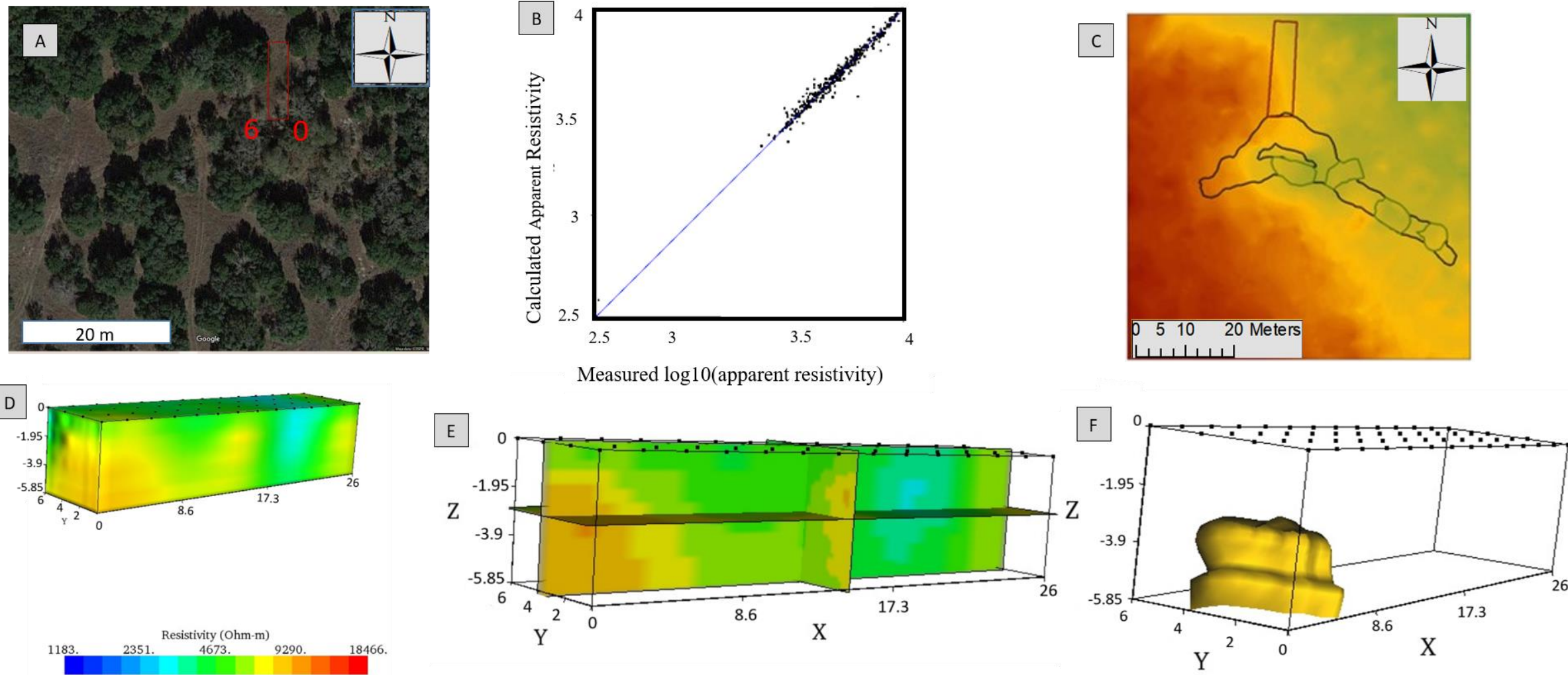
**A)** An overview of study area and survey line. **B)** Cross plot of data after processing. **C)** Location of survey line in reference to known cave passages. **D)** Uninterpreted survey cross section. **E)** interpreted survey cross section.

This survey was completed along the western side of the cave. High resistivity is indicative of air-filled pores or high porosity, mid-range resistivity is unaffected Edwards Limestone and low resistivity is soil or a saturated zone.

The dotted line here represents the saturated- unsaturated boundary, and the rectangles show zones of high porosity. The bottom of this cross-section highlights an area of low resistivity below the bedrock layer. This could be a link to the water table or a highly saturated zone.

**Figure A6:** Survey analysis for Fern Cave 2-D line 3. Maximum resistivity values are 4285 ohm-meters and RMS is 3.77%. The maximum depth achieved in this survey was 10.4 meters using 56 electrodes at 1 meter spacing.





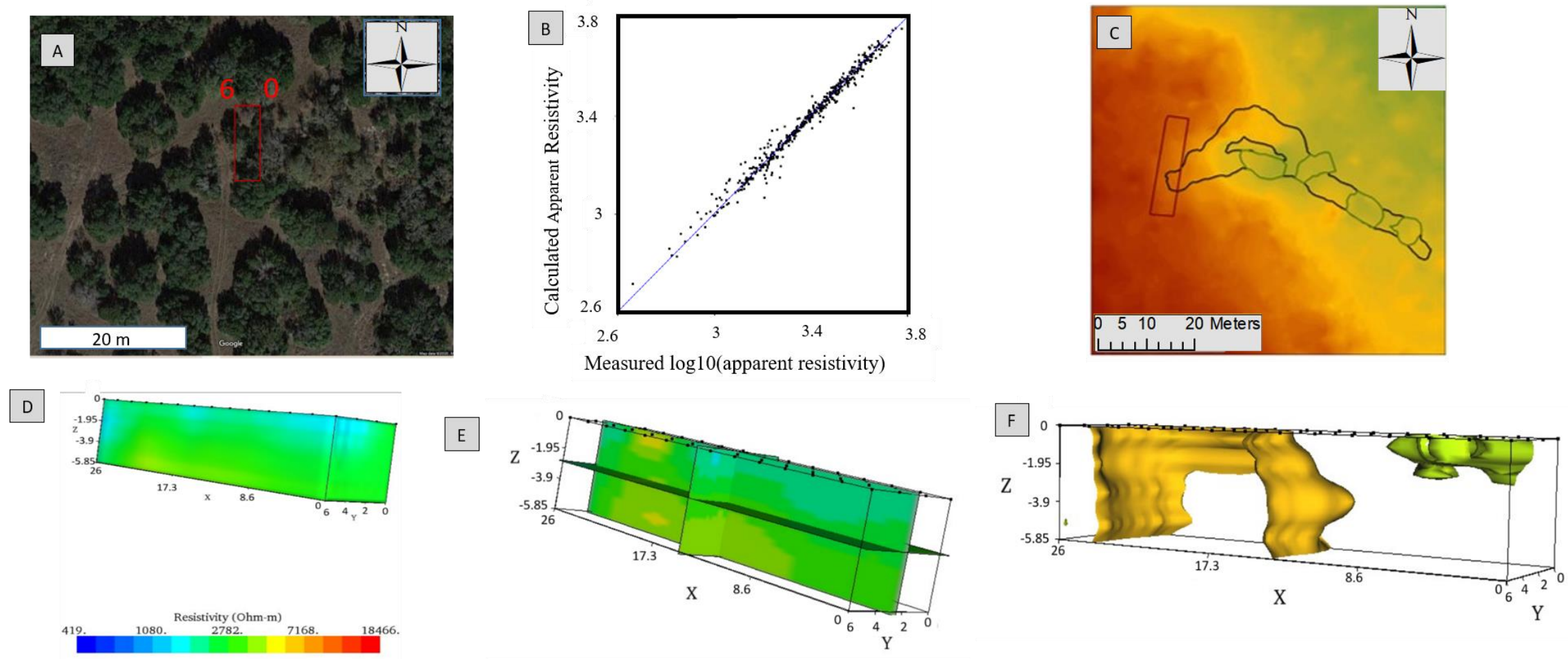
**Description:**

**A)** An overview of study area and survey line. **B)** Cross plot of data after processing. **C)** Location of survey in reference to known cave passages. **D)** Full volume of 3-D survey **E)** Dynamic contours of survey. **F)** 3-D contours of survey.

This survey was completed to encompass the northern extent of Brokeback Cave and was run perpendicular to Brokeback line 1 2-D as well as the cave itself. High resistivity here represents zones of higher porosity or air-filled passages. Low and intermediate resistivity are zones of saturation/soil and natural limestone, respectively.

The 3-D volume image shows two areas of interest shown in the forward right corner and back right corner. The dynamic slice shows the extent in the x- and y-directions. The 3-D contour model shows the morphology of the front anomaly. This coincides to the location, depth, and shape of the known cave passage in this area.

**Figure A7:** Survey analysis for Brokeback Cave 3-D survey 1. Maximum resistivity values are 14598 ohm-meters and RMS is 4.9%. The maximum depth achieved in this survey was 5.85 meters using 56 electrodes at 2 meters spacing in a 4-by-14 grid with cables in the x-direction.



**Description:**

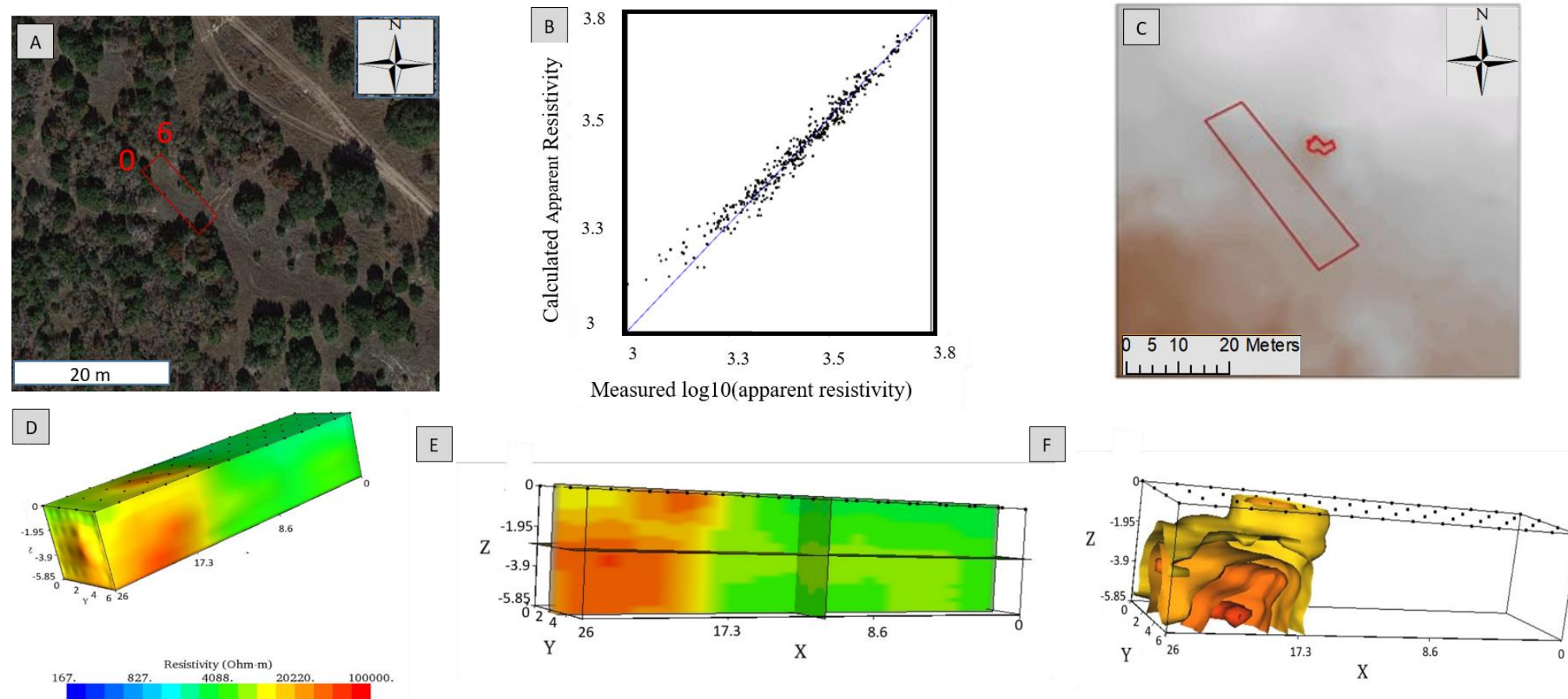
**A)** An overview of study area and survey line. **B)** Cross plot of data after processing. **C)** Location of survey in reference to known cave passages. **D)** Full volume of 3-D survey **E)** Dynamic contours of survey. **F)** 3-D contours of survey.

This survey was completed to encompass the western extent of Brokeback Cave and was run parallel to a portion Brokeback line 2 2-D as well as the cave itself. High resistivity here represents zones of higher porosity or air-filled passages. Low and intermediate resistivity are zones of saturation/soil and natural limestone respectively.

The 3-D volume image shows two areas of interest shown in the back right corner near the 26 meter mark. The dynamic slice shows the extent in the x- and y-directions. The 3-D contour model shows the morphology of the anomaly. This coincides to the location, depth, and shape of the known cave passage in this area.

**Figure A8:** Survey analysis for Brokeback Cave 3-D survey 2. Maximum resistivity values are 43194 ohm-meters and RMS is 4.8%. The maximum depth achieved in this survey was 5.85 meters using 56 electrodes at 2 meters spacing in a 4-by-14 grid with cables in the x-directions.





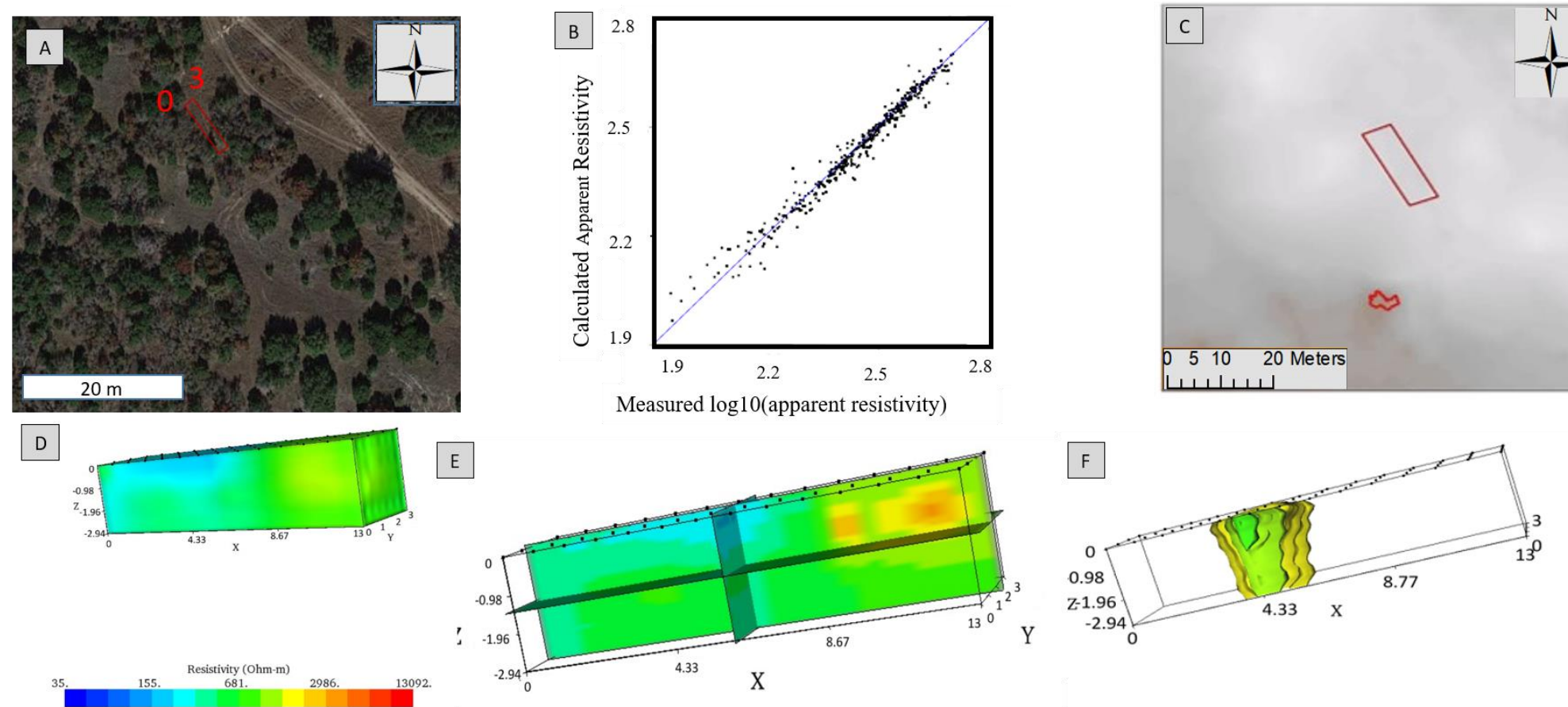
**Description:**

**A)** An overview of study area and survey line. **B)** Cross plot of data after processing. **C)** Location of survey in reference to known cave passages. **D)** Full volume of 3-D survey **E)** Dynamic contours of survey. **F)** 3-D contours of survey.

This survey was completed on the western/southwestern side of Fern Cave along a portion of Fern line 3 2-D. High resistivity corresponds to areas of high porosity. Low and medium resistivity represent the soil saturation zone and natural limestone respectively.

The first image is the 3-D total survey and shows a zone of interest on the bottom right corner of the survey. The dynamic contours show distribution in the x- and y-direction. The 3-D contour shows the general morphology of this anomaly. Though this anomaly shows general morphology that would be present in a cave structure, Resistivity values for the anomaly are high enough to represent an air-filled passage. Therefore, this zone is attributed to a zone of high porosity or larger voids like those seen in Fern line 3 2-D.

**Figure A9:** Survey analysis for Fern Cave 3-D survey 1. Maximum resistivity values are 8523 ohm-meters and RMS is 4.5%. The maximum depth achieved in this survey was 5.85 meters using 56 electrodes at 2 meters spacing in a 4-by-14 grid with cables in the x- direction.



**Description:**

**A)** An overview of study area and survey line. **B)** Cross plot of data after processing. **C)** Location of survey in reference to known cave passages. **D)** Full volume of 3-D survey **E)** Dynamic contours of survey. **F)** 3-D contours of survey.

This survey was completed on the eastern side of Fern Cave along a portion of Fern line 1 2-D that contained the probable soil piping conduit. High resistivity corresponds to areas of high porosity. Low and medium resistivity represent the soil saturation zone and natural limestone respectively.

The first image is the 3-D total survey and shows a zone of interest near the 13 m mark along cable 1. The dynamic contours show distribution in the x- and y-direction. The 3-D contour shows the general morphology of this anomaly. This coincides with the low resistivity zone seen in the 2-D survey line. This leads to the interpretation that this anomaly could be attributed to the possible suffusion feature.

**Figure A10:** Survey analysis for Fern Cave 3-D survey 2. Maximum resistivity values are 2224 ohm-meters and RMS is 4.8%. The maximum depth achieved in this survey was 2.94 meters using 56 electrodes at 1 meter spacing in a 4-by-14 grid with cables in the x-direction.



## VITA

Annie Robison graduated from Livingston High School in 2013 and after choosing a major in Geophysics attended Texas A&M University in College Station beginning in August of 2013. Annie graduated from Texas A&M in May of 2017 with a Bachelor of Science in Geophysics. January of 2018, Annie was admitted into the master's program at Stephen F. Austin State University. She will graduate with her Master's Degree in Geology in May 2020.

Permanent address: 774 West Lake Dr.

Livingston, Texas 77351

Style manual designation: Geological Society of America

This thesis was typed by Annie P. Robison